

**Finite-Element Analysis of Physical Phenomena of a Lab-Scale  
Electromagnetic Launcher**

A thesis  
Presented to  
The Academic Faculty

By

Bummo Chung

In Partial Fulfillment  
Of the Requirements for the Degree  
Master of Science in Mechanical Engineering

Georgia Institute of Technology

August 2007

# **Finite-Element Analysis of Physical Phenomena of a Lab-Scale Electromagnetic Launcher**

Approved by:

Dr. Itzhak Green, Co-Advisor  
G. W. W. School of Mechanical Engineering  
*Georgia Institute of Technology*

Dr. Richard S. Cowan, Co-Advisor  
Manufacturing Research Center  
*Georgia Institute of Technology*

Dr. Richard W. Neu  
G. W. W. School of Mechanical Engineering  
*Georgia Institute of Technology*

Dr. Jeffrey Streater  
G. W. W. School of Mechanical Engineering  
*Georgia Institute of Technology*

Date Approved: July 09, 2007

## **DEDICATION**

Turn my heart toward your statutes and not toward selfish gain.

(Psalms 119:36)

First of all, I want to give thanks and honor to God our Father for His endless guidance. I firmly believe that without His unending care and guidance I could not be where I am now. I also wish that the knowledge I have gained through this study will not be selfishly used, but it will be utilized in caring and loving others.

I am very thankful to Dr. Itzhak Green and Dr. Richard S. Cowan for their support and guidance throughout my study. I am also thankful to fellow graduate students in Tribology research group for all their support and help.

Last but not least, I also would like to thank my parents and my sister for their unending support in this journey.

Bummo Chung

Georgia Institute of Technology

August 2007

## **ACKNOWLEDGEMENTS**

This research is supported in part through the Department of Defense Multidisciplinary Research Program of the University Research Initiative as Office of Naval Research Grant N00014-04-1-0601, entitled "Friction & Wear under Very High Electromagnetic Stress." Dr. P. Peter Schmidt serves as Program Officer. Information conveyed in this thesis does not necessarily reflect the position or policy of the Government, and no official endorsement should be inferred.

## TABLE OF CONTENTS

ACKNOWLEDGEMENTS .....	iv
LIST OF TABLES .....	vii
LIST OF FIGURES .....	viii
NOMENCLATURE .....	xii
CHAPTER 1: INTRODUCTION .....	1
CHAPTER 2: LITERATURE REVIEW .....	11
2.1. Extreme Applied Electric Current .....	11
2.2. Structural Characteristics.....	14
2.3. Other Topics.....	15
2.4. Discussion.....	17
CHAPTER 3: STRUCTURAL ANALYSIS .....	19
3.1. Compliance Layer.....	21
3.1.1. Geometry, Meshing, Boundary Condition, and Element.....	21
3.1.2. Result and Discussion .....	29
3.2. Initial Contact .....	33
3.2.1. Geometry, Meshing, Boundary Condition, and Element.....	34
3.2.2. Result and Discussion .....	39
CHAPTER 4: MODAL ANALYSIS OF THE ARMATURE .....	53
4.1. Mathematical Background.....	53
4.2. Modal Analysis of the Armature.....	55
4.2.1. Geometry, Meshing, Boundary Condition, and Element.....	56
4.2.2. Result and Discussion .....	58
CHAPTER 5: ELECTROMAGNETIC ANALYSIS .....	71

5.1. Electromagnetic Analysis .....	71
5.1.1. Geometry, Meshing, Boundary Condition, and Element.....	72
5.1.2. Result and Discussion .....	77
CHAPTER 6: THERMAL ANALYSIS .....	97
6.1. Friction Heating.....	97
6.1.1. Geometry, Meshing, Boundary Condition, and Element.....	98
6.1.2. Result and Discussion .....	101
6.2.1. Geometry, Meshing, Boundary Condition, and Element.....	108
6.2.2. Result and Discussion .....	111
CHAPTER 7: CONCLUSIONS AND RECOMMENDATIONS.....	115
7.1. Conclusions .....	115
7.1.1. Structural Analysis .....	115
7.1.2. Modal Analysis .....	116
7.1.3. Electromagnetic Analysis .....	117
7.1.4. Thermal Analysis .....	117
7.1.5. Discussion .....	118
7.2. Recommendations .....	121
APPENDIX A .....	123
A.1 ALUMINUM ARMATURE .....	123
A.2 COPPER RAILS.....	123
A.3 G10 INSULATOR .....	123
A.4 MYLAR.....	124
A.5 COMPLIANCE LAYER .....	124
A.6 STEEL CONTAINMENT .....	124
REFERENCES .....	125

## LIST OF TABLES

Table 1: Area numbers and corresponding materials for Figure 6.....	23
Table 2: Area numbers and corresponding materials for Figure 8.....	27
Table 3: Comparison of experimental measurements and the FEA results.....	32
Table 4: Number of elements in contact, contact length, and contact area for six different interferences.....	50
Table 5: Frequencies and periods of the first four modes of the unstressed armature.....	61
Table 6: Frequencies and periods of the first four modes of the pre-stressed armature ...	64
Table 7: Frequencies and periods of the first four modes of the pre-stressed armature that experiences 1897.5 N on each leg.....	66
Table 8: Frequencies and periods of the first four modes of the pre-stressed armature that experiences 3795 N on each leg.....	68
Table 9: Definition of the coordinate/direction as shown in Figure 35 .....	77
Table 10: Summation of the resulting EMAG force of the armature .....	79
Table 11: Summation of the resulting EMAG force of the top and the bottom rails.....	85
Table 12: Summation of the EMAG force for top-to-bottom and bottom-to-top directional electric current flow .....	95

## LIST OF FIGURES

Figure 1: Schematic diagram of an electromagnetic launcher [1]; a) Resulting Velocity; b) Resulting EMAG forces.....	2
Figure 2: Picture of the lab-scale electromagnetic launcher .....	5
Figure 3: Schematic diagram of the cross section of the lab-scale EML.....	6
Figure 4: Decoupled FEA components of the lab-scale EML .....	8
Figure 5: Schematic diagram of the armature and the rails .....	19
Figure 6: Front view of a quarter of the lab-scale EML .....	22
Figure 7: Results of an actual Lab-Scale EML compliance test .....	25
Figure 8: Geometry used in modeling the structural compliance layer .....	26
Figure 9: Schematic diagram of the rail.....	27
Figure 10: Mesh plot of the compliance layer FEA model .....	28
Figure 11: Schematic diagram of the Plane 42 element [22] .....	29
Figure 12: Displacement along the Y axis of the compliance layer at the load of 672N..	31
Figure 13: Geometry of the initial contact FEA .....	35
Figure 14: Schematic diagram of the aluminum armature (all dimensions are in inch)...	37
Figure 15: Mesh plot of the initial contact FEA model .....	38
Figure 16: Schematic diagram of the contact and target element [22] .....	39



Figure 17: Displacement results in the X and the Y directions for interference of 0.1232 mm .....	41
Figure 18: Results of the von Mises stress for an interference of 0.1232 mm .....	42
Figure 19: Results of the contact pressure for interference of 0.1232 mm .....	44
Figure 20: Results of the von Mises stress for 6 different interferences.....	46
Figure 21: Results of the contact pressure for 6 different interferences .....	48
Figure 22: Results of the maximum von Mises stress for 30 different interferences of the half symmetric lab-scale EML model .....	49
Figure 23: Mesh plot of the 3-D armature used in the Modal analysis.....	57
Figure 24: Schematic diagram of the Solid 45 element [22] .....	58
Figure 25: Six rigid body modes.....	59
Figure 26: First four vibration mode shapes of the unstressed armature .....	60
Figure 27: Results of the X direction displacement of the deformed armature .....	62
Figure 28: Results of the Y direction displacement of the deformed armature .....	62
Figure 29: First four vibration mode shapes of the pre-stressed armature .....	63
Figure 30: Mesh plot of the pre-stressed armature that experiences 1897.5 N on each leg .....	65
Figure 31: First four vibration mode shapes of the pre-stressed armature that experiences 1897.5 N on each leg .....	66
Figure 32: Mesh plot of the pre-stressed armature that experiences 3795 N on each leg .....	67

Figure 33: 3-D model used in the electromagnetic FEA .....	73
Figure 34: Plot of the applied electric current .....	74
Figure 35: Mesh plot of the 3-D model used in the electromagnetic FEA .....	76
Figure 36: Schematic diagram of the Solid 97 element [22] .....	77
Figure 37: Iso-surface contour plots of the resulting X direction EMAG force of the armature .....	80
Figure 38: Iso-surface contour plots of the resulting Y direction EMAG force of the armature .....	81
Figure 39: Iso-surface contour plots of the resulting Z direction EMAG force of the armature .....	83
Figure 40: Iso-surface contour plots of the resulting EMAG force of the rails in the X, Y, and Z directions.....	86
Figure 41: Calculated armature velocity as a function of time .....	89
Figure 42: Calculated armature displacement as a function of time.....	89
Figure 43: Schematic diagram of resulting EMAG force for different direction current flow .....	91
Figure 44: Vector plots of the electric field for top-to-bottom and bottom-to-top directional electric current .....	93
Figure 45: Comparison of the resulting EMAG force of the armature in the X direction for top-to-bottom and bottom-to-top direction electric current flow .....	94
Figure 46: Close up geometry of the friction heating FEA model.....	99
Figure 47: Mesh plot of the friction heating FEA model.....	100

Figure 48: Schematic diagram of the Plane 13 element [22].....	100
Figure 49: Temperature results at 57.5 microseconds due to friction heating for a coefficient of friction of 0.2, the thermal contact conductance of $10^6$ J/s-K-m <sup>2</sup> , and 50%-50% heat partition between the armature leg and the rail.....	103
Figure 50: Temperature results at 62.5 microseconds due to friction heating for a coefficient of friction of 0.2, the thermal contact conductance of $10^6$ J/s-K-m <sup>2</sup> , and 50%-50% heat partition between the armature leg and the rail.....	103
Figure 51: The maximum temperature results of friction heating for three different values of the coefficient of friction .....	106
Figure 52: The maximum temperature results of friction heating for three different values of heat partition .....	107
Figure 53: Mesh plot of the worst case scenario of the Joule heating FEA model.....	109
Figure 54: Mesh plot of the best case scenario of the Joule heating FEA model .....	110
Figure 55: Schematic diagram of the Plane 67 element [22].....	111
Figure 56: Results of the temperature plot for an electric contact conductance of $10^7$ siemens per meter (S-m <sup>-1</sup> ).....	113
Figure 57: Optimization of the armature geometry .....	120

## NOMENCLATURE

$\vec{B}$	Magnetic field
$[C]$	Damping matrix
COF	Coefficient of friction
$E$	Elastic modulus
$\vec{E}$	Electric field
$[F]$	Force vector
$\vec{F}$	Force
$[K]$	Stiffness matrix
$[M]$	Mass matrix
T	Temperature
$[U]$	Displacement matrix
$[\dot{U}]$	1 <sup>st</sup> derivative of the displacement matrix
$[\ddot{U}]$	2 <sup>nd</sup> derivative of the displacement matrix
$q$	Electric charge of the particle
t	time
$\vec{v}$	Instantaneous velocity of the particle

$\{\Phi_i\}$	Mode shape vector (eigenvector) of mode i
$\lambda$	Eigenvalue
$\rho$	Density
$\nu$	Poisson's ratio
$\omega_i$	Natural circular frequency of mode i

## SUMMARY

An electromagnetic launcher (EML) is an apparatus that propels an armature between two rails. This is accomplished when an applied electric current passes through the rails resulting in a magnetic field, which with the current creates an electromagnetic (EMAG) force capable of accelerating the armature to velocities up to several thousand meters per second. The high sliding velocity, with the electric current density, creates extreme thermal conditions at the interface between the rail and the armature, such that melting can occur.

In the operation of an EML, a few highly coupled phenomena are present. The structural, thermal, and electromagnetic components are coupled together to govern the motion of the armature. In this work, because of computational limitations, the coupled phenomena are decoupled into the aforementioned individual components and each separate effect is studied in detail. This work is aimed at improving the understanding of the armature-to-rail performance and the useful life of an EML by developing a computer simulation that can be used as a design tool to acquire conditions for the best performance.

A structural finite element analysis (FEA) is performed to investigate the

structural behavior of a lab-scale EML, housed in the Laboratory for Extreme Tribology at Georgia Tech. In order to obtain realistic results, modeling of the structural compliance layer (an artificial layer incorporated into the FEA model) is done. This layer mimics any deformation that may be caused from the difference between the ideally designed parts and the actually manufactured parts. Modeling of the compliance layer is presented. The FEA determines the structural deformation, as well as the interface contact area, contact pressure, and Von Mises stress that arise due to the initial armature-to-rail contact.

A modal analysis of the armature is performed to determine its vibration frequencies and vibration mode shapes. Once the armature is placed between the rails, the armature experiences stress due to interference fit. Modal analysis of both an unstressed and pre-stressed armature is performed and results are compared. Then, the material properties and the size of the armature are varied to see the corresponding effects.

An electromagnetic FEA is performed to determine the EMAG force that results from the applied current coupled together with the resulting electromagnetic field. This FEA is performed using a quasi-static 3-D model. The model assumes a perfect contact at the contact interface. In order to minimize the computational expense in obtaining a solution, it consists of a small segment of the rails, the whole armature, and the air (i.e., a

space where the electromagnetic field resides) that surrounds the structure. One set of actual electric current input data from lab-scale EML experiments is used as a loading condition for this analysis.

Frictional heating and Joule heating are determined from a 2-D thermal FEA. Although both the frictional and the Joule heating occur simultaneously in the operation of the actual EML, in this study, both are separately studied because of computational limitations. For the frictional heating, three different values of coefficient of friction (COF) and three different values of the heat partition are incorporated in the FEA. For Joule heating, the same set of the electric current input used in the EMAG analysis is used with three different values of contact conductance.

For the Georgia Tech lab-scale EML, with an armature (aluminum)-to-rail (copper) interference of 0.1232 mm, the maximum contact pressure, and von Mises stress is close to but still lower than the yield strength of the weaker material (aluminum). Therefore, the effect of plastic deformation is not considered. The contact area is determined to be 3.32 mm<sup>2</sup>. For both an unstressed and pre-stressed armature, the current armature design results in a vibration period that is much shorter than the duration of the sliding of the armature. This means many vibrations of the armature legs are possible while the armature slides along the rails. In addition, the results of FEA show,



as expected, that the frequency is proportional to  $\sqrt{E/\rho}$ , where  $E$  is Young's modulus and  $\rho$  is the density. As the size of the armature increases, the vibration period decreases.

The EMAG analysis predicts the EMAG force that propels the armature in the lab-scale EML. Using Newton's second law of motion, acceleration is obtained and then integrated with respect to time to get the velocity. The obtained velocity is again integrated with respect to time to get the displacement. The maximum velocity of the armature is determined to be consistent with the measured experimental value, approximately 2.4 km/s. Using these results, thermal analysis of both the friction heating and the Joule heating shows that immediate melting of the tip of the armature is inevitable for the current lab-scale EML.

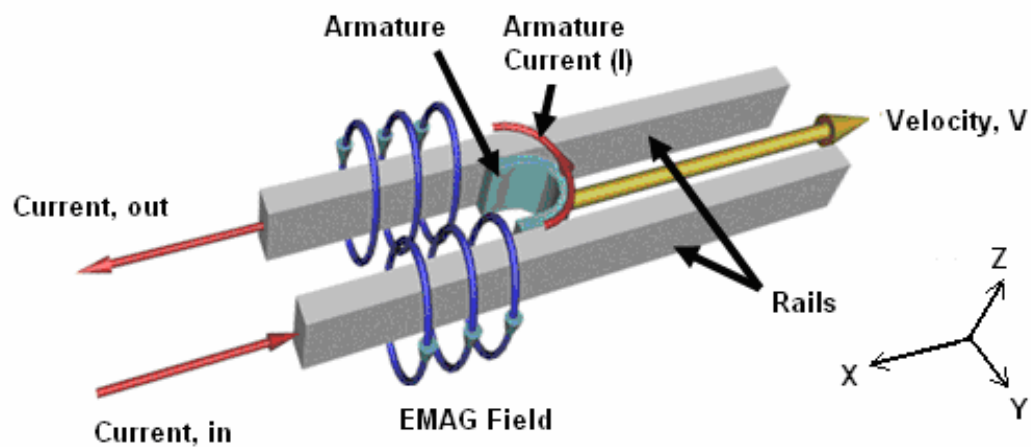
## **CHAPTER 1: INTRODUCTION**

An electromagnetic launcher (EML) is an apparatus that propels an armature along rails to achieve velocities up to several thousands of meters per second without using an explosive propellant. This is accomplished by converting electric energy into kinetic energy. Figure 1 illustrates a schematic diagram of an electromagnetic launcher (the schematic diagram of an electrical power supply is omitted).

An EML consists of two parallel metal rails that are connected to an electrical power supply and an electrically conductive armature. When this electrically conductive armature is inserted between these rails, a closed electric circuit is formed, and the EML is ready to be used. Once voltage is applied by the power supply, electric current flows to the bottom rail, across the armature, and back through the top rail as shown in Figure 1. The flow of electric current enables the EML to become a powerful electromagnet that creates an electromagnetic (EMAG) field around the rails and the armature. An applied electric current, coupled with the resulting EMAG field, creates an EMAG force, which is called the Lorentz force. This is the driving force that accelerates the armature along the rails. Since the rails also carry an electric current the rails also experience EMAG forces. Figure 1 shows the electric current flow through

the two rails. Electric current flows into the bottom rail in the negative X direction, and it flows out from the top rail in the positive X direction. This different flow direction creates an EMAG force on the rails such that the two rails repel each other.

a)



b)

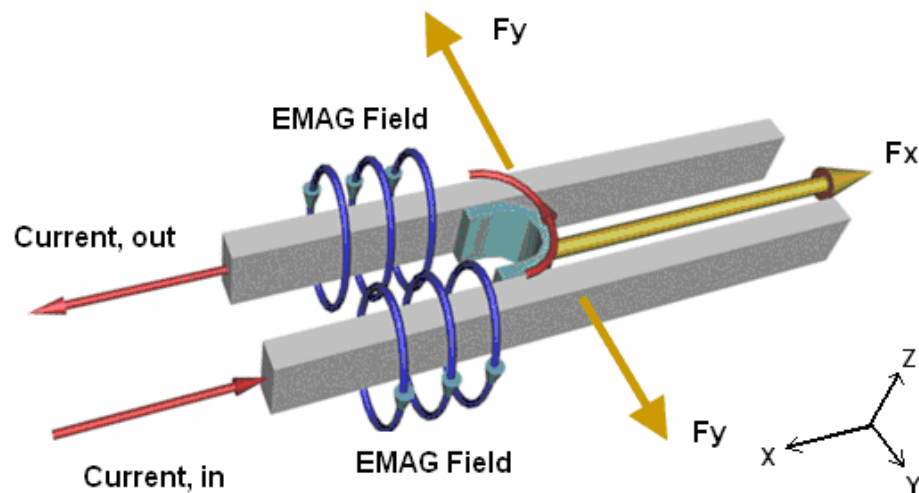


Figure 1: Schematic diagram of an electromagnetic launcher [1]; a) Resulting Velocity; b) Resulting EMAG forces

It is common to see a C-shape armature being used in an EML as shown in Figure 1. Although the EMAG force can accelerate an armature of different shapes, a C-shape armature is typically chosen because the legs of the armature experience force in the outward direction (the resulting EMAG force spreads the legs of the armature) such that the EMAG force helps in preventing the loss of contact at the interface between the armature and the rails.

Melting at the contact interface is commonly observed in the operation of an EML due to the high electric current density and the sliding velocity. This melting typically leads the molten material to be detached, which can cause loss of contact. The resulting EMAG force in the C-shaped armature tends to close the empty space that results, helping avoid loss of contact. Likewise, the molten material helps in the lubrication of the contact.

Its ability to propel an armature to extreme velocities makes an EML a good candidate for a next generation weapon. The high projectile velocities attained by an EML allow lighter projectiles to have kinetic energy equal to or superior to that of heavier projectiles fired by conventional firearms. Higher projectile velocities also allow an EML to have greater range, less bullet drop, and less wind drift. In addition, the use of an electromagnetic force to propel an armature eliminates the danger of

carrying an explosive. Despite these advantages, the need for significant electrical power can be a major disadvantage. In order to fire an EML, electric current up to several mega-amps must be supplied to the EML. This makes an EML impractical for applications such as portable firearms until portable power supplies that can supply the aforementioned electric current are developed.

Another possible application of an EML is a mass driver for space exploration. An EML can be used to launch bulk ores into space from low-gravity bodies such as the moon and asteroids. If the required electrical power for the operation of an EML can be obtained from solar energy, then the need for consumables such as rocket fuel can be eliminated and therefore the pollution created from using such consumables can be prevented.

Although high projectile velocities and the use of EMAG force are attractive and desirable characteristics of an EML, these features also act as adverse factors and bring complexities to EML research. For example, the resulting extreme sliding velocity makes it difficult to accurately measure and capture what happens at the contact interface. The typical velocity obtained ranges from several hundred meters per second to several thousand meters per second, which means that complex coupled phenomena occur in a couple of milliseconds to a couple of seconds. As a result, important information for the

analysis of the EML performance such as the vibration characteristics of the armature legs during sliding, the exact location and time of the melting of the material, and the deformation of the armature cannot be measured or captured in many situations.

In order to improve understanding of the armature-to-rail performance and the useful life of an EML, a lab-scale EML has been developed at the Extreme Tribology Research Facilities at the Georgia Institute of Technology and several experiments have been performed. Figure 2 shows a picture of the actual lab-scale EML setup.

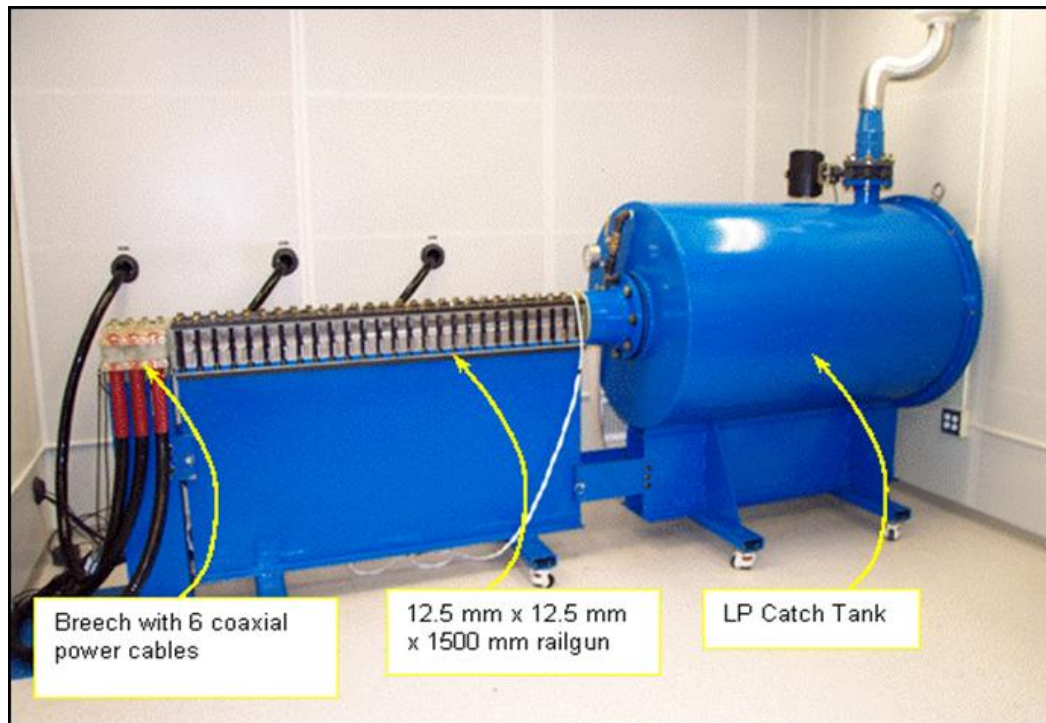


Figure 2: Picture of the lab-scale electromagnetic launcher

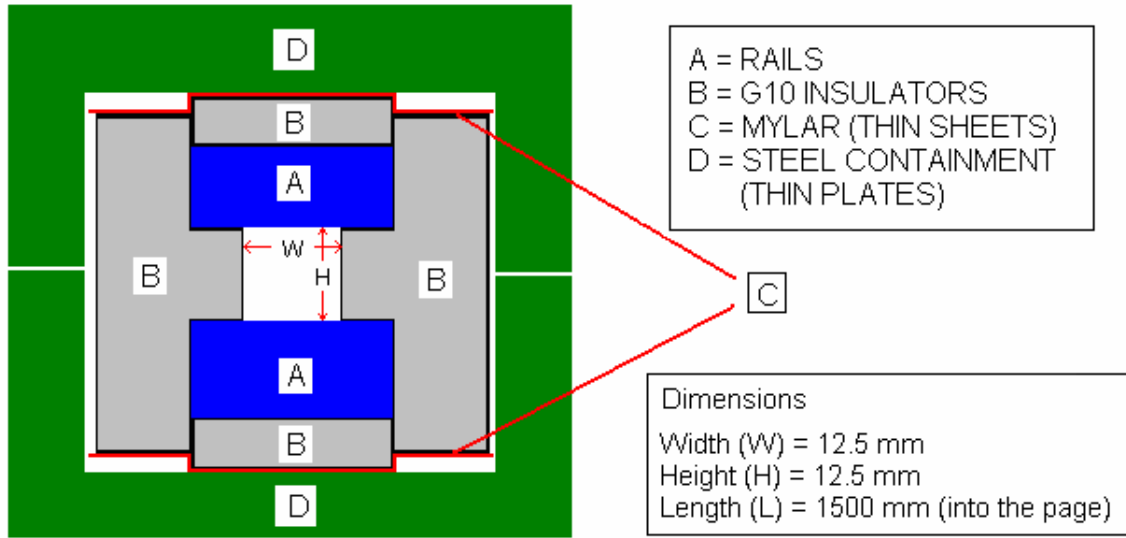


Figure 3: Schematic diagram of the cross section of the lab-scale EML

Figure 3 shows a schematic diagram of the cross section of the lab-scale EML. As shown in Figure 3, the dimensions of this lab-scale EML are approximately 12.5mm in width, 12.5mm in height, and 1500mm in length. Aluminum 6061 T651 is used as a material for the armature, and copper UNS C11000 is used as the material for the rails. G10 and Mylar (thin sheets) are used as the electrical insulating materials. The structure that holds the rails and the aforementioned layers is made of thin sheets of steel, stacked and bolted together. At the end of the EML, a catch tank is attached for catching the high velocity armature. Although it is not shown in Figure 2 and Figure 3, there is a pulse discharge power supply (PDPS) that supplies electric current through coaxial power cables. The PDPS consists of six individually operated power supply modules each

with a maximum stored energy of 13.5 kJ. Each power supply module contains five 210  $\mu\text{F}$  capacitors with a maximum charge voltage rating of 5.7 kV. The PDPS can store total energy of 81.9 kJ at a peak charge voltage of 5.1 kV.

A finite-element analysis (FEA) of this lab-scale EML is presented in this work in order to improve the understanding of the physical phenomena of an EML. It is decoupled as shown in Figure 4 into structural, modal, electromagnetic and thermal analyses. There are two reasons why this was done. First, the University version of the commercial FEA package, ANSYS, the version used in this study, limits the number of nodes that can be used in modeling. The node limitation does not allow a three-dimensional lab-scale EML FEA model to be adequately meshed. The second reason is attributed to a computational hardware limitation. With a coupled model, a solution could not be obtained due to insufficient memory.



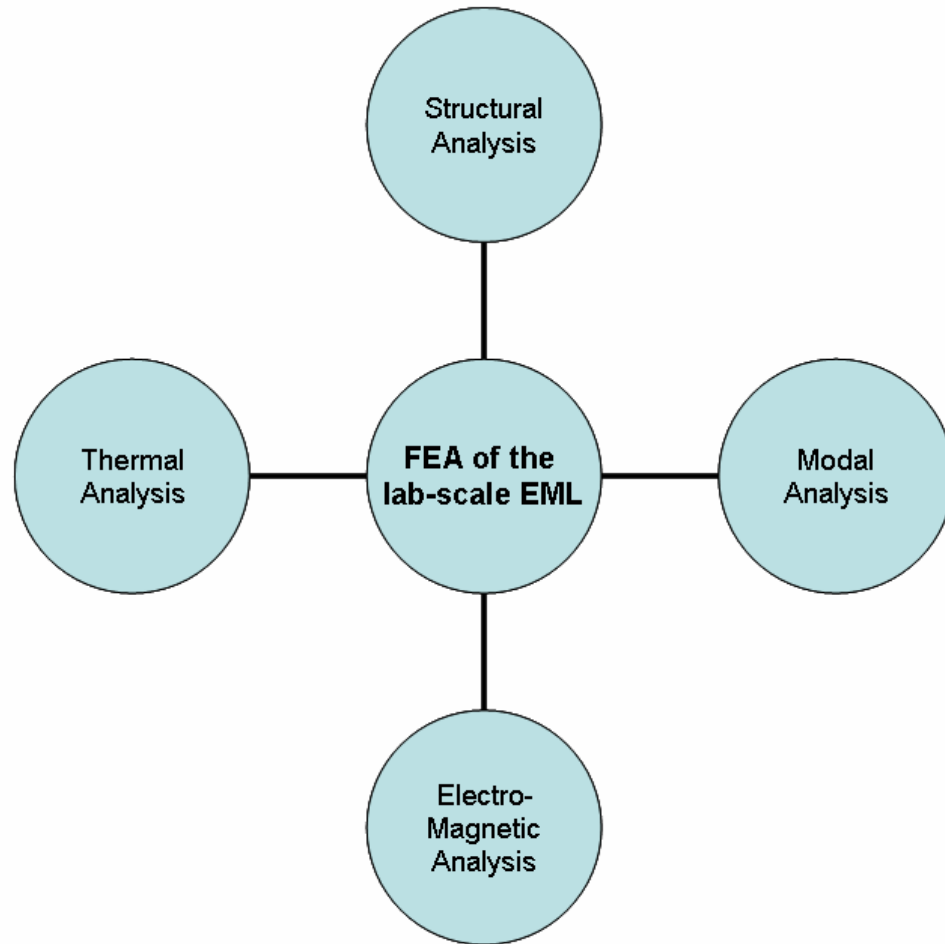


Figure 4: Decoupled FEA components of the lab-scale EML

This FEA provides results of the decoupled physical phenomena through four separate analyses, not the coupled physical phenomena. However, this FEA gives many meaningful results. Structural analysis of the initial contact will not only indicate how the armature deforms, but it will also determine factors influencing EML performance, such as the actual contact area, the contact pressure, and the maximum stress. Modal analysis of the armature provides the inherent vibration characteristics of the armature

legs. This analysis can provide guidelines for design modifications of the armature geometry. Electromagnetic analysis will determine the EMAG forces created due to the applied electric current, which when summed will enable the velocity and the displacement of the armature to be calculated as a function of time. Thermal analysis determines the temperature rise of the EML due to Joule and frictional heating. A simulation of the sliding armature is created to investigate the effect of the friction heating. A stationary armature-rail model is used to investigate the effect of Joule heating. These analyses will show that each mode of heating influences the melting of material at the contact interface, and will predict where the melting of the material occurs.

Results from this investigation will not only improve our understanding of an EML, but will also provide guidance for achieving the optimum contact condition (contact pressure and contact area) that will minimize the adverse thermal and abrasive wear of armature and rail. In addition, modal analysis will provide guidelines for selection of a material that will reduce the vibration of the armature legs.

This work is organized in the following way. Chapter 2 provides a literature review. Many aspects of previously performed and conducted EML research are presented. Chapter 3 provides the structural analysis for the initial contact. Important factors like contact area, contact pressures, and the maximum von-Mises pressure of the

initial configuration of the lab-scale EML are determined. Chapter 4 provides a detailed study of the inherent vibration characteristics of the particular armature geometry used in the lab-scale EML. A pre-stressed armature and a non stressed armature are considered in the analysis, and the results are compared. Chapter 5 presents the electromagnetic FEA. The Lorentz force created due to the applied electric current is determined, and using the force results, acceleration, velocity, and the displacement of the armature are calculated as a function of time. Chapter 6 provides the effects of the frictional heating and the Joule heating through thermal-electric coupled analysis. Chapter 7 provides conclusions from the present work and recommendations for future work.

## **CHAPTER 2: LITERATURE REVIEW**

Due to the highly coupled nature of phenomena that result in operation of an EML, thus far there have been no universally accepted principles that provide complete understanding of the armature-to-rail performance and the useful bore life of an EML. Many attempts to explain what happens during the operation of an EML have been made using theoretical and analytical studies, actual experiments, and finite-element analysis. In this section, summaries of previous work are presented in three categories. The first category summarizes those works that discuss the effects of an extreme applied electric current. The second category includes summaries of those works that are related to the structural characteristics of the EML. The third category summarizes works that are not included in the first two categories.

### **2.1. Extreme Applied Electric Current**

The magnitude of the applied electric current used in the operation of an EML is considerably large. Typically, it ranges from several hundred kilo-amperes to several mega-amperes. This enormous magnitude of electric current creates astonishing effects at the interface between the rails and the armature. In order to enhance

understanding of the effects of an extreme applied electric current at the constricted pathway, many studies have been conducted. Merrill and Stefani [2] developed an analytic model of the current melt wave in a one-dimensional stationary conductor to gain insight into the complex problem of melt-wave erosion contact wear in EML armatures. Their result suggests that the electrodynamics of the moving melt-wave boundary have an insignificant effect on melt-wave erosion in solid armature EML and as such can be justifiably neglected. The electro-thermal behavior of solid armatures in an EML has been studied by Angeli and Cardelli [3]. From their model, they found that most of the applied electric current flows through primary and secondary current paths. Their model predicted that vaporized, molten, and solid zones would form in the trailing contact between rails and armature. Drobyshvskii et al. [4] studied the effect of the thermoelectrodynamic loss of material by a solid armature in an EML. They reported that there is redistribution of the current as a result of Joule diffusion as the armature accelerates along the rails. This decreases the electrical conductivity and causes heating in the region where redistribution occurs. The redistribution of the electric current causes an uneven heating at the trailing edge of the armature and eventually the detachment of the melted material. This causes initial shunting arcs behind the armature. They supposed that this is one of the reasons that a loss in

expected velocity of the solid EML armature can occur. Powell and Zielinski [5] developed an initial numerical model for solving the equations that predict current and heat transport in a series-augmented, solid-armature EML and then they [6] modified their initial model to include the solution of coupled Maxwell and heat transport equations. Their results suggest that the velocity skin effect<sup>1</sup> is significant at points near the rail-armature interface at moderate velocities and that there is significant heating where the high current density occurs. Also they found that the fast rise time and decay of the current pulse led to some magnetic energy remaining in the armature (and rails) at the termination of the pulse. Kim et al. [7] developed a three-dimensional finite element model for the thermal effect of imperfect electric contact. A higher contact resistance, an effect of an imperfect electric current, results due to the air gaps and the constriction between the two surfaces. Their model shows that an imperfect electric current effect dominates at the early launching stage due to a current concentration over the outer and trailing edge of the armature. Comparison shows that, at the early launching stage, the local temperature over the imperfect electric current interface is higher than that of a perfect contact.

---

<sup>1</sup> Velocity skin effect is an uneven distribution of current in a moving armature and rails due to diffusion effects in the rail material.

## 2.2. Structural Characteristics

Several experiments demonstrate that one of the important factors that govern the maximum velocity of the armature is the metal-to-metal contact at the contact interface between the rails and the armature. For as long as the interface stays in contact, the armature experiences a Lorentz force and continuously accelerates. However, once the contact is lost, many unfavorable effects such as arcing and gouging, occur. Arcing is a luminous discharge of current that is formed when a strong current jumps a gap in an electric circuit. Gouging is a groove or hole made on the rail due to sliding of the armature. These phenomena destroy the metal-to-metal contact at the interface. In order to understand the reasons that destroy the metal-to-metal contact at the contact interface, many studies have been conducted. Drobyshevkiî et al. [8] indicated in their study that the main factor determining the flow of physical processes on the interface of a sliding solid-state contact carrying a current  $\sim 0.1-1 \text{ MA/cm}^2$  is a sausage-type magnetohydrodynamic (MHD) pinch instability. A sausage-type MHD pinch effect is an axial expansion of a cube as a result of compressing its side faces by a magnetic force. It vertically deforms the armature and leads to gouging on both rails. They found that the effects of the third dimension (transverse relative to the flowing current) are important, and must be considered in future studies. Drobyshevkiî et al. [9] provide more insights

about how a solid armature launcher contact transitions into an arc mode. The term *transition* is defined as the process in which the status of the contact interface changes from metal-to-metal contact to arcing. They found that three-dimensional MHD processes develop in the gap between the contact surfaces, where the resistance to shear is zero. They also answered why teardrop-shaped gouging occurs with the same reason previously discussed as offered by Drobyshevskii et al. James and James [10] provided a general solution predicting the transition velocity of a solid armature which is derived using a velocity skin-effect current-wave model. In addition, they proposed in their study a concept of a *supported* armature in order to exert an adequate outward force to maintain a contact pressure at the rear contact surface at start-up. Tzeng [11] developed a model to investigate the dynamic response of an electromagnetic launcher, induced by a moving magnetic pressure during launch of projectiles. The derived solution suggests that a high magnitude of cyclic stress can occur that might cause damage in the rails, might accelerate growth of defects, and might shorten rail life significantly.

### **2.3. Other Topics**

Many advantages inherent in lubrication for sliding motion of the armature led Kothmann and Stefani [12] to develop a thermal hydraulic model of melt-lubrication for



the EML armature. The model was moderately successful at reproducing results of experiments that measured high-speed mechanical wear of 7075 aluminum sliding against electrolytic tough pitch (ETP) copper for face pressures ranging from 45 to 150 MPa.

Another innovative subject was studied by Satapathy and Persad [13]. They studied thermal stresses in an actively cooled two-piece rail structure. The study concluded that use of rail overlays and active cooling not only reduces the peak temperature, but also affects the overall thermal gradient. Thin resistive overlays minimized thermal stress by affecting a more even temperature distribution. The active cooling system was ineffective for single launchers, but enabled faster heat removal in the time between two consecutive launches.

As the power of computing capability grows, there have been many studies that use coupled finite element codes to simulate the operation of the EML. Hopkins et al. [14] performed an analysis of startup behavior in a “C-Shaped” armature using linked EMAP3D/DYNA3D finite element codes. The goal of the analysis was to investigate if the EML maintains good solid-to-solid sliding contact during the initial portion of a launch. The simulation determined that a peak displacement transverse to the direction of motion was on the order of 0.1mm. Newill, et al. [15] developed a different coupled

finite element code for armature design. This FEA coupled two-dimensional electromagnetic analysis with three-dimensional dynamic structural mechanics analysis. The finite element code can be used to calculate the acceleration, velocity, and distance of the armature as a function of time. Also, the temperature of the armature can be determined using this FE code. The advantage of this coupled model is its capability to perform rapid assessment of the EML and the armature structure.

## **2.4. Discussion**

Based on the studies introduced in this chapter, there have been attempts to explain the failure modes of the EML. As mentioned, the principal challenge of the EML is to eliminate or delay the transition to arcing contact. Thus far, there are two major mechanisms that explain the reason for the transition of the solid armature in the EML. The first mechanism is broadly known as “wear-induced transition”. It results from uneven or excessive loss of material from the armature at the rail contact interface. There have been many studies [16-20] on this transition mechanism. These studies state that the cause of wear is “melt wave erosion” which is intense skin-effect heating at the perimeter of the armature that creates a self-sustaining form of molten material. They explain that transition occurs because loss of material from the perimeter of the armature

causes the current flow to converge which generates a repulsive force tending to separate the contact face of the armature from the rail. The second mechanism, known as “electrodynamic transition”, is associated with a rapid reduction in driving current. This transition mechanism is studied in detail in [21]. They have used 3-D FEA to observe the development of localized forces at the edges of the armature as the driving current drops rapidly. They proposed that this behavior could be the reason for molten material to be ejected from the armature-rail contact region and causes arcing to occur.

In this work, using FEA, physical phenomena of the lab-scale EML is investigated. Useful information such as the contact area, the contact pressure, the von Mises stress, the vibration characteristics (frequencies and mode shapes), the electromagnetic (Lorentz) force, the friction heating, and the Joule heating of the lab-scale EML are provided. This information will help provide a better understanding of the contact interface between the armature and the rails, of use in predicting the failure modes of the solid armature and the rail of the current lab-scale EML. Prediction will provide insight of how the current lab-scale EML operates and ways of improving current lab-scale EML design for better performance.

In the next chapter, the results of a structural FEA are presented, of use in understanding the structural deformation of the lab-scale EML for initial contact.

### CHAPTER 3: STRUCTURAL ANALYSIS

For the lab-scale EML that is investigated in this study, initial armature-to-rail contact is established by means of an interference fit as shown in Figure 5.

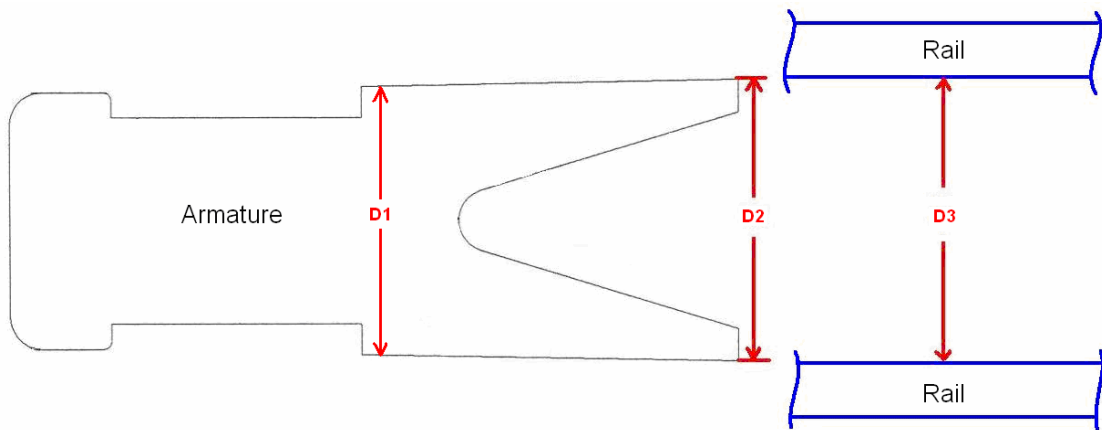


Figure 5: Schematic diagram of the armature and the rails

The armature is tapered;  $D_1$  is smaller than  $D_2$ . It allows the armature to be easily pushed in between the two rails. The distance between the outer edges of the two legs ( $D_2$ ) of the armature is designed to be slightly greater than the distance between the inner edges of the two rails ( $D_3$ );  $D_2 > D_3$ . Therefore, as the armature is pushed in between the two rails, the armature deforms and an initial contact is established at the interfaces between the rails and the armature. In this chapter, a 2-D structural FEA of

the lab-scale EML is performed to investigate the effects of the initial contact. This analysis provides an initial contact area, the von Mises stress, the contact pressure, and the deformation of the armature given interference set (i.e., full model is  $\sim 0.25$  mm and half model is  $\sim 0.12$  mm) for the present lab-scale EML. It should be noted that since the FEA considers the half symmetric model of the lab-scale EML, a half of the actual lab-scale EML interference is used in the rest of this chapter. Once the results are discussed, the effect of interference is studied further by examining how the variation in interference changes the contact area and the contact pressure. These results will be useful in developing guidelines for armature design. The initial contact area and the contact pressure are useful in determining frictional heating and Joule heating at the contact (a detailed discussion will be provided in chapter 6).

This chapter is organized in the following way. A FEA model of the compliance layer, an artificial layer that takes into account the stiffness of the lab-scale EML, is presented in the first section. Then, using this model, the effect of the initial contact is studied in the second section.

### **3.1. Compliance Layer**

The lab-scale EML studied here is designed to have a very small magnitude of interference. The magnitude of the interference applied in the FEA is 0.1232 mm. This value is obtained from the CAD drawings of the present lab-scale EML. Since this magnitude is very small, any stiffness that arises from manufacturing or component assembly must be taken into account in the FEA model in order to assure accurate results. Therefore, a compliance layer, an artificial layer that takes stiffness into account, is created. This section presents a process for determining geometric and material properties of the compliance layer.

#### **3.1.1. Geometry, Meshing, Boundary Condition, and Element**

The lab-scale EML is constructed using several materials. Because electric current is used in its operation, the material's electrical properties are major factors for selecting these materials. In addition, since the structure experiences significant electromagnetic force, the structural material properties are also considered.

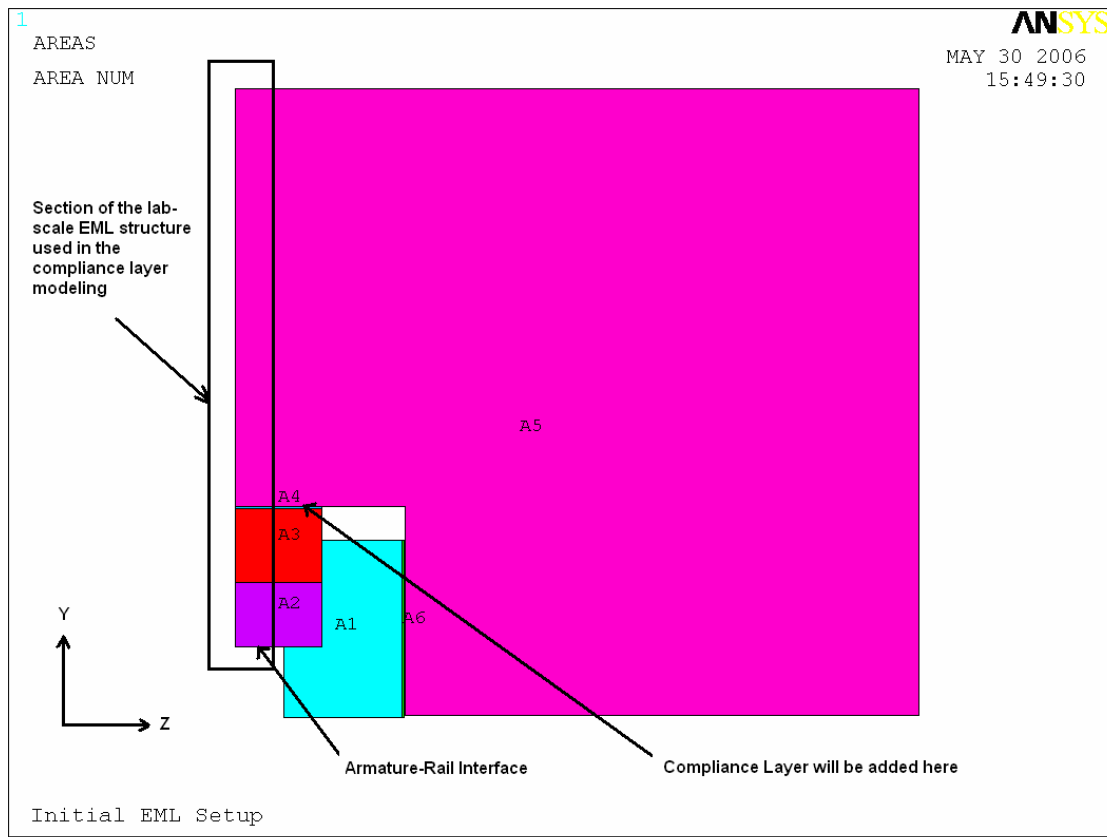


Figure 6: Front view of a quarter of the lab-scale EML

Figure 6 shows how these different materials are put together in the lab-scale EML. In this figure, the compliance layer is not yet added. Since the geometry is symmetric, only a quarter of the front view is shown in Figure 6. The symmetric planes are located along the left edge and the bottom edge. Table 1 lists the area number in Figure 6 and the corresponding materials.

Table 1: Area numbers and corresponding materials for Figure 6

Area Number	Material
A1	G10 LAYER
A2	COPPER RAIL
A3	G10 LAYER
A4	MYLAR
A5	STEEL CONTAINMENT
A6	MYLAR

Aluminum 6061 T651 and UNS C11000 copper are used for the armature and the rail, respectively, because both materials have small electrical resistivity and sufficient strength that can withstand the electromagnetic force. Since the electric current should flow only through the rails and the armature, electric insulating materials are placed to prevent electric current from flowing to the overall structure. G10<sup>2</sup> and Mylar<sup>3</sup> are selected electric insulating materials. Thin plates of UNS S30100 stainless steel (full hardened) are used in fabricating the massive structure that contains the rails. The steel plates are thin in the X direction (into the page, see Figure 6). Therefore, many plates are stacked and bolted together to make the steel containment.

---

<sup>2</sup> G10 is created from electrical alkali-free glass cloth that has been impregnated with an epoxy resin under pressure and heat.

<sup>3</sup> Mylar is one of several trade names used in the US and Britain for biaxial-oriented polyethylene terephthalate (boPET) polyester film which has high tensile strength, chemical and dimensional stability, transparency, gas and aroma barrier properties and electrical insulation.



A lab-scale EML compliance test was conducted at the Extreme Tribology Research Laboratory of the Georgia Institute of Technology. The purpose of the experiment is to investigate how the completely assembled lab-scale EML reacts when force is applied to push the rails apart and to obtain the relationship between the applied force and the resulting relative displacement of the two rails. Eleven different magnitudes of line force are internally applied in the Y axis direction to both the top and the bottom rails equally, and the corresponding displacements were measured at 80 mm away from the muzzle (exit) of the lab-scale EML. Figure 7 shows the results from this compliance test. The linear regression is performed on the results, and the regression results are also shown in the Figure 7. As shown, the  $R^2$  value of regression analysis is about 0.95. This means that the regression captures the actual experimental measurements well. The relationship between the applied force and the resulting relative displacement is therefore a linear.

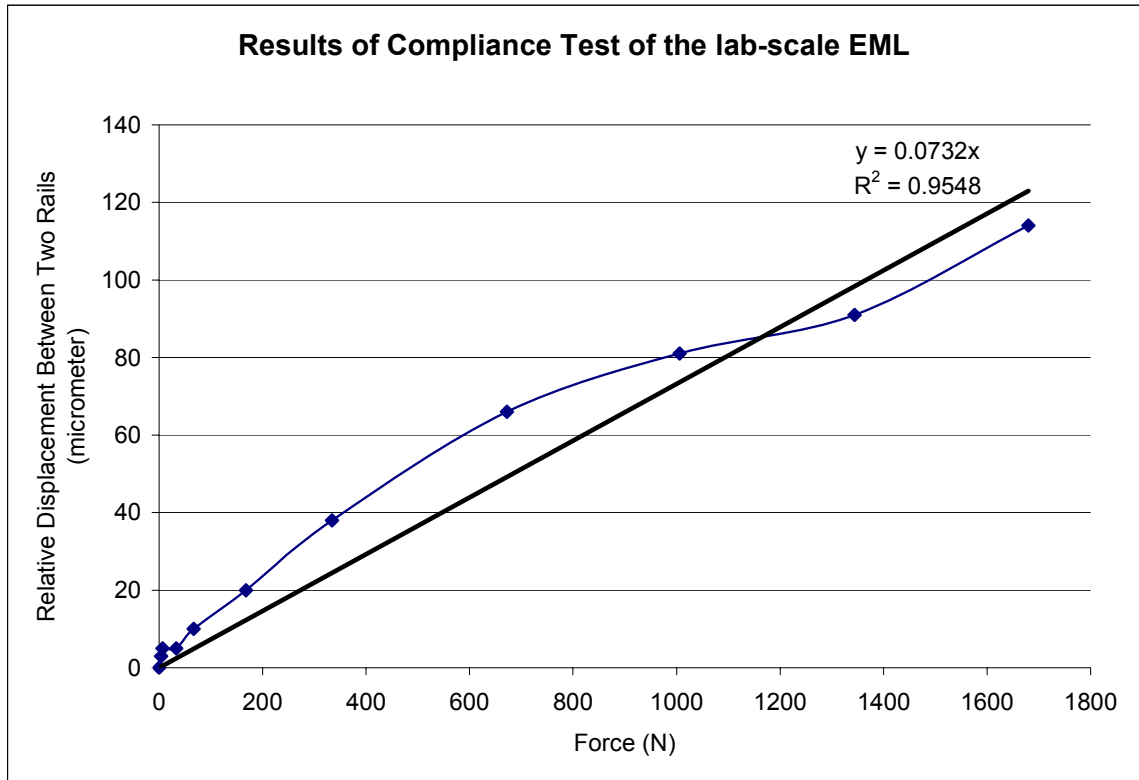


Figure 7: Results of an actual Lab-Scale EML compliance test

In order to adapt this structural compliance characteristic into the FEA model, a compliance layer was modeled. Figure 8 shows the FEA model that was used to determine the material properties of the structural compliance layer.

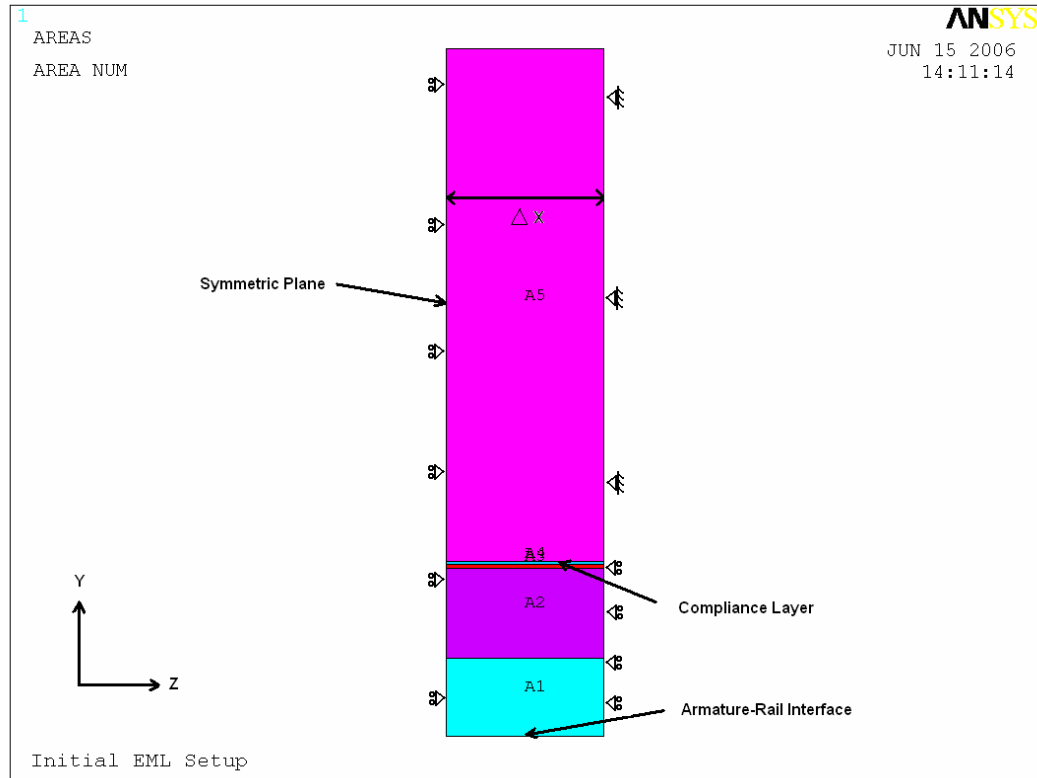


Figure 8: Geometry used in modeling the structural compliance layer

Figure 8 is the boxed region shown in Figure 6. The compliance layer is located between the stainless steel structure and the Mylar layer. The thickness of the compliance layer is 0.254 mm (0.01 inch) so that the overall geometry and structural characteristics are not greatly altered. The width ( $\Delta x$ ) of the rail and other layers shown in Figure 8 is 3.81 mm. Due to symmetric geometry, only the upper rail and layers are modeled. Along the left edge of the model (A1, A2, A3, A4, and A5), a symmetric boundary condition is applied. The right edge of A1 through A4 is constrained so as not to move in the Z direction, but allowed to move freely in the Y direction. Since the

stainless steel case is much stronger than the other materials, then the right edge of A5 is constrained so as not to move in both the Y and Z direction where the steel containment is cut along that edge. The bottom edge of A1 is the armature-rail interface. Table 2 summarizes the area numbers shown in Figure 8 and the corresponding materials.

Table 2: Area numbers and corresponding materials for Figure 8

Area Number	Material
A1	COPPER RAIL
A2	G10 LAYER
A3	MYLAR
A4	COMPLIANCE LAYER
A5	STEEL CONTAINMENT

Figure 9 shows a schematic diagram of the rail. Since the length of the rail is much greater than the width, a plane strain assumption is applied throughout the FEA of this section.

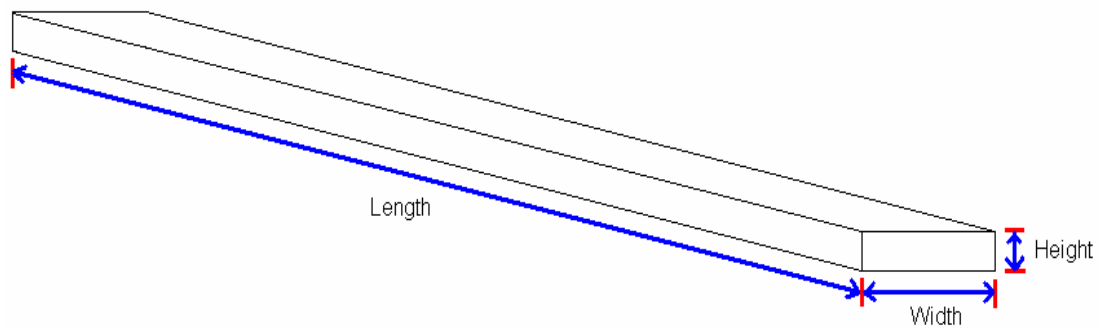


Figure 9: Schematic diagram of the rail

Figure 10 shows the meshed FEA model including the compliance layer. Since the thickness of both the Mylar and the compliance layers is small, a finer mesh density is applied in both layers. Various magnitudes force shown in Figure 7 is applied at the bottom surface of the copper rail as a distributed load.

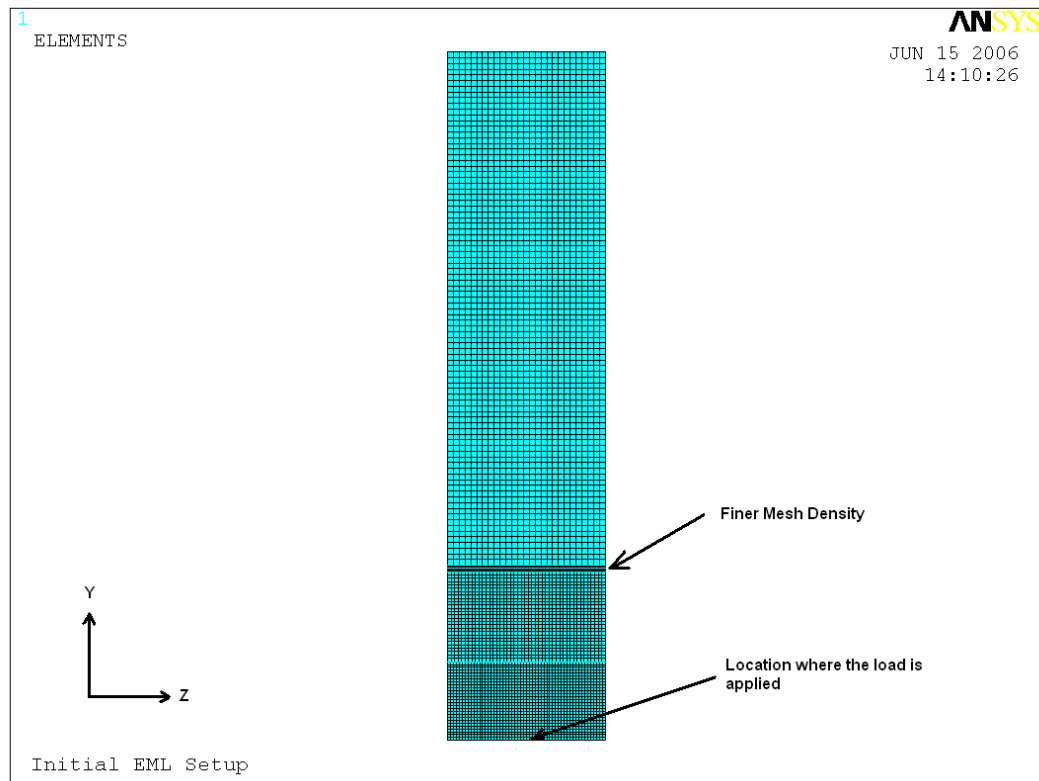


Figure 10: Mesh plot of the compliance layer FEA model

Figure 11 shows the schematic diagram of Plane 42, the element that is used in this analysis. Plane 42 is a 2-D structural solid element that can be used either as a plane element (plane stress or plane strain) or as an axisymmetric element. The element

is defined by four nodes having two degrees of freedom at each node: translations in the local nodal x and y directions, as shown.

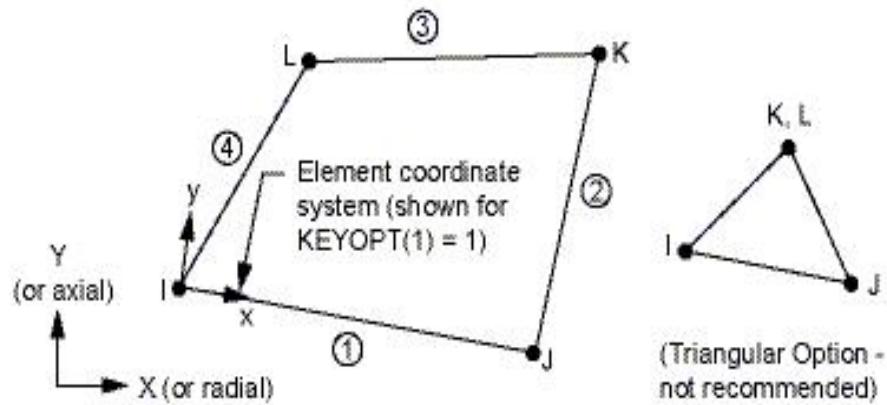
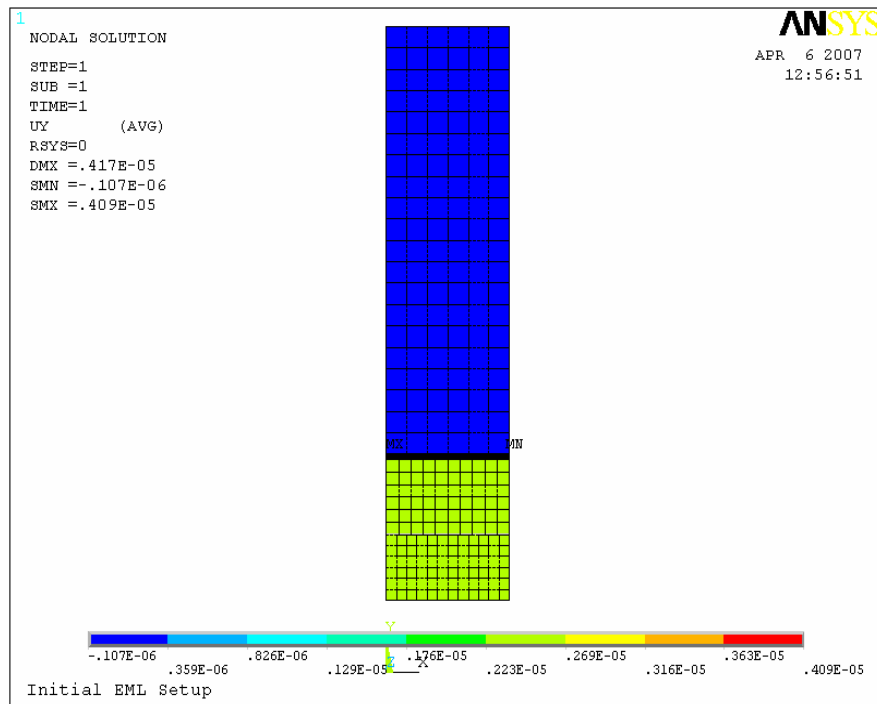


Figure 11: Schematic diagram of the Plane 42 element [22]

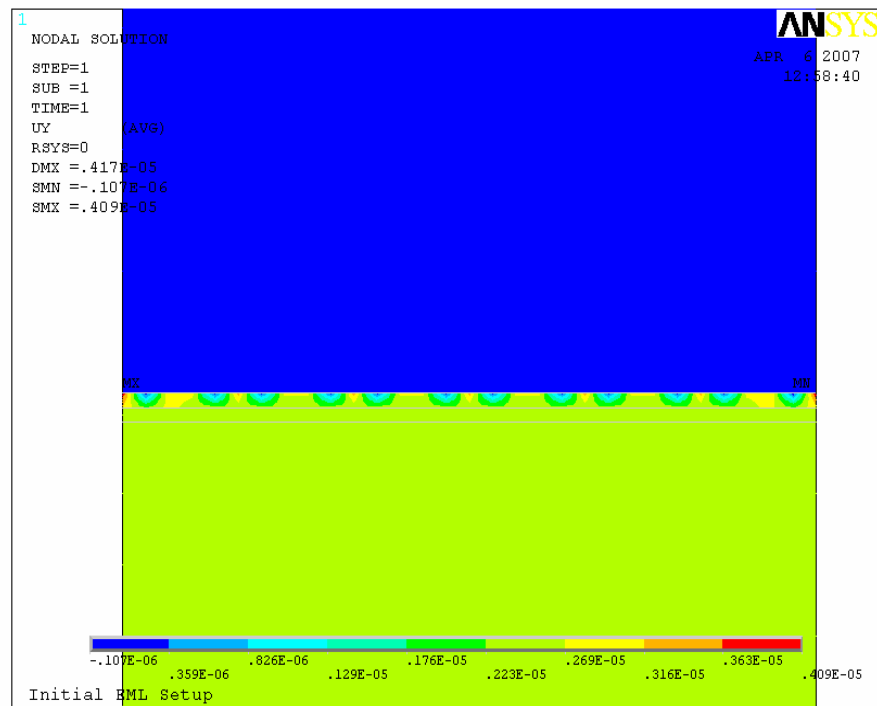
### 3.1.2. Result and Discussion

A process of trial and error is employed to determine the material properties (the modulus of elasticity ( $E$ ) and the Poisson's ratio ( $\nu$ )) of the structural compliance layer. A force is applied at the bottom surface of the rail, and the values of  $E$  and  $\nu$  are varied until the displacement result of the FEA matches the experimental measurement. The material properties,  $E$  of 20 MPa and  $\nu$  of 0.3, of the compliance layer yield the displacement results that are comparable with the experimental measurements with an approximate error of 2-3 %. Figure 12 shows a typical result of the displacement in the Y direction, with an applied force of 672N. For this particular case, all the layers (the

rail, G10, Mylar, and the compliance layer) were displaced in the upward direction approximately 24  $\mu\text{m}$ . Figure 12 clearly shows that the major deformation occurs at the compliance layer as anticipated. A similar trend of deformation (shown in Figure 12) is obtained for the remaining applied forces.



a) Overall view



b) Close up view

Figure 12: Displacement along the Y axis of the compliance layer at the load of 672N



Holding the value of  $E$  of 20 MPa and  $\nu$  of 0.3 constant, eleven different forces, shown in Figure 7, are applied in the FEA. The corresponding  $Y$  displacement results are tabulated in Table 3 with the measured  $Y$  displacement values. The measured displacements and the FEA results are listed in the second and the third column, respectively. Since only the upper rail and layers are considered in this FEA, the FEA results shown in Table 3 is the twice of the actual FEA results. The FEA results closely match the measured values.

Table 3: Comparison of experimental measurements and the FEA results

<b>FORCE (N)</b>	<b>Experimental Results (<math>\mu\text{m}</math>)</b>	<b>Regression Results (<math>\mu\text{m}</math>)</b>	<b>FEA Results (<math>\mu\text{m}</math>)</b>
0	0	0.00	0.00
4	3	0.29	0.28
7	5	1	0.48
33	5	2	2
67	10	5	5
168	20	12	12
334	38	24	24
672	66	49	48
1006	81	74	72
1334	91	98	98
1680	114	123	122

In summary, a compliance layer, which is included in the FEA model of the next section, has been created. In order to minimize a change in overall geometry and structural characteristics, the thickness of the compliance layer is set to 0.254 mm (0.01

inch). The Young's modulus and the Poisson's ratio that yield the Y direction displacement values that match closely to the measured values are 20 MPa and 0.3, respectively.

### **3.2. Initial Contact**

With the structural compliance layer having been added to the FEA model, the structural deformation and the corresponding effects of the lab-scale EML due to armature/rail interference are examined in this section. The interference of the current lab-scale EML (i.e., a value of  $D_3 - D_2$  in Figure 5) is 0.25 mm. This is the value which is obtained from CAD drawings of the lab-scale EML. Since a half of the lab-scale is modeled in the FEA due to a symmetric geometry, the interference is set numerically to be at 0.12 mm. It should be noted that the interference value presented in the subsequent section of this chapter is the half of the actual interference, since a half symmetric model is used in this analysis. The results of the X and Y displacement, the von Mises stress distribution, the contact pressure, and the contact area due to this interference are presented. Then, the effect of the interference is studied further. The interference is varied continually and the corresponding effects of the aforementioned characteristics are investigated.

### **3.2.1. Geometry, Meshing, Boundary Condition, and Element**

As mentioned previously, the armature is pushed in between two rails in order to establish the initial contact. In order to investigate the effect of the initial contact, two FEA models are created. The first model simulates the actual push-in motion. Initially, the armature is located outside of the EML, and slowly it is pushed in between two rails. The push-in motion requires many iterative steps for the solution to converge. The simulation typically requires up to six to eight hours on a PC (a Pentium 4 CPU 2.40 GHz, 2 GB of RAM) to acquire the solution. In order to obtain the initial contact results efficiently, the rails and the other layers are brought in toward each other. The armature is already placed in between the rail and the layers. This requires significantly fewer steps for convergence, and the simulation typically takes less than half an hour to acquire the solution.

Figure 13 shows the geometry of the FEA model. Parts of the rail and the other layers located far away from the actual contact do not experience any effect. Therefore, only a small segment (0.2 m in length) of the rail and the other layers are used in the FEA. In addition, due to the symmetric geometry, only half of lab-scale EML is considered in the FEA model. This allows a finer mesh to be used at the interface between the armature and the rail where contact is expected. It should be noted that the compliance

layer modeled in the previous section is added between the Mylar layer and the steel containment in the FEA model. Figure 13 also shows the coordinate system used in the FEA. The positive X and Y directions are defined to the right and to the top, respectively. This coordinate system is used throughout the analysis presented in this chapter.

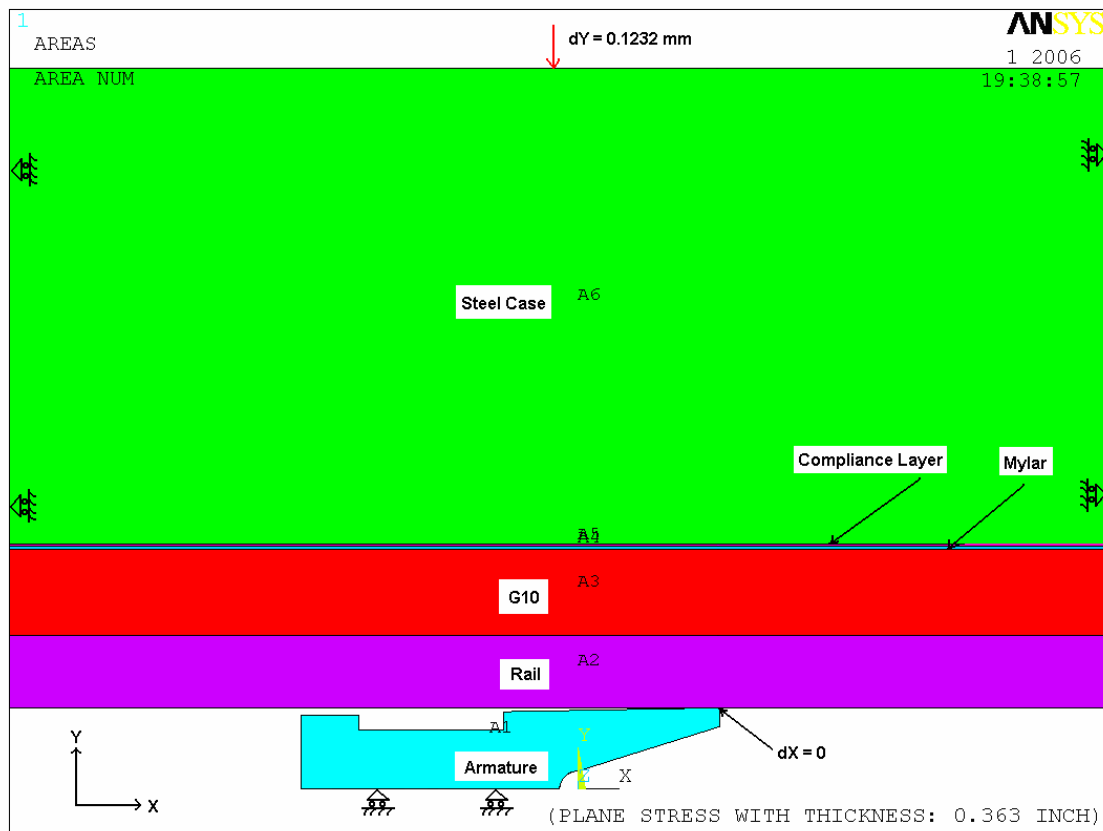


Figure 13: Geometry of the initial contact FEA

The left and right edges of the rail and the other layers are constrained so that no motion in the X direction is allowed. Along the bottom surface of the armature, a symmetric boundary condition is applied. At the top surface of the steel structure, a downward displacement of -0.1232 mm is applied. There is a small taper at the outer edge (a surface which is adjacent to the rail) of the armature geometry (see Figure 14). Therefore, if the rail and other layers are brought down without any constraint on the armature, the armature freely slides. There are two ways to prevent sliding of the armature. The first way is to apply a sufficiently high coefficient of friction at the contact interface. The high friction force at the interface between the rails and the armature prevents the armature from sliding. The second way is to simply apply the constraint to the node located at the tip of the trailing edge of the armature, so that the node does not move in the X direction while it is free to move in the Y direction. This prevents the armature from freely sliding but allows it to freely deform. In this analysis, the node at the tip of the trailing edge of the armature is constrained,  $dx = 0$  as shown in Figure 13.

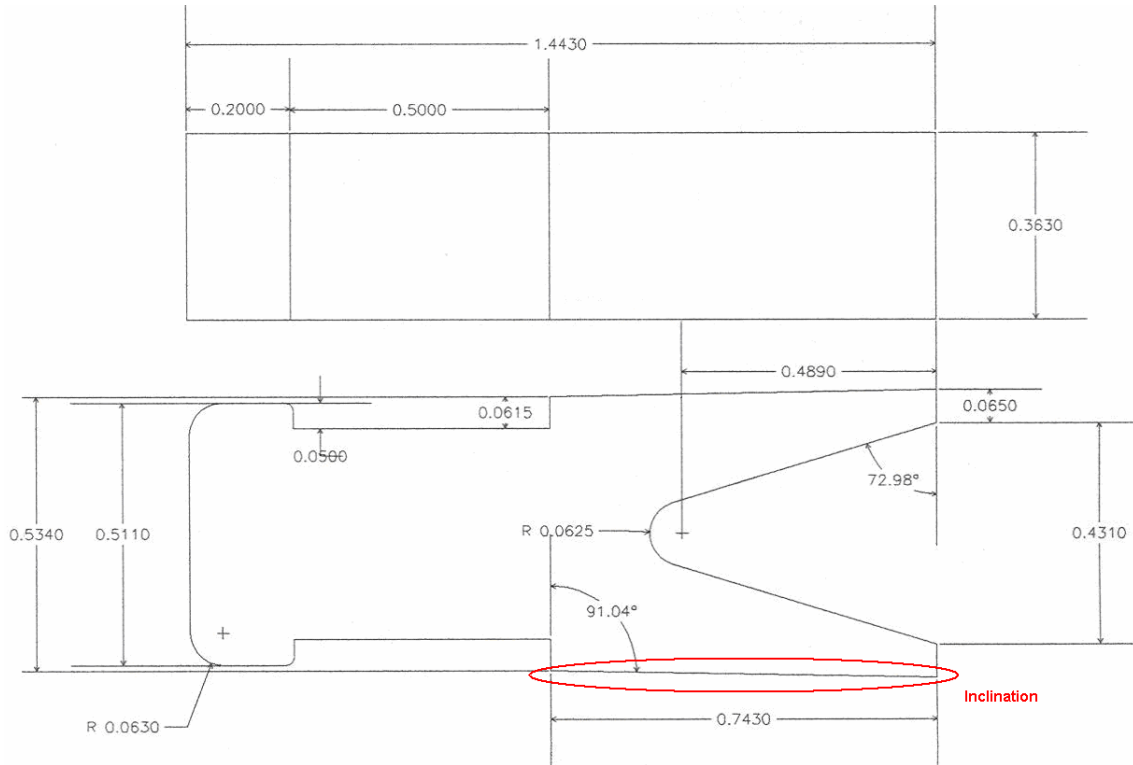
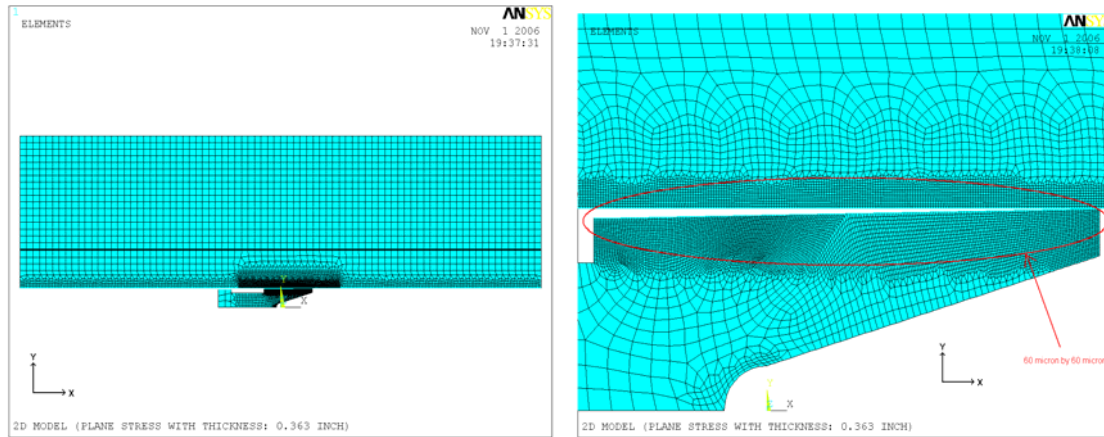


Figure 14: Schematic diagram of the aluminum armature (all dimensions are in inch)

A schematic diagram of the aluminum armature with dimensions is shown in Figure 14. Aluminum 6061 T651 is used as the material for the aluminum armature as mentioned previously. It should be noted that there is an inclination of  $1.04^\circ$  at the outer edges of the legs. This taper makes the interference an important factor in determining the contact area.

Figure 15 shows the mesh plots of the initial contact FEA model. The total number of elements used in this FEA is 14895. A finer mesh is applied where the contact between the rail and the armature is expected and around the circular section of

the armature where the two legs meet. The size of the finer mesh that is applied at the location where the contact is expected is approximately 60  $\mu\text{m}$  by 60  $\mu\text{m}$ .



a) Overall view

b) Close up view

Figure 15: Mesh plot of the initial contact FEA model

The element, Plane 42, introduced in the prior section is also used in this FEA. Plane 42 provides the plane stress with the specified thickness option. This option allows a user to specify the thickness, even though it is a 2-D element. This option is employed in this FEA with a thickness of 9.22 mm into the page. This is an actual thickness of the lab-scale EML armature. For the contact element pair shown in Figure 16, CONTACT 172 and TARGET 169 are used in this FEA.

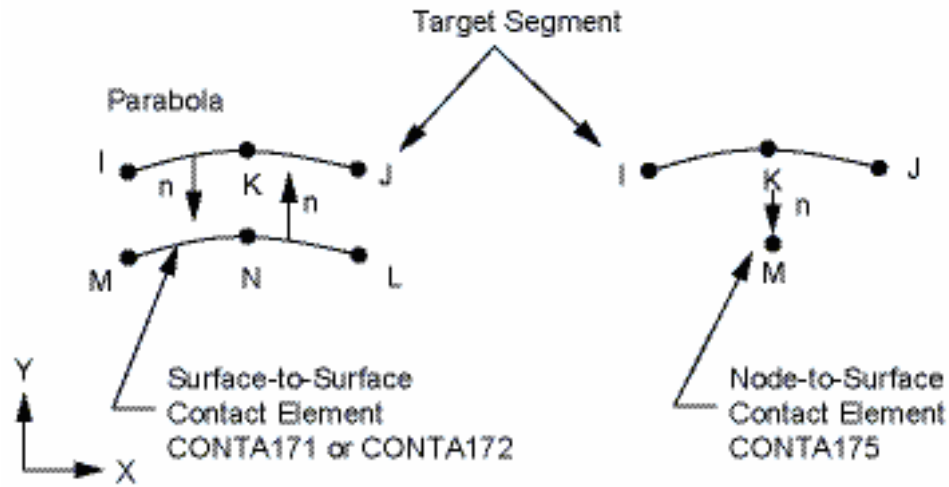


Figure 16: Schematic diagram of the contact and target element [22]

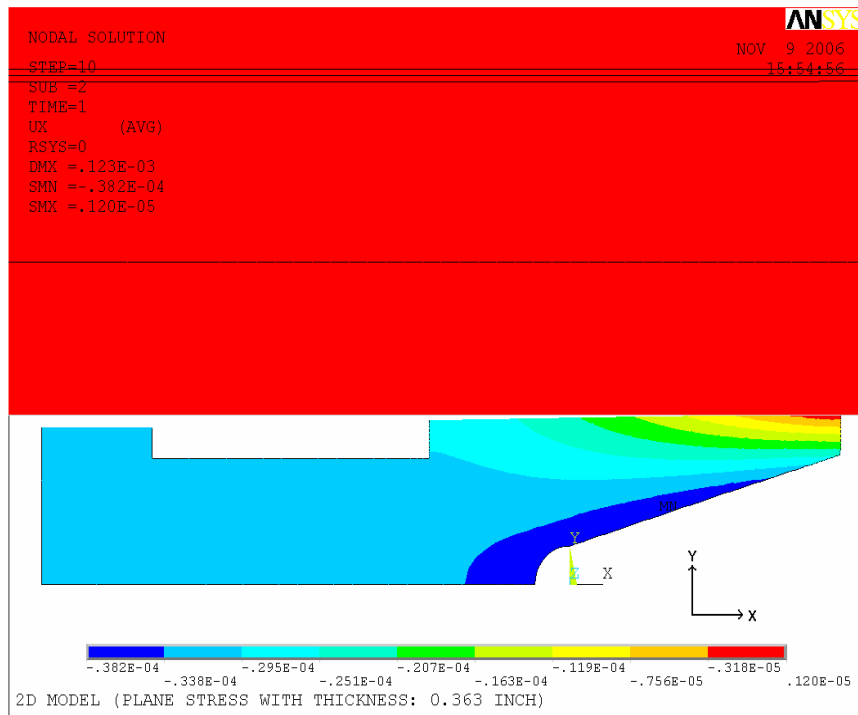
### 3.2.2. Result and Discussion

As anticipated, the simulation of compressing or bringing the rail and the other layers down for the initial contact yielded a converged solution. Although substantial number of elements is used in this FEA, the solution converges in approximately 10 minutes. The results obtained from compressing or bringing the rails and the other layers down is compared with the results obtained from a sliding simulation. The results of both cases match closely. Therefore, the approach of bringing the rail and the other layers down is employed in subsequent analyses.

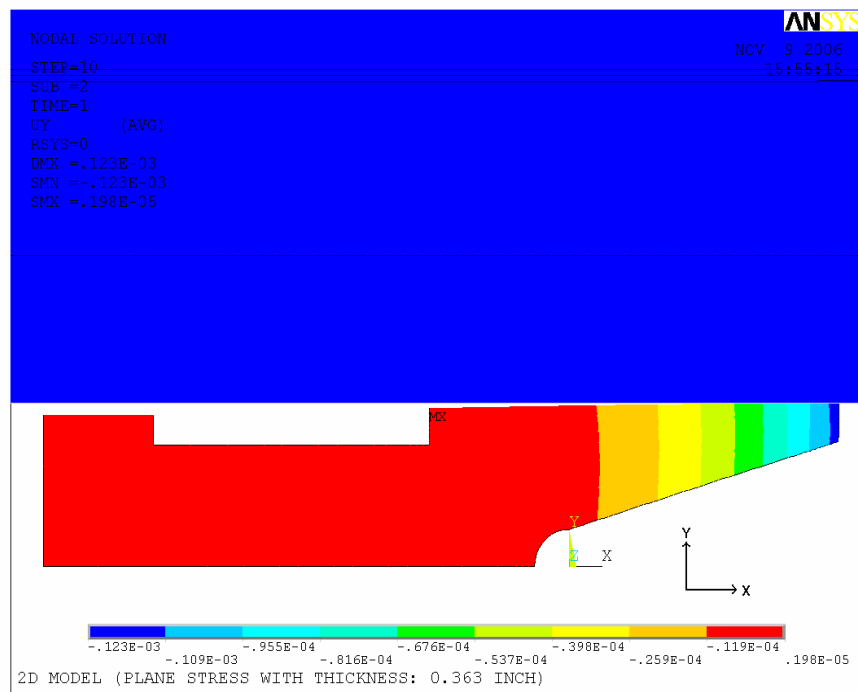
Figure 17 shows the resulting displacement in the X and the Y directions for interference of 0.1232 mm. In the X direction, the maximum displacement occurred along the inner edge of the armature leg. A portion of the armature is elongated due to



compression, although the magnitude is not significant. In the Y direction, the maximum displacement occurred at the trailing tip of the armature leg, as expected. Starting from the trailing tip of the armature, the displacement gradually decreased towards the main body section of the armature. There are investigations which try to reduce the adverse effects of friction by means of lubrication [23].

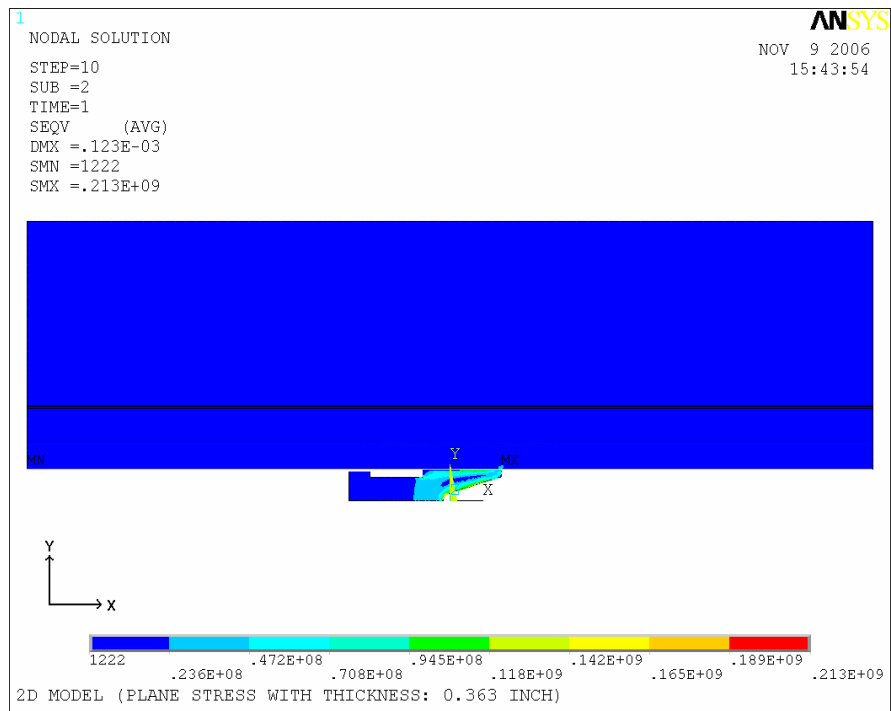


a) In the X direction

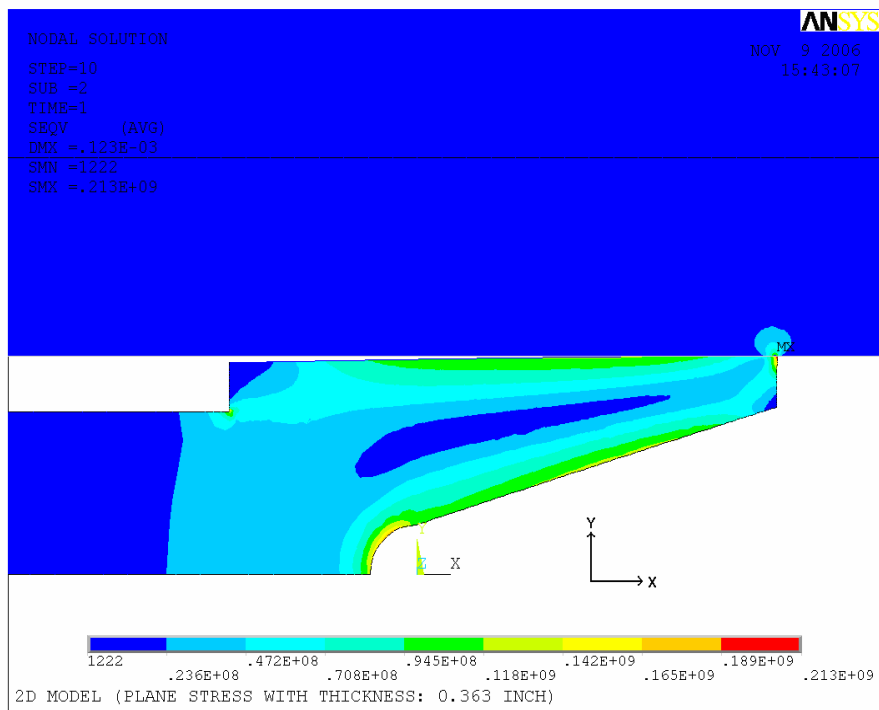


b) In the Y direction

Figure 17: Displacement results in the X and the Y directions for interference of 0.1232 mm



a) Overall view

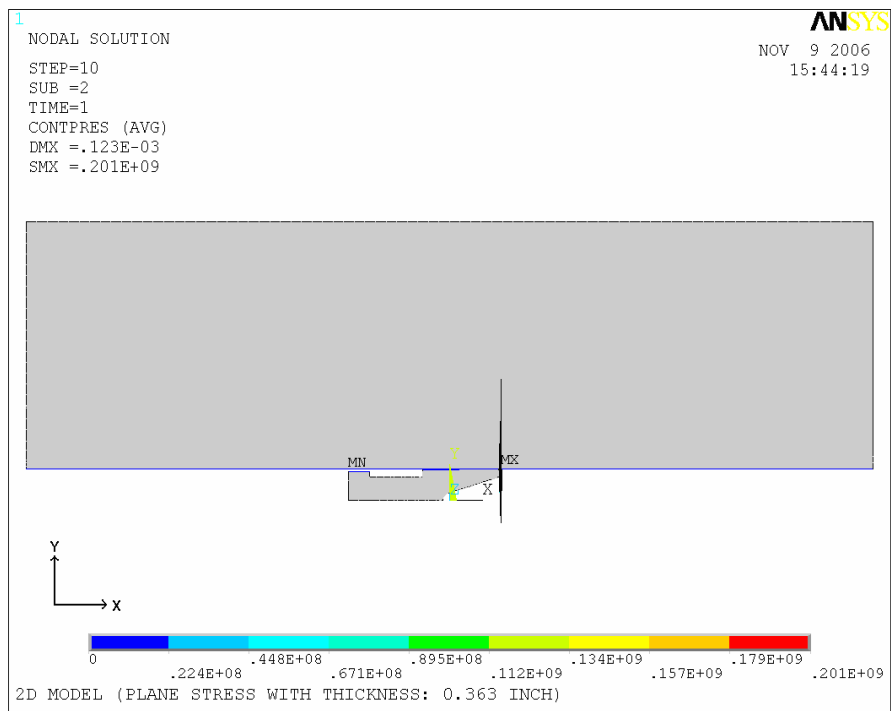


b) Close up view

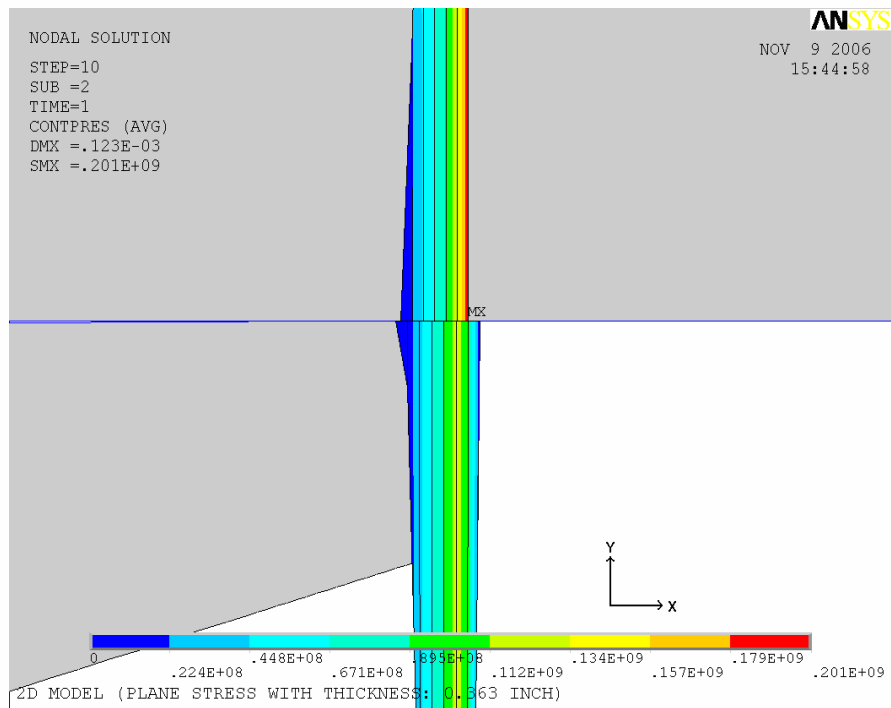
Figure 18: Results of the von Mises stress for an interference of 0.1232 mm

Figure 18 shows the result of the von Mises stress test conducted for the case of 0.1232 mm interference. The maximum stress occurs at the tip of the trailing edge and at the circular section where two legs meet the armature. The magnitude of the maximum stress is close to but still lower than the yield strength of the materials. Therefore, the effect of plastic deformation does not need to be considered for this particular interference. These results so far show that, from a structural point of view, the design of the present lab-scale EML is reasonable, since no permanent deformation results from the initial contact.

Figure 19 shows the results of the contact pressure for an interference of 0.1232 mm. A symmetric contact element pair is applied along the bottom surface of the rail and the top surface of the armature in order to obtain the contact pressure experienced by both the armature and the rail. The pressure result represented in the upward direction is the pressure experienced by the armature. The pressure result represented in the downward direction is the pressure experienced by the rail. As shown in Figure 19, the actual contact is established in a very small area. The maximum pressure experienced by the armature and the rail is approximately 200 MPa. The magnitude of the contact pressure also shows that the effect of plastic deformation does not need to be considered at the contact interface for initial contact.



a) Overall view



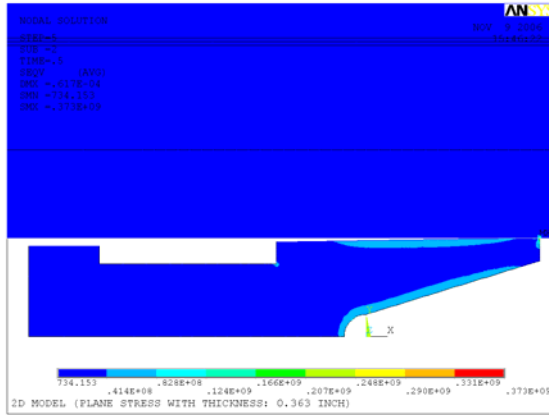
b) Close up view

Figure 19: Results of the contact pressure for interference of 0.1232 mm

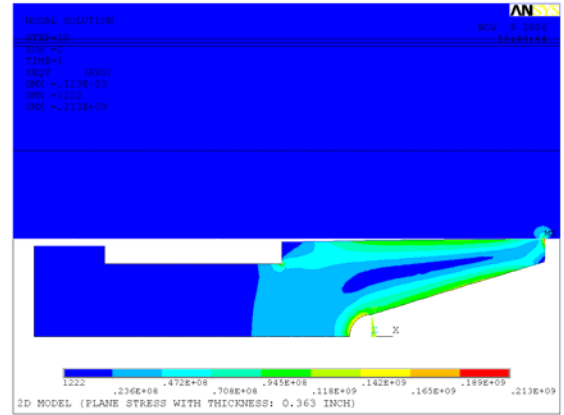
Close examination of the results shows that six elements at the tip of the trailing edge of the armature experience the contact pressure. The length of the side of the element used in that area is approximately 60  $\mu\text{m}$ . Therefore, the total contact length is approximately 360  $\mu\text{m}$ . Since the thickness of the armature is about 9.22 mm, the contact area from the initial contact is approximately 3.32  $\text{mm}^2$ .

The effects of interference are investigated further by varying the magnitude. Figure 20 shows the results of the von Mises stress measurements obtained for 6 different interferences. As the armature is compressed, initially the von Mises stress forms along the inner and the outer edges of the armature leg due to bending, while the maximum von Mises stress occurs at the contact interface. However, as more compression is applied, the trends of the von Mises stress distribution changes. Due to the C-shape of the armature geometry, the contact does not occur at the tip of the trailing edge of the armature leg anymore. The contact area moves forward along the outer edge of the armature legs. As shown in Figure 20, at the interference of 0.18 mm, the maximum von Mises stress starts to occur at the circular section of the armature, not at the contact interface. Further compression shifts the point of contact forward and reduces the inclination angle of the armature leg to close to zero. This makes the von Mises stress increase at the circular section of the armature and in the section of the rail directly above

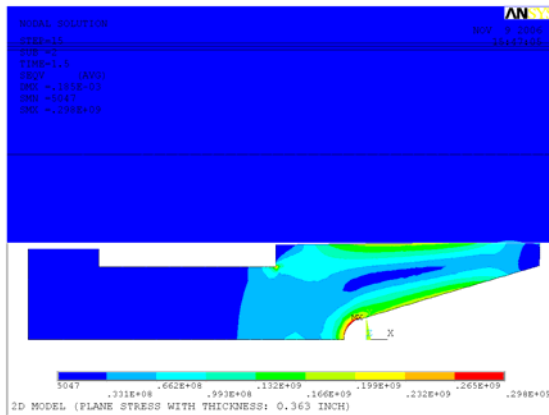
the point of contact.



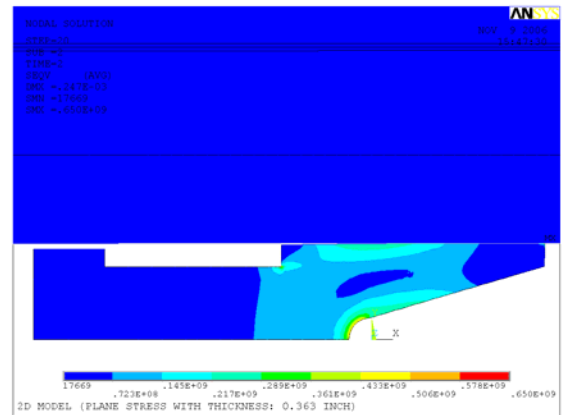
a) Interference of 0.0616 mm



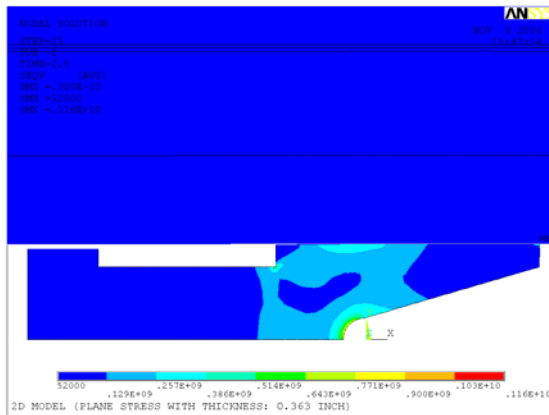
b) Interference of 0.1232 mm



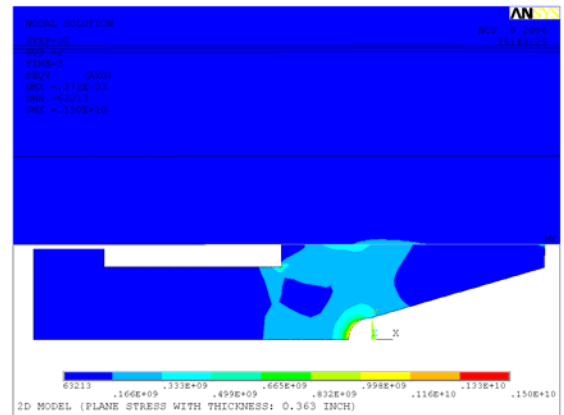
c) Interference of 0.1848 mm



d) Interference of 0.2464 mm



e) Interference of 0.3080 mm

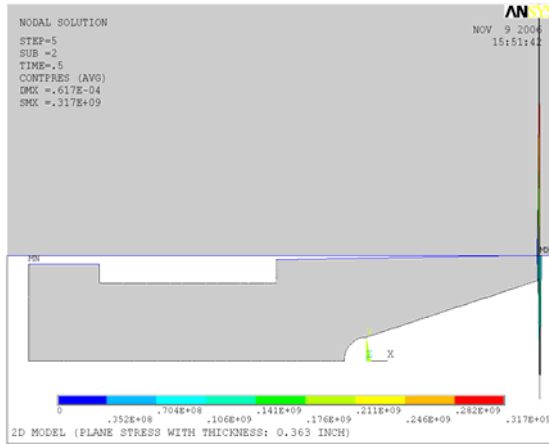


f) Interference of 0.3696 mm

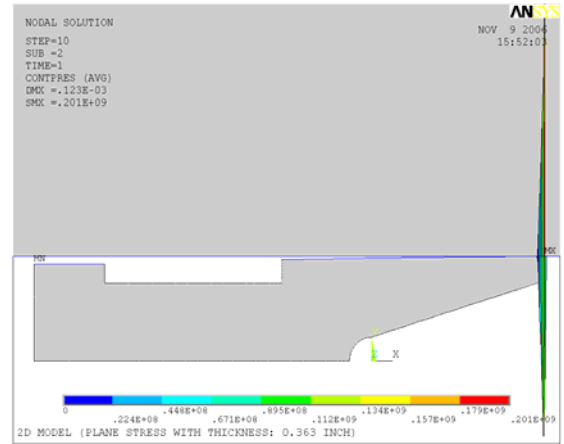
Figure 20: Results of the von Mises stress for 6 different interferences

Figure 21 shows the contact pressure results for 6 different interferences. The shifting of the point of contact discussed earlier is clearly shown in Figure 21. Initially the contact pressure is present at the tip of the trailing edge of the armature leg, and as the compression progresses, the contact pressure shifts forward with an increase in the contact area. The results of the maximum contact pressures for 30 different interferences are shown in Figure 22. The results are non-intuitive due to the C-shape armature geometry. Since the area of contact is small initially, there is a sharp increase in the contact pressure as the interference increases. The maximum contact pressure, 325 MPa, occurs at interference of 0.05 mm. Once this point is reached, any increase in the interference starts to deform the armature leg. This deformation causes an increase in the contact area, so the contact pressure continuously decreases until the interference reaches approximately 0.18 mm. After this point, as the magnitude of interference increases, the contact pressure slowly increases again because the armature cannot deform any more.

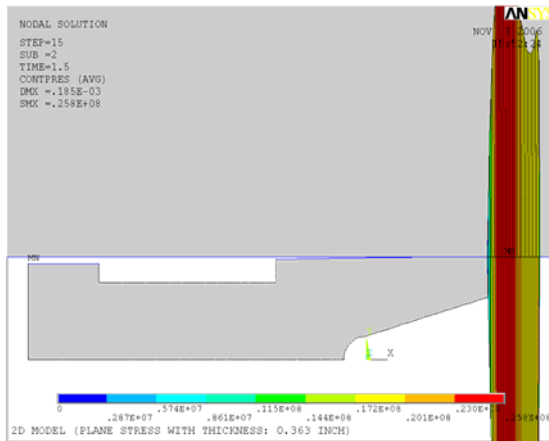




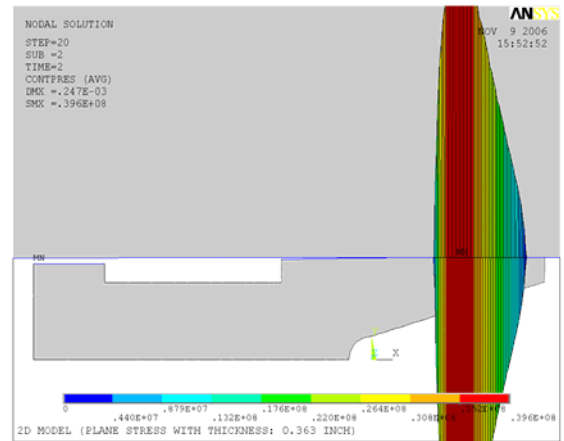
a) Interference of 0.0616 mm



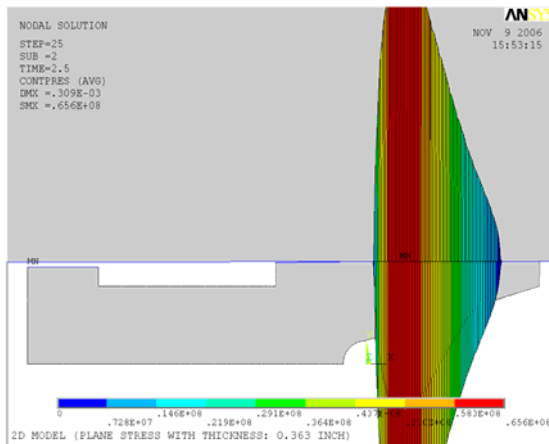
b) Interference of 0.1232 mm



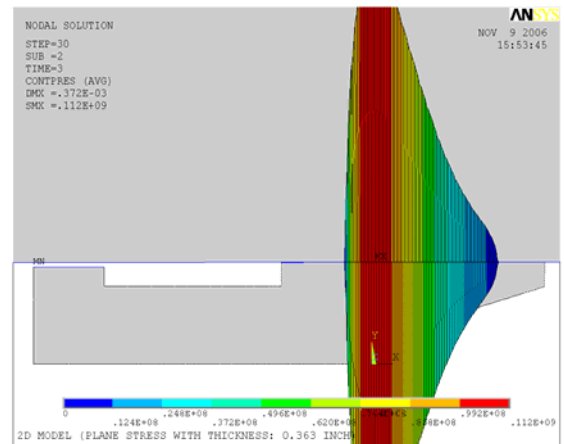
c) Interference of 0.1848 mm



d) Interference of 0.2464 mm



e) Interference of 0.3080 mm



f) Interference of 0.3696 mm

Figure 21: Results of the contact pressure for 6 different interferences

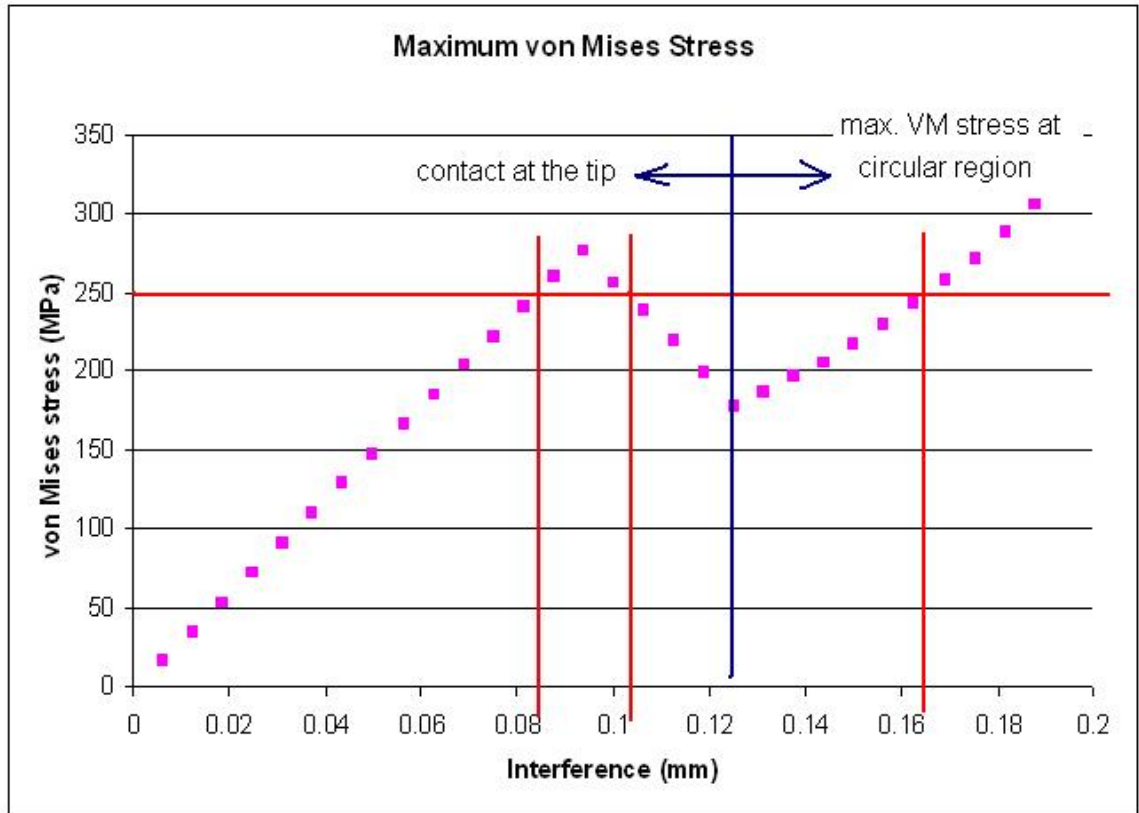


Figure 22: Results of the maximum von Mises stress for 30 different interferences of the half symmetric lab-scale EML model

Figure 22 shows a maximum von Mises stress of the half lab-scale EML model for 30 different interferences. The yield strengths of the aluminum armature and copper rail used in the lab-scale EML are 255 MPa and 305 MPa, respectively. Initially, the von Mises stress increases linearly because interference increases linearly while the contact area stays at the same location that is the armature tip. The von Mises stress then linearly decreases because the contact area increases faster with the interference. About 0.13 mm, the von Mises stress starts back to increase. At this point, the

maximum von Mises stress does not occur at the armature-to-rail interface, it occurs at the circular region of the armature. Therefore, as interference increases, the von Mises stress increases since geometry cannot deform easily anymore. Figure 22 shows that interference values between 0.085 mm and 0.105 mm and greater than 0.165 mm yield a maximum von Mises stress which is higher than the yield strength of the weaker material (aluminum). This means that as the armature is pushed in between two rails in actual lab-scale EML, the armature can plastically deform.

The contact length is determined by counting the number of elements that are in contact. The contact area is then calculated by multiplying the contact length by the thickness of the armature, 9.22 mm. The results of the number of elements that are in contact and the corresponding contact length and contact area for six different interferences are listed in Table 4.

Table 4: Number of elements in contact, contact length, and contact area for six different interferences

<b>Interference (mm)</b>	<b>Elements</b>	<b>Length (mm)</b>	<b>Area (mm<sup>2</sup>)</b>
0.0616	2	0.12	1.11
0.1232	6	0.36	3.32
0.1848	43	2.58	23.79
0.2464	76	4.56	42.04
0.3080	105	6.30	58.09
0.3693	126	7.56	69.70

The following conclusions summarize the major results obtained from the structural analysis for initial armature-to-rail contact.

1. The compliance layer which incorporates any stiffness that arises from manufacturing or component assembly is added in the FEA. With the thickness of the compliance layer set at 0.254 mm, the Young's modulus, and the Poisson's ratio is determined to be 20 MPa and 0.3, respectively.
2. The interference between 0.085 mm and 0.105 mm and beyond 0.165 mm results in the von Mises stress that is higher than the yield strength of the aluminum. This means as the armature is pushed in between two rails, it can plastically deform, since the interference values than that is used in the current lab-scale EML (0.12 mm).
3. The maximum contact pressure at the interference of 0.12 mm is approximately 200 MPa.
4. The contact area results from the initial contact are determined to be  $3.32 \text{ mm}^2$ .

The results provided in this section alone are not of much significance. However, using these results, the performance of the EML can be better understood.

For example, the friction heating and the Joule heating at the interface strongly depend on the contact area and the contact pressure. Knowing how the contact area and the contact pressure vary as a function of the interference is an important information that can be used in optimizing the performance of the EML. In the next chapter, the modal analysis of an armature is performed to investigate vibration characteristics, vibration mode shape, and vibration frequency.

## **CHAPTER 4: MODAL ANALYSIS OF THE ARMATURE**

A modal analysis is a study of the dynamic properties of vibrational excitation. It determines the natural frequencies and vibration mode shapes of a structure during free vibration and it is capable to also provide a solution to the force response. In this chapter, modal analysis of the lab-scale EML armature is performed. The scope of this study is limited only to eigenvalue problem of the lab-scale EML armature. The vibration of the rails of the EML is studied by Johnson and Moon [24].

In the first section, a fundamental mathematical background is provided. In the second section, an actual modal analysis is presented.

### **4.1. Mathematical Background**

The purpose of modal analysis in structural mechanics is to find the natural frequencies and the mode shapes of a structure during free vibration. The equations used in modal analysis are the equations that are typically seen in eigensystems. Eigenvalues and Eigenvectors determined from solving eigensystems represent the natural frequencies and the mode shapes of the system, respectively.

Equation 4.1 shows the equation in matrix form for the most basic problem

involving a linear elastic material which obeys Hooke's Law.

$$[M][\ddot{U}] + [C][\dot{U}] + [K][U] = [F] \quad (4.1)$$

where

- $[M]$  = the mass matrix
- $[\ddot{U}]$  = the 2<sup>nd</sup> derivative of the displacement maxtrix
- $[\dot{U}]$  = the 1<sup>st</sup> derivative of the displacement maxtrix
- $[U]$  = the displacement matrix
- $[C]$  = the damping maxtrix
- $[K]$  = the stiffness matrix
- $[F]$  = the force vector

Assuming the system does not consider the damping effect, and no external force is applied to the system, then Equation 4.1 becomes

$$[M][\ddot{U}] + [K][U] = [0] \quad (4.2)$$

Further, harmonic motions are typically assumed in the structure mechanics, so  $[\ddot{U}]$  is assumed to be equal to  $\lambda[U]$ , where  $\lambda$  is an eigenvalue. Then Equation 4.2 becomes

$$[M][U]\lambda + [K][U] = [0] \quad (4.3-a)$$

In ANSYS, the finite element package used in this study, Equation 4.3-b which is equivalent to Equation 4.3-a is used to solve the classical eigenvalue problem.

$$[K]\{\Phi_i\} = \omega_i^2 [M]\{\Phi_i\} \quad (4.3-b)$$

where

$[K]$  = the stiffness matrix

$\{\Phi_i\}$  = the mode shape vector (eigenvector) of mode i

$\omega_i$  = the natural circular frequency of mode i ( $\omega_i^2$  is the eigenvalue)

$[M]$  = the mass matrix

Since the armature does not have a built-in damping mechanism, the vibration modes and the vibration frequencies of the armature are determined using Equation 4.3-b.

## 4.2. Modal Analysis of the Armature

There are two motivations that cause to perform modal analysis of the lab-scale EML armature. The study performed by Watt and Fish [25] provides the first motivation. They observed vibration of the armature during experiments conducted in 1999 at the Institute for Advanced Technology in Austin, TX. The second motivation emerges from the FEA simulation that shows the vibration of the armature legs. The FEA is created to roughly estimate the magnitude of the force required to push the armature out of the lab-scale EML. In this simulation, the legs of the armature are flapping up and down as the armature is sliding along the rail in that analysis. The



magnitude of this flapping motion is sufficiently large such that intermittent contact at the interface is evident.

Modal analyses of un-deformed and deformed armatures are performed. As shown in previous chapter, the initial contact can cause the armature to be permanently deformed. Therefore, the vibration characteristics of both the un-deformed and the deformed armature are investigated here. In addition, material properties of the armature are varied to investigate corresponding effects on the vibration frequencies and mode shapes. This information will be important in establishing guidelines for selecting material and designing the geometry of an armature.

#### **4.2.1. Geometry, Meshing, Boundary Condition, and Element**

Figure 23 shows a 3-D plot of the meshed armature that is used in this analysis. No boundary or loading conditions are applied in this FEA, since modal analysis is the study of free vibration.

At total four different armatures (one un-deformed armature and three deformed armatures) are used in the analysis. To create the deformed armature, three different magnitudes of forces (400N, 1897.5N, and 3795N) are applied at the tip of the each armature leg.

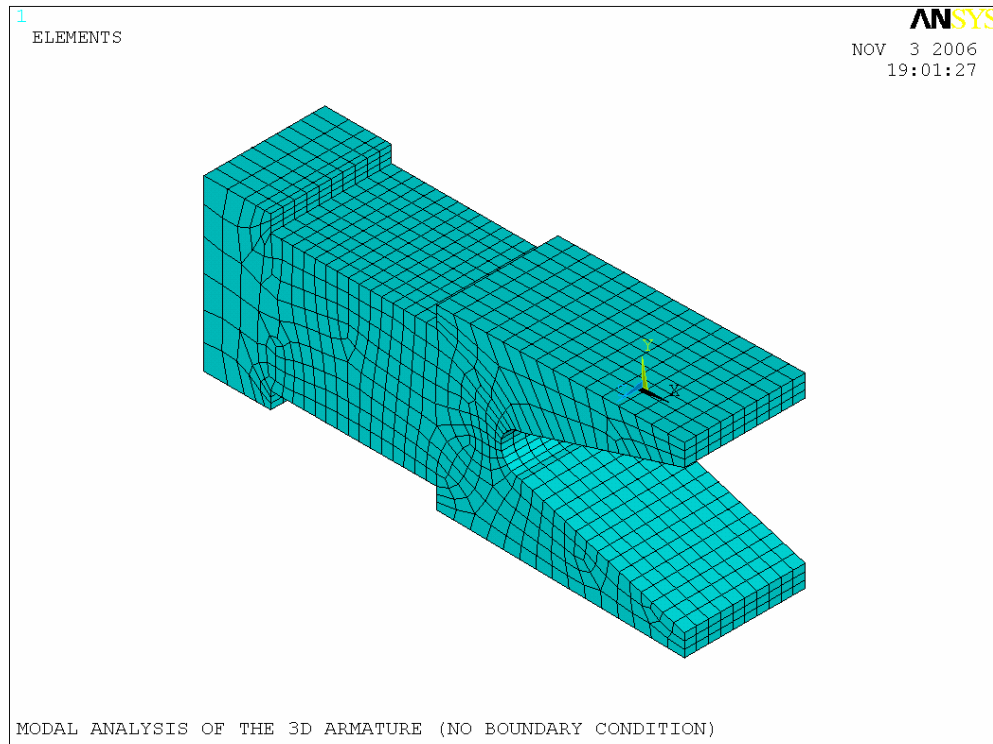


Figure 23: Mesh plot of the 3-D armature used in the Modal analysis

Figure 24 shows the schematic diagram of Solid 45. This element is used in creating a 3-D armature. This element is defined by eight nodes having three degrees of freedom at each node: translation in the nodal X, Y, and Z directions. The total number of elements used in this modal analysis was 4004.

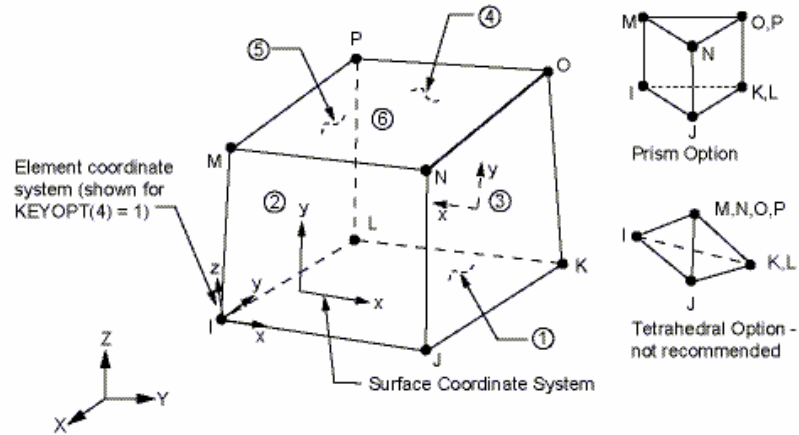
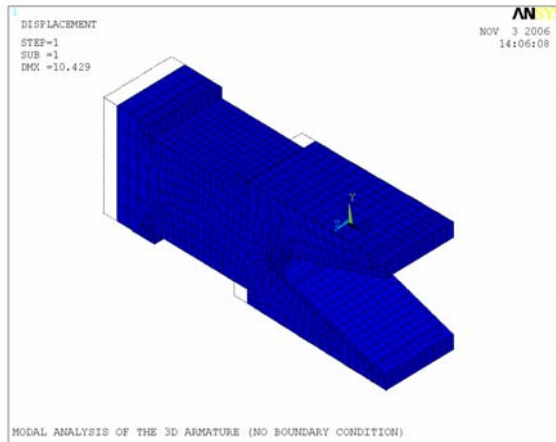


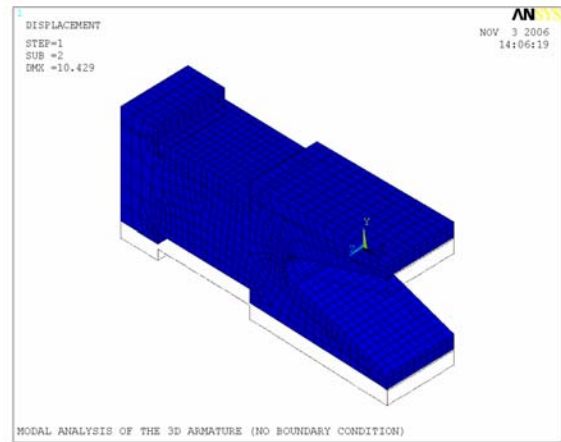
Figure 24: Schematic diagram of the Solid 45 element [22]

#### 4.2.2. Result and Discussion

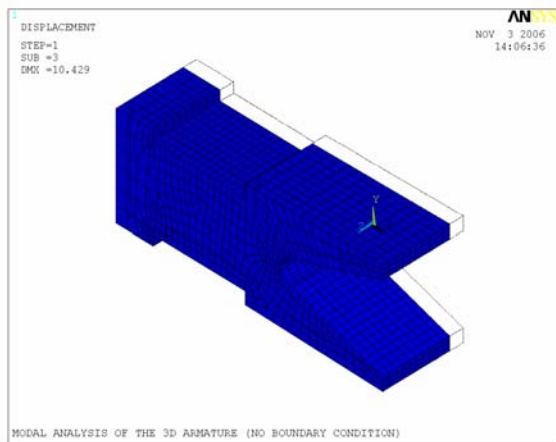
As mentioned before, no boundary and loading conditions are applied in this analysis. No boundary and condition yields six rigid body modes first. Both the undeformed and deformed armature results the same six rigid body modes. The six rigid body modes are shown in Figure 25. The first three modes represent the translation in the X, Y, and Z axes, and the next three modes represent the rotation in the X, Y, and Z axes.



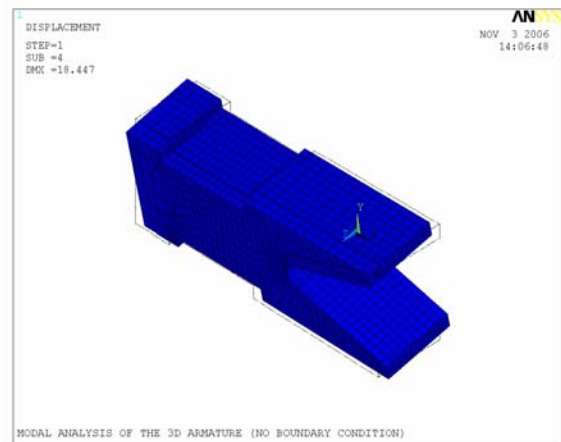
a) 1<sup>st</sup> Rigid Body Mode



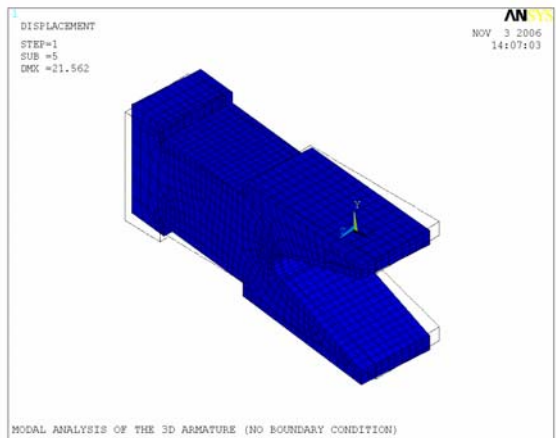
b) 2<sup>nd</sup> Rigid Body Mode



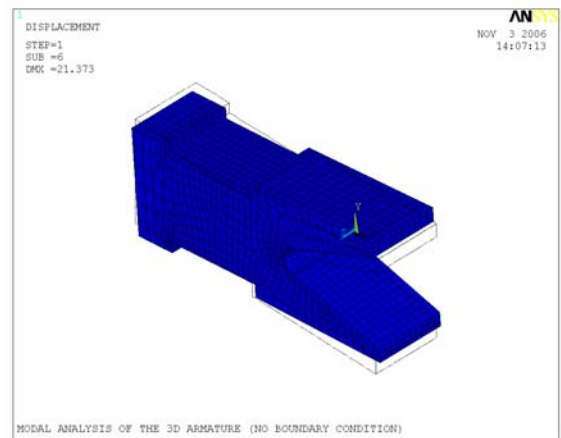
c) 3<sup>rd</sup> Rigid Body Mode



d) 4<sup>th</sup> Rigid Body Mode

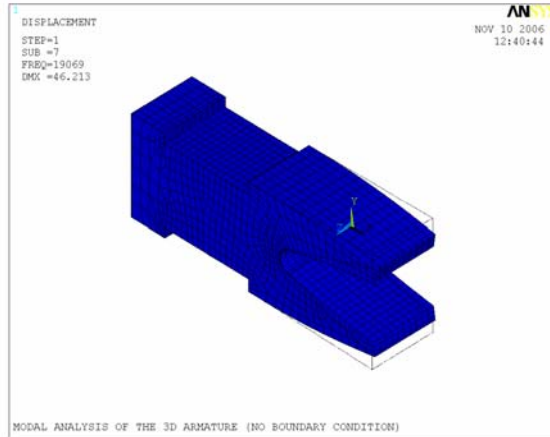


e) 5<sup>th</sup> Rigid Body Mode

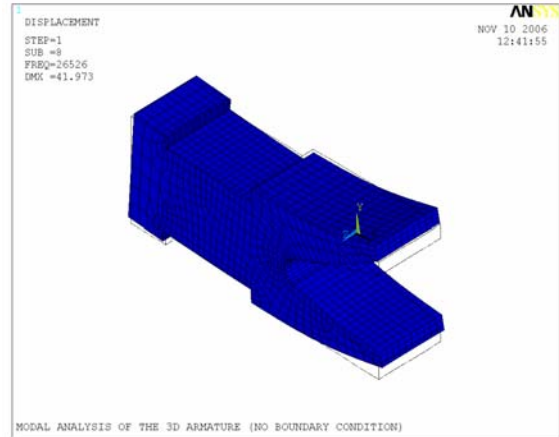


f) 6<sup>th</sup> Rigid Body Mode

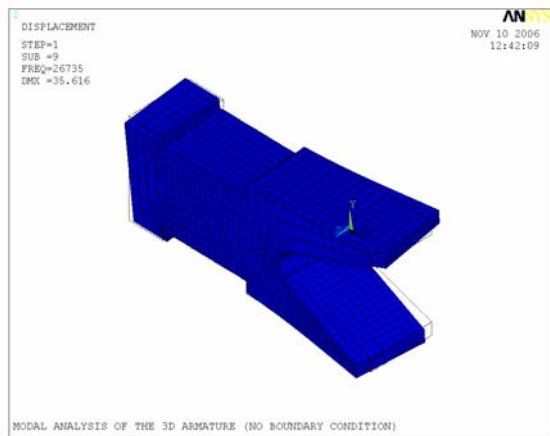
Figure 25: Six rigid body modes



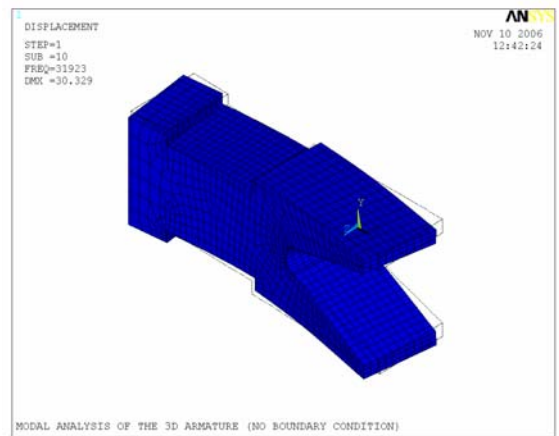
a) 1<sup>st</sup> Vibration Mode Shape



b) 2<sup>nd</sup> Vibration Mode Shape



c) 3<sup>rd</sup> Vibration Mode Shape



d) 4<sup>th</sup> Vibration Mode Shape

Figure 26: First four vibration mode shapes of the un-deformed armature

Figure 26 shows the result of the first four vibration mode shapes of the un-deformed armature. There are infinite mode shapes, however only first four mode shapes are shown here. The first vibration mode shape represents the flapping up and down motion of armature legs (out of phase motion). This is the mode shape that was mentioned at the beginning of this section. The up and down bending of the whole

armature is shown in the second mode shape (in phase motion). The opposite directions motion of the armature legs (out of phase motion) are shown in the third mode shape. If the top leg moves in the positive transversal direction (out of the page), then the bottom leg moves in the opposite direction (into the page), and vice-versa. The motion of the whole armature bending in the positive and the negative transversal direction (in phase motion) is shown in the fourth mode shape. Table 5 summarizes the frequency and the period of the first four modes of the un-deformed armature.

Table 5: Frequencies and periods of the first four modes of the un-deformed armature

<b>MODE</b>	<b>FREQ. (Hz)</b>	<b>PERIOD (Sec.)</b>
1	19069	5.25E-05
2	26526	3.77E-05
3	26735	3.74E-05
4	31923	3.13E-05

Figures 27 and 28 show the resulting displacement in the X and Y directions for the armature that experiences the 400N on each leg, respectively. Each armature leg moved inward about 0.12 mm due to the applied force.

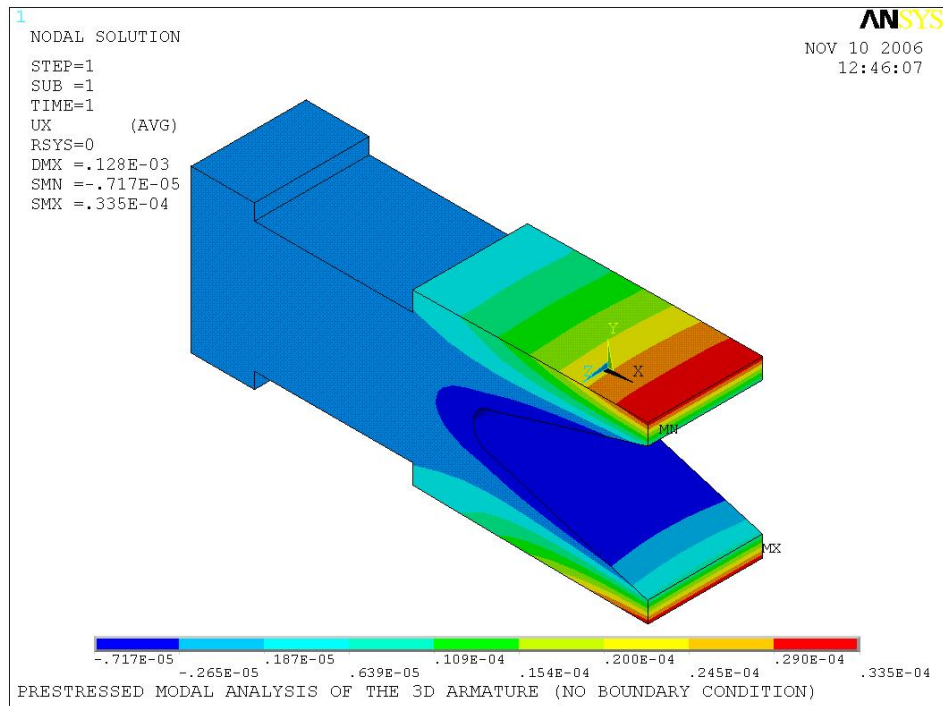


Figure 27: Results of the X direction displacement of the deformed armature

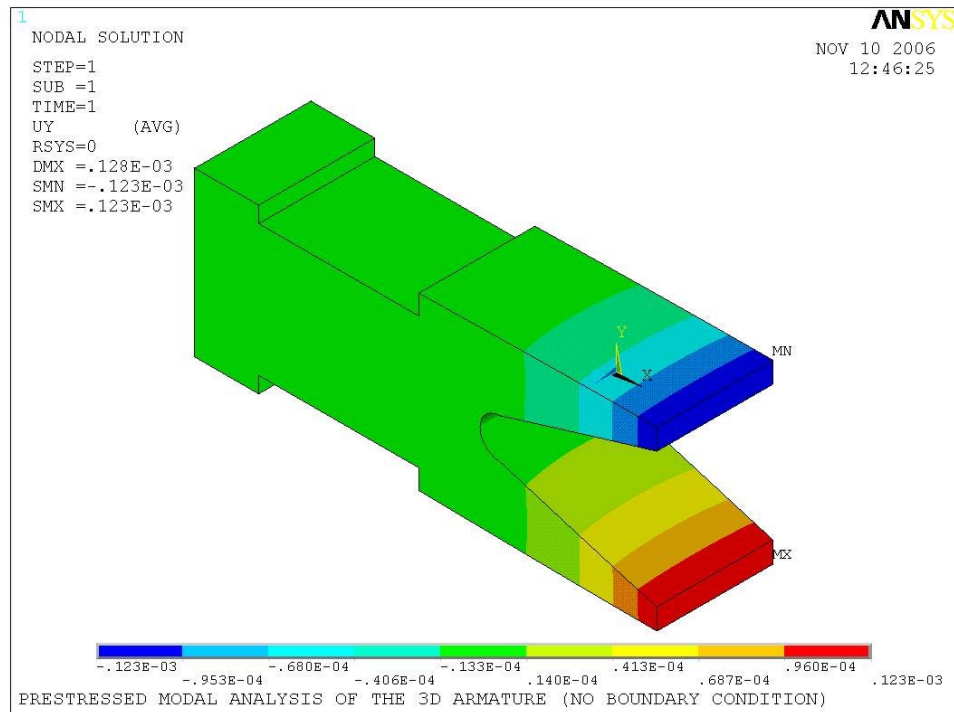
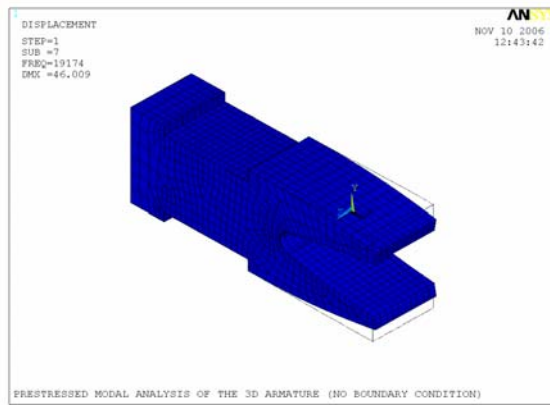
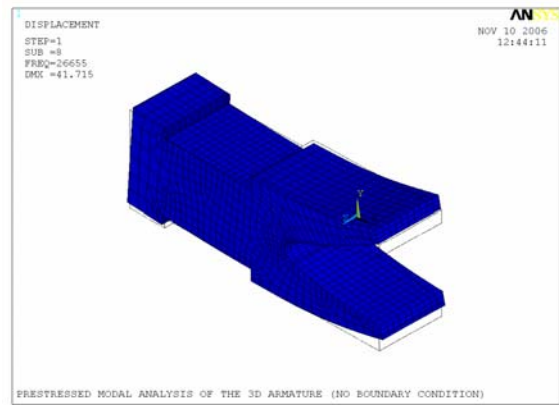


Figure 28: Results of the Y direction displacement of the deformed armature

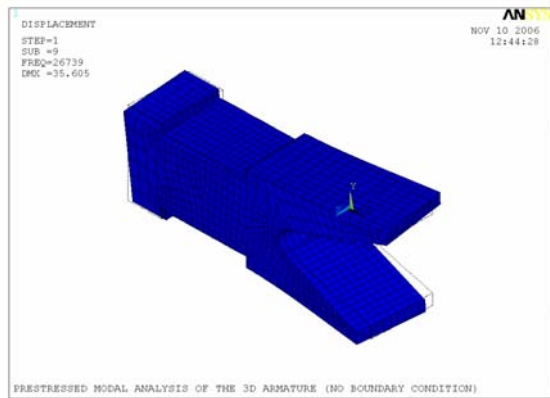
Figure 29 shows the result of the first four vibration mode shapes of the deformed armature that experiences 400 N on the each leg. These vibration mode shapes are the exactly the same as the results of the un-deformed armature. The frequency of each mode is increased slightly. A summary of the vibration frequency and the period of the first four modes of the deformed armature are given in Table 6.



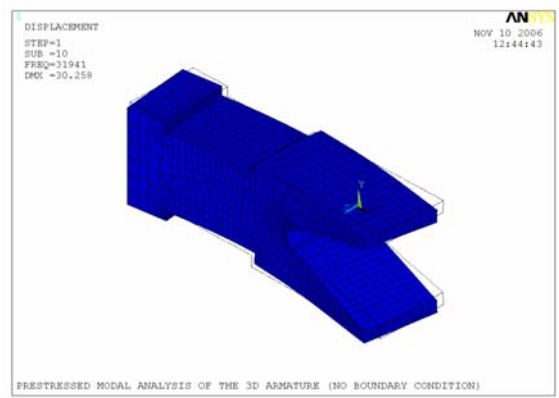
a) 1<sup>st</sup> Vibration Mode Shape



b) 2<sup>nd</sup> Vibration Mode Shape



c) 3<sup>rd</sup> Vibration Mode Shape



d) 4<sup>th</sup> Vibration Mode Shape

Figure 29: First four vibration mode shapes of the deformed armature that experiences 400 N on each leg



Table 6: Frequencies and periods of the first four modes of the deformed armature that experiences 400 N on each leg

MODE	FREQ. (Hz)	PERIOD (Sec.)
1	19174	5.22E-05
2	26655	3.75E-05
3	26739	3.74E-05
4	31941	3.13E-05

It should be noted that the first mode vibration period of both the un-deformed and the deformed armatures is significantly shorter than the typical sliding duration expected in the lab-scale EML. This means the intermittent contact can occur while the armature slides along the rail. This vibration characteristic should be considered in the future design of the armature so the performance of the lab-scale EML is improved.

To further study the vibration characteristics of the deformed armature, a higher force is applied at the each leg of the armature. Figure 30 shows a side view of the mesh plot of the deformed armature that experiences 1897.5 N on each leg. The armature legs are bent inward towards each other.

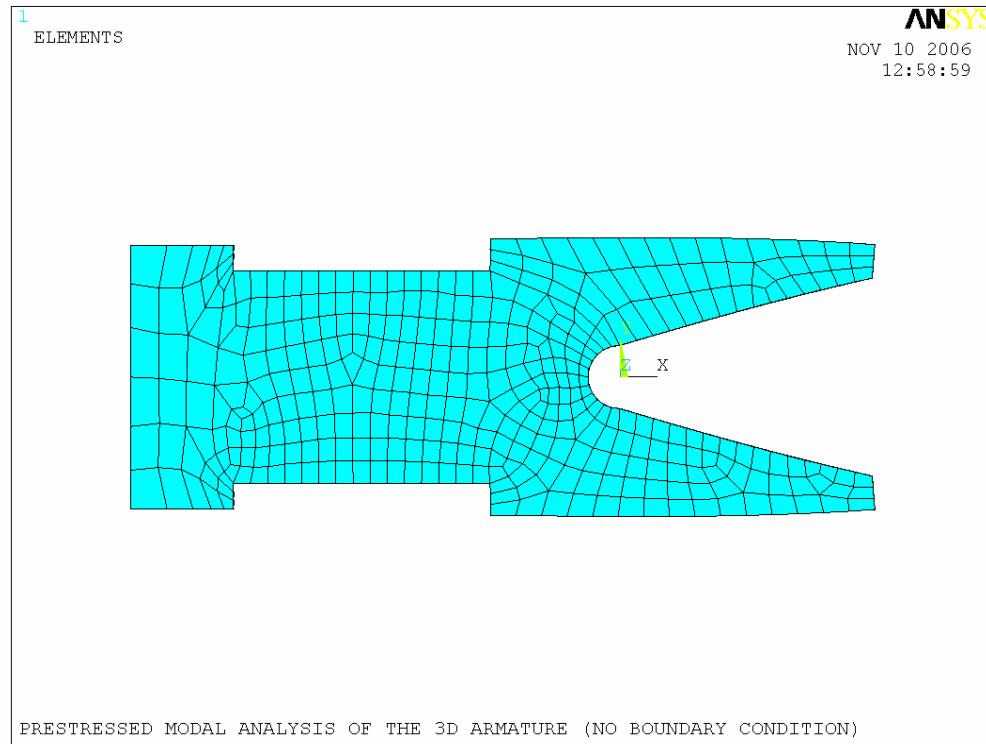
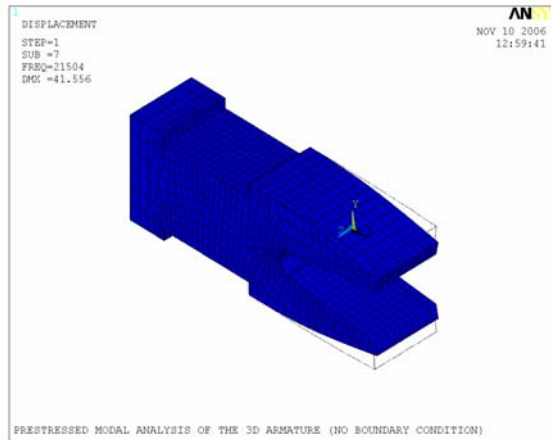
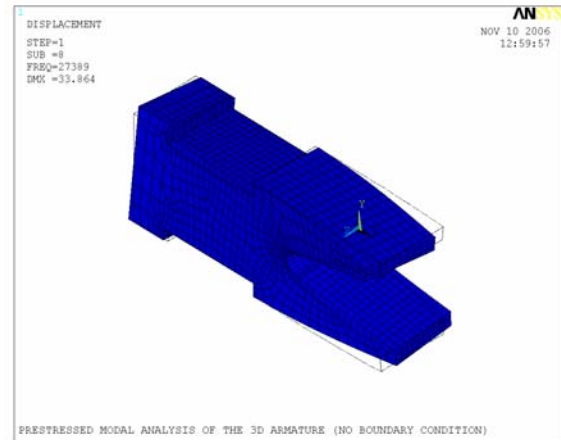


Figure 30: Mesh plot of the deformed armature that experiences 1897.5 N on each leg

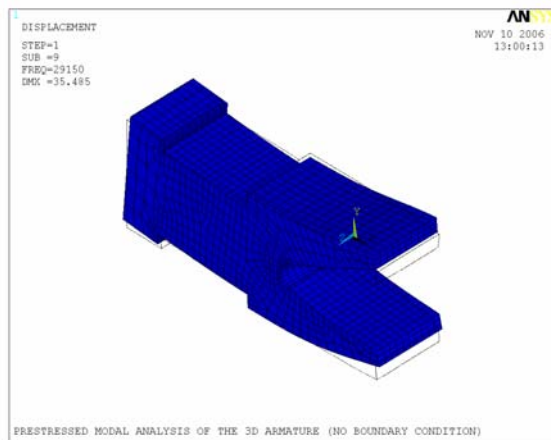
Figure 31 shows the first four vibration mode shapes of the armature that experience 1897.5N on each leg. The second vibration mode shape that is seen in two previous analyses is the third vibration mode shape for this analysis, and the third vibration mode shape that is seen in two previous analyses is the second vibration mode shape for this case. The frequency of each mode is increased further. Table 7 lists the frequency and the period of the first four modes.



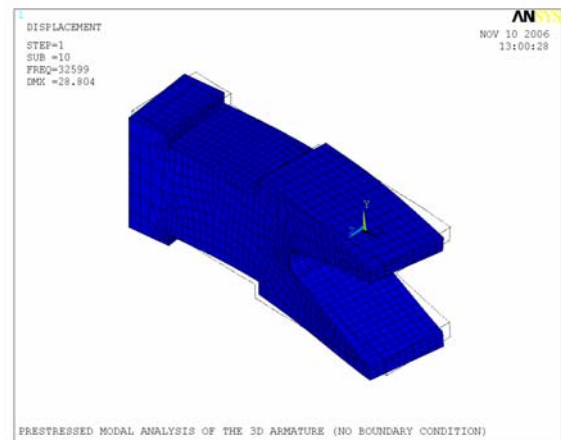
a) 1<sup>st</sup> Vibration Mode Shape



b) 2<sup>nd</sup> Vibration Mode Shape



c) 3<sup>rd</sup> Vibration Mode Shape



d) 4<sup>th</sup> Vibration Mode Shape

Figure 31: First four vibration mode shapes of the deformed armature that experiences 1897.5 N on each leg

Table 7: Frequencies and periods of the first four modes of the deformed armature that experiences 1897.5 N on each leg

MODE	FREQ. (Hz)	PERIOD (Sec.)
1	21504	4.65E-05
2	27389	3.65E-05
3	29150	3.43E-05
4	32599	3.07E-05

A higher force (3795 N) is applied at the each armature leg. The deformed armature is shown in Figure 32.

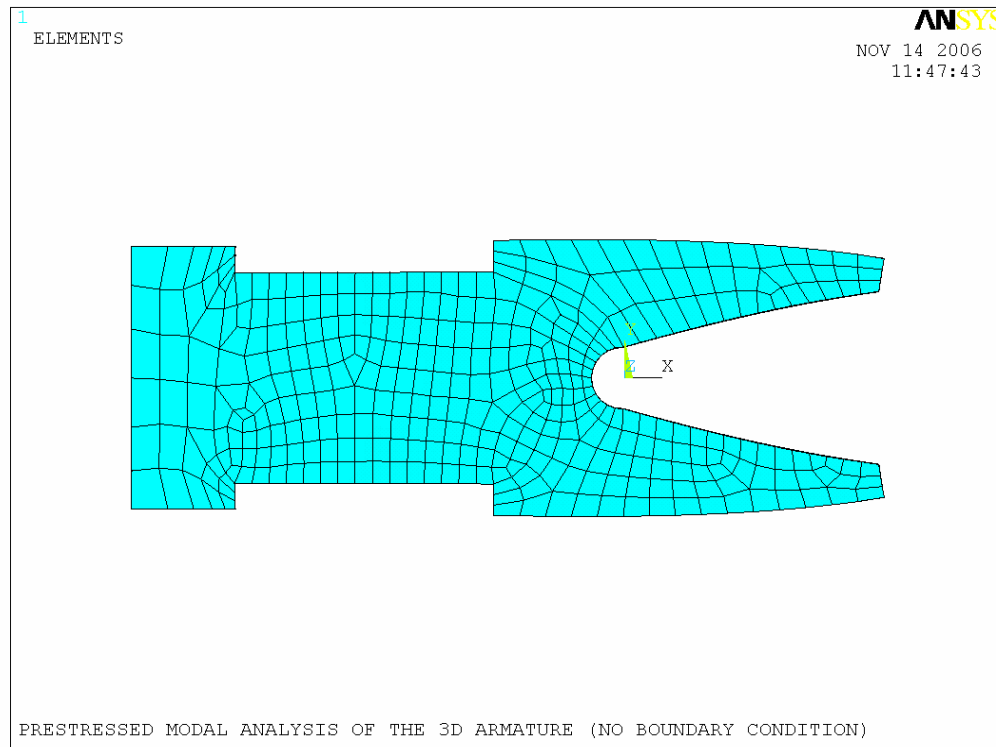


Figure 32: Mesh plot of the deformed armature that experiences 3795 N on each leg

The vibration mode shapes obtained in this analysis are exactly the same as those shown in Figure 31. A slight increase in the frequency of each mode is observed. Table 8 lists the frequency and the period of the first four vibration modes.

Table 8: Frequencies and periods of the first four modes of the deformed armature that experiences 3795 N on each leg

MODE	FREQ. (Hz)	PERIOD (Sec.)
1	25126	3.98E-05
2	28947	3.46E-05
3	32738	3.06E-05
4	34272	2.92E-05

The study of the deformed armature provides two conclusions. The first conclusion is that the higher deformation of the armature legs results in the higher vibration frequency. The second conclusion is that the vibration mode shape depends on the deformed geometry of the armature. The results of the first two analyses where the armature legs are not bent indicate the same vibration mode shape, while the last two analyses where the armature legs are bent show the same vibration mode shape.

Further investigation of the vibration characteristics is conducted to improve the material selection criteria. The material properties, the Young's modulus and the density, are varied. Although there are other material properties, these two are selected because modal analysis is one of the structural FEAs. Therefore, it is logical that structural material properties are varied. Also, the Young's modulus and the density of the material can be easily obtained for most of the materials.

The results of FEA show that the frequency is proportional to  $\sqrt{E/\rho}$ , where  $E$  is Young's modulus and  $\rho$  is the density. The mode shapes do not change, as the material properties change.

The size of the armature is also varied and the corresponding effects are observed. The length in the X, Y, and Z directions are increased by factors of 2, 5, and 10. It is found that frequency is inversely proportional to size.

The following conclusions summarize the major results obtained from the modal analysis of the armature.

1. The frequencies of the first vibration mode of the un-deformed and deformed armatures currently used in the lab-scale EML are 19069 Hz and 19174 Hz, respectively. These high frequencies can possibly create the on-and-off contact at the interface while the armature slides along the rails.
2. The vibration mode shapes depend on the geometry of the armature.
3. The vibration mode shape is not affected by Young's modulus and density.

However these material properties affect the frequency of each vibration mode.

A vibration frequency is directly proportional to  $\sqrt{E/\rho}$  and the armature size.

In the next chapter, an electromagnetic FEA is performed to determine the actual electromagnetic force created by the applied electric current coupled with the resulting electromagnetic field.

## CHAPTER 5: ELECTROMAGNETIC ANALYSIS

One of the advantages of an EML over conventional launchers is that an EML can operate without chemical explosives. This advantage is achieved by using electromagnetic force. The physics of the electromagnetic force is explained by the Lorentz force, which is the force exerted on a charged particle in an electromagnetic field as given by Equation 5.1.

$$\vec{F} = q(\vec{E} + \vec{v} \times \vec{B}) \quad (5.1)$$

where  $\vec{F}$  is the force,  $\vec{E}$  is the electric field,  $\vec{B}$  is the magnetic field,  $q$  is the electric charge of the particle, and  $\vec{v}$  is the instantaneous velocity of the particle.

When an electric current (charged particles with a drift velocity) flows in the conductor, the electric and the magnetic fields are created in the proximity of the conductor. In the EML, an electric current flows from one end of the rail to the armature and back to the other end of a second rail. This creates electric and magnetic fields, which when coupled with electric current create an electromagnetic force.

### 5.1. Electromagnetic Analysis

In this chapter, an investigation of the electromagnetic force is presented. A

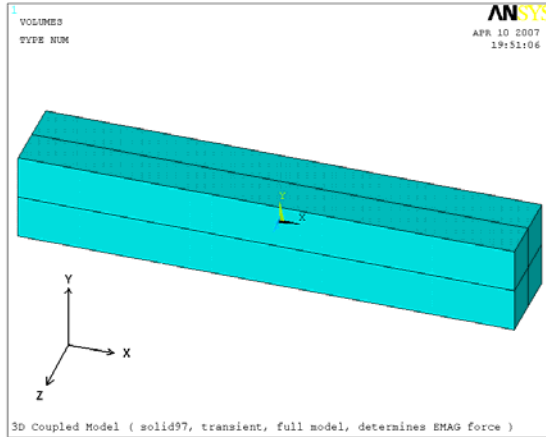


quasi-static 3-D finite element model is created for the electromagnetic FEA. The complex coupled nature of the problem is de-coupled in this study. A stationary model is employed to obtain the pseudo-electromagnetic force results.

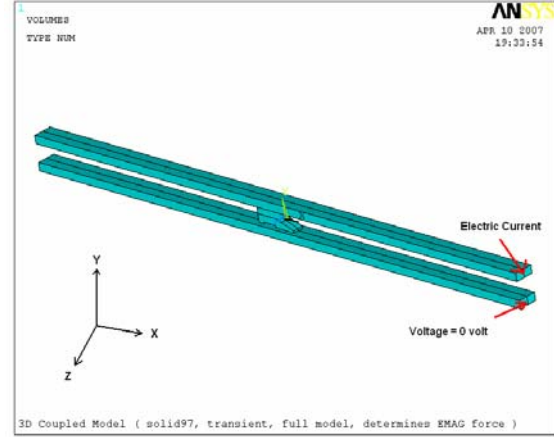
It should be noted that the full version of ANSYS is used here, so there was no limit on the number of nodes. Approximately two million elements were used in this analysis. In addition, a workstation with dual-core CPU (2.6 GHz) and 8GB memory was used in this FEA. With this workstation, the analysis took approximately 10-12 hours to perform.

#### **5.1.1. Geometry, Meshing, Boundary Condition, and Element**

Figure 33 shows a 3-D model used in this analysis. A quasi-static 3-D model contains the rails, the armature, and the air (space) where the electric and the magnetic fields reside. As shown in Figure 33, throughout the analysis, the positive X, Y, and Z coordinates are defined as to the right, to the top, and out of page, respectively. It should be noted that the armature slides towards the left (the negative X direction) in the analysis (see Figure 33-b). Therefore, it is expected that the resulting electromagnetic force on the armature should be a negative value.



a) 3-D model



b) 3-D model without air (space)

Figure 33: 3-D model used in the electromagnetic FEA

The actual sliding of the armature is not simulated in this analysis. The magnitude of the EMAG forces is calculated using the quasi-static model. The rails are modeled as 0.5 m in length, since the full length of the rails is not necessary. In addition, in order to prevent the solution from being affected by any end effects (possible interference due to the armature's placement close to the end of the rails where the current is applied), the armature is placed about 0.25 m away from the inlet. A perfect and continuous contact condition at the interface is assumed in this analysis. No additional resistance is applied at the contact interface (since any additional contact resistance normally arises due to the variation in real contact to apparent contact). In this analysis, an electric current flows from the top rail to the bottom rail. In Figure 33-

b, the surface where the electric current is applied, and the surface where zero voltage is present are indicated. At the outer surfaces of the air (space), a flux parallel boundary condition is applied. This boundary condition forces the magnetic field flux to be parallel along the six surfaces of the air, while the magnetic field flux can be freely formed anywhere within the air (space).

Figure 34 shows the electric current that is used in this analysis. This electric current is one set of actual lab-scale EML experimental data.

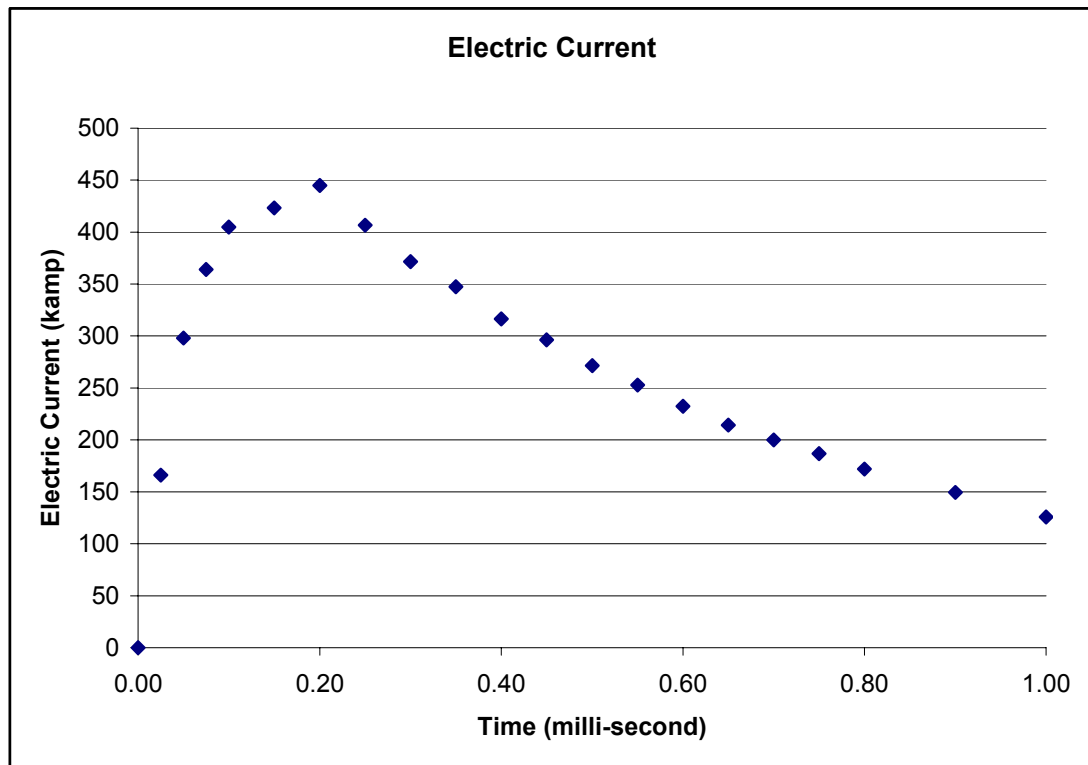
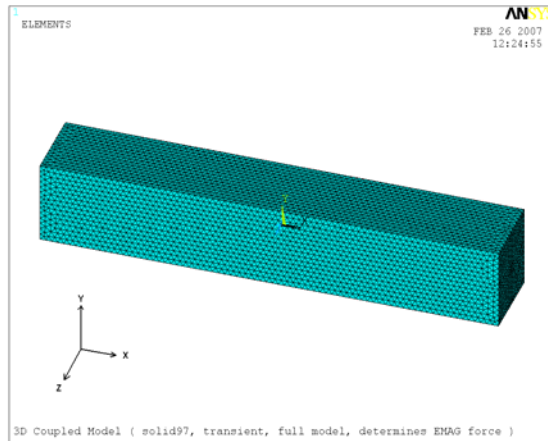
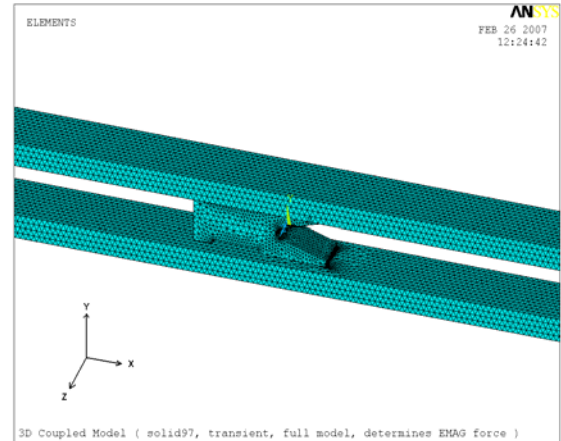


Figure 34: Plot of the applied electric current

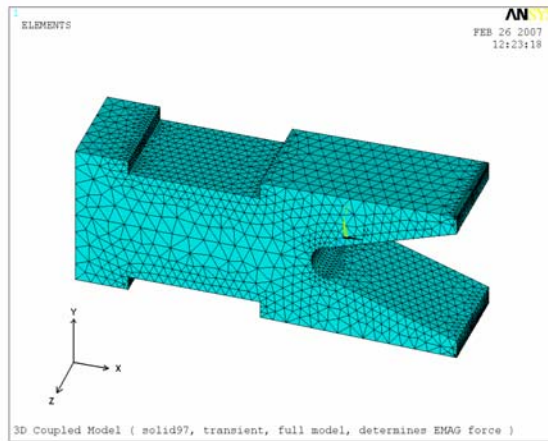
Figure 35 shows the meshed plot of the 3-D model. A finer mesh density is created around the contact region of the rails and the armature. In addition, although it is not shown, a finer mesh density is developed to account for the air between the armature legs and the rail. As shown in Figure 13 and Figure 14, the armature legs are inclined approximately  $1^\circ$  outward. This inclination creates a thin space between the outer surface of the armature legs and the inner surface of the rails. Because this space is so thin, it necessitates a fine mesh density in this region. ANSYS provided a warning message suggesting that the aspect ratio of less than 1000 of the elements could introduce a minor error in the calculation of the electromagnetic force, the effect of which should be insignificant [22].



a) Meshed 3-D model with the air (space)



b) Meshed 3-D rails and armature



c) Meshed 3-D armature

Figure 35: Mesh plot of the 3-D model used in the electromagnetic FEA

Figure 36 shows the schematic diagram of Solid 97, the element that is used in this analysis. Solid 97 models 3-D magnetic fields. It also has the thermal capability. The element is defined by eight nodes, and has up to five degrees of freedom per node (the magnetic vector potential, the time-integrated electric potential, the electric potential, the electric current, and the electromotive force).

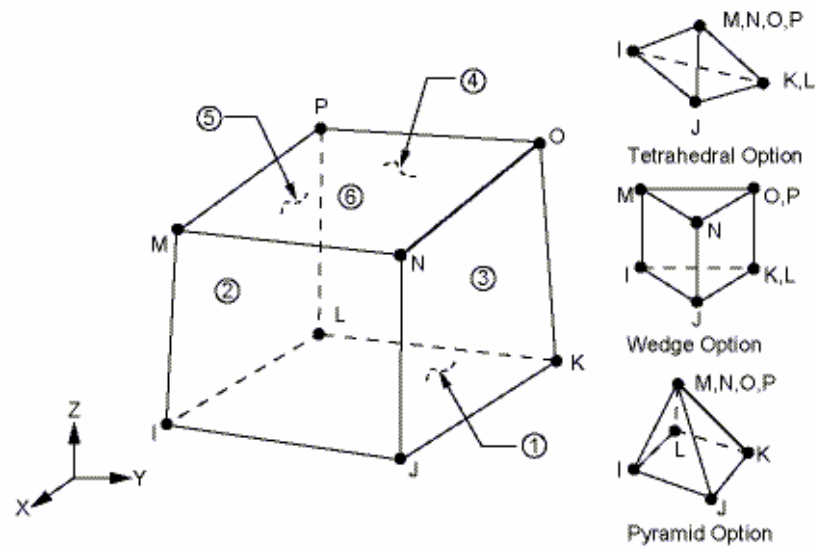


Figure 36: Schematic diagram of the Solid 97 element [22]

### 5.1.2. Result and Discussion

In relation to Figure 35, Table 9 shows the definition of the direction used in this section. In the X direction, negative means forward (left) and positive means backward (right). In the Y direction, negative means downward and positive means upward. In the Z direction, negative means into the page and positive means out of the page.

Table 9: Definition of the coordinate/direction as shown in Figure 35

Direction	Negative	Positive
X	Forward	Backward
Y	Downward	Upward
Z	Into the Page	Out of the Page

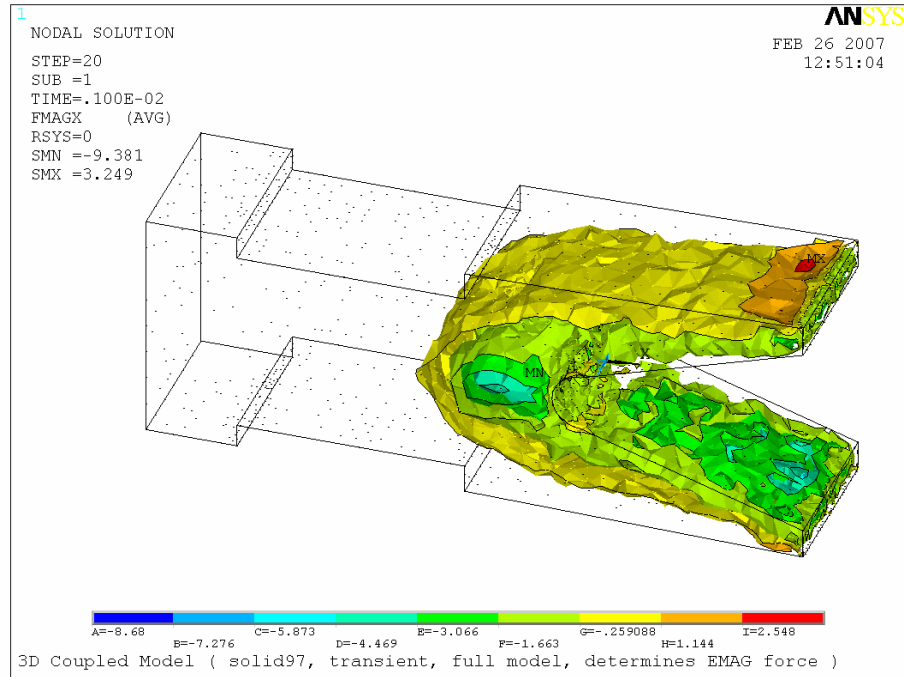
The electric current given in Figure 34 results in an EMAG force acting on the armature is summed up and given in Table 10. As expected, a large EMAG force is obtained in the negative X direction. For the Y and the Z direction, the EMAG force in the armature is well balanced and its magnitude is almost negligible compared to the X direction EMAG force. This shows that the resulting EMAG force is going to push the armature in the negative X direction towards the outlet of the EML. Theoretically, summation of the resulting EMAG force in the Y direction and the Z direction should be zero. As shown in Figure 13 and Figure 14, there is a thin gap between the armature legs and the rails due to the small inclination at the armature legs. The gap is so thin (although a very fine mesh is used to model the air between the armature legs and the rails) that the appropriate element aspect ratio can not be achieved. The detail distribution of the EMAG force is shown in Figure 37 through Figure 39. These results occur due to an applied electric current of 125828 ampere.

Table 10: Summation of the resulting EMAG force of the armature

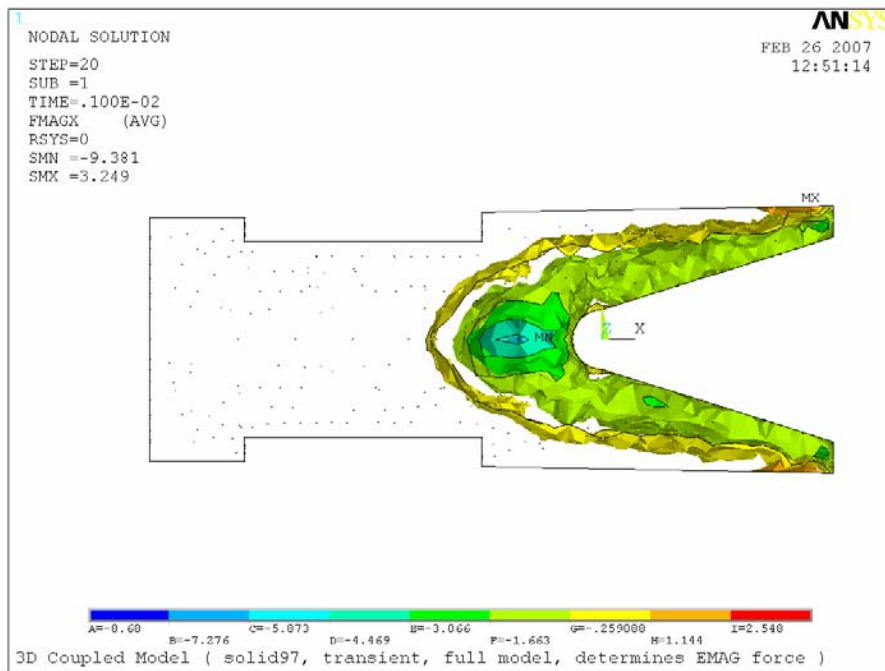
Time (ms)	Current (ampre)	ARMATURE		
		FMAG_X (N)	FMAG_Y (N)	FMAG_Z (N)
0	0	0	0	0
0.025	165988	-2834.11	0.21293	-8.97973
0.050	298098	-17531.6	-19.2978	-46.8886
0.075	364017	-31447.4	-38.2116	-64.6879
0.100	404855	-41293	-44.8651	-80.7321
0.150	423360	-49945	-56.9143	-88.316
0.200	444809	-54653	-65.5495	-98.1229
0.250	406464	-52363.4	-56.5056	-88.5162
0.300	371716	-44090.3	-46.6044	-76.1814
0.350	347224	-38552.9	-39.4061	-58.8042
0.400	316526	-33249.9	-32.4998	-47.8632
0.450	296319	-28819.6	-26.5838	-38.4387
0.500	271350	-24994.3	-23.6404	-30.4982
0.550	252812	-21548.3	-19.4301	-25.0466
0.600	232381	-18635.4	-17.3421	-19.6851
0.650	214269	-15916.7	-14.5126	-16.1998
0.700	200041	-13814.5	-12.93	-12.6928
0.750	186802	-12103.1	-11.2997	-10.5334
0.800	171794	-10440.7	-9.8762	-8.75393
0.900	149369	-8144.23	-8.00703	-6.13986
1.000	125828	-6006.57	-6.01278	-4.03004

Figure 37 shows the iso-surface contour plots of the resulting EMAG force on the armature in the X direction. The major portion of the resulting EMAG force resides in the legs of the armature. As expected, the negative EMAG force is distributed along the inner edges of the armature legs. However, the result shows that a thin layer of the positive EMAG force is also distributed in the armature. This layer is located between the negative EMAG force layer and the body of the armature. As mentioned earlier, because the magnitude of the negative EMAG force is much greater compared to the positive EMAG force, the armature will slide in the negative X direction towards the outlet of the EML.



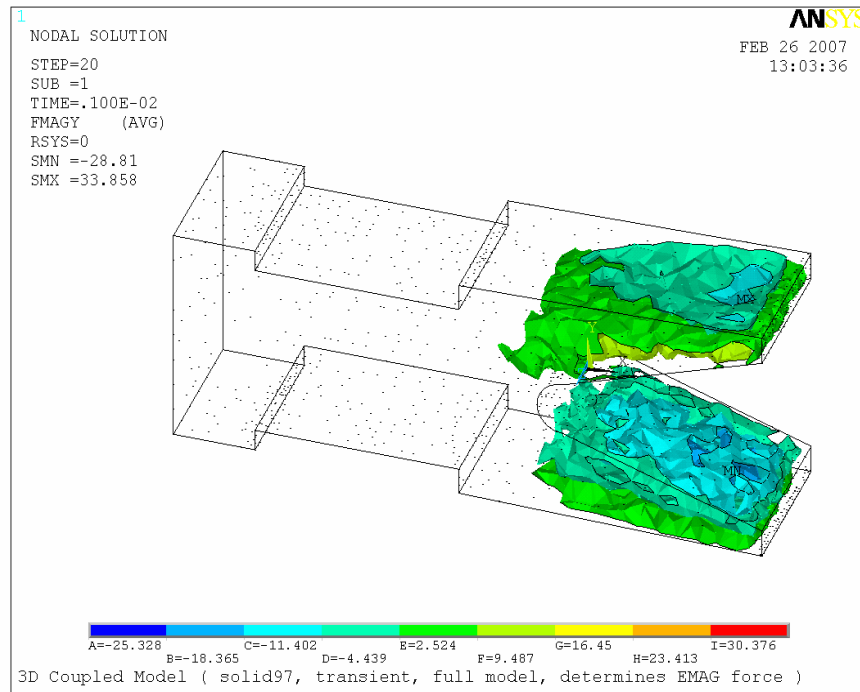


a) Overall view

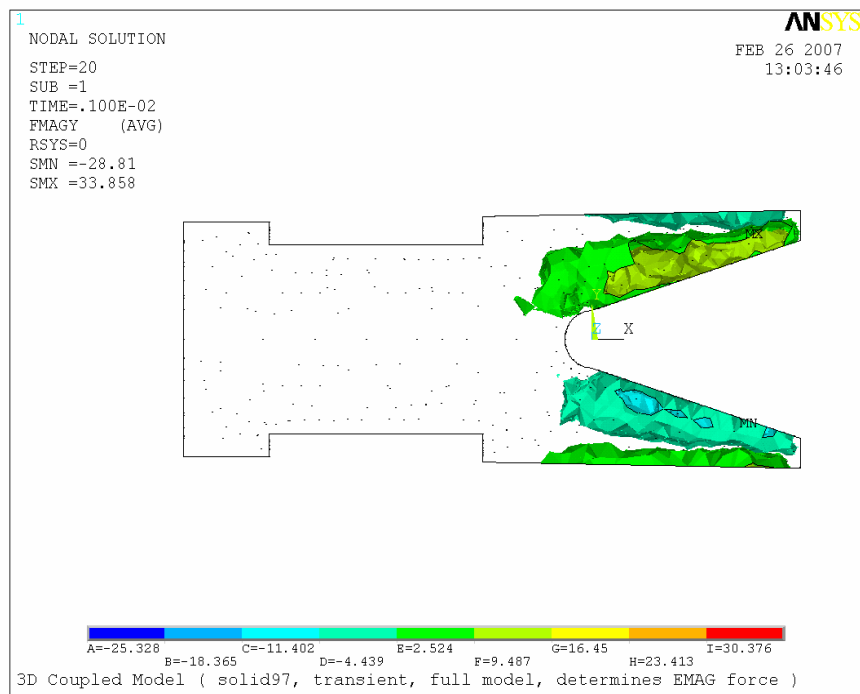


b) Side view

Figure 37: Iso-surface contour plots of the resulting X direction EMAG force of the armature



a) Overall view

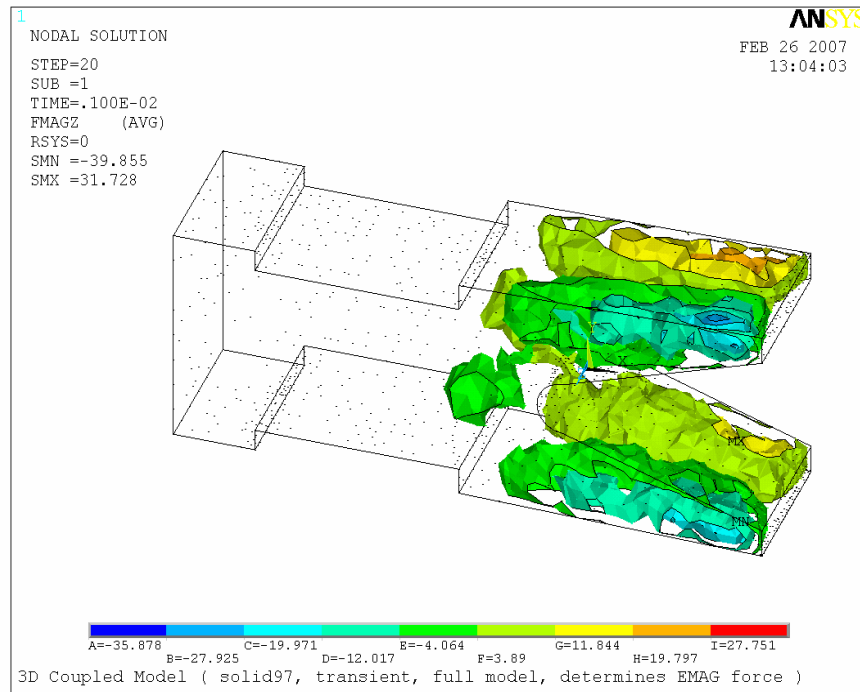


b) Side view

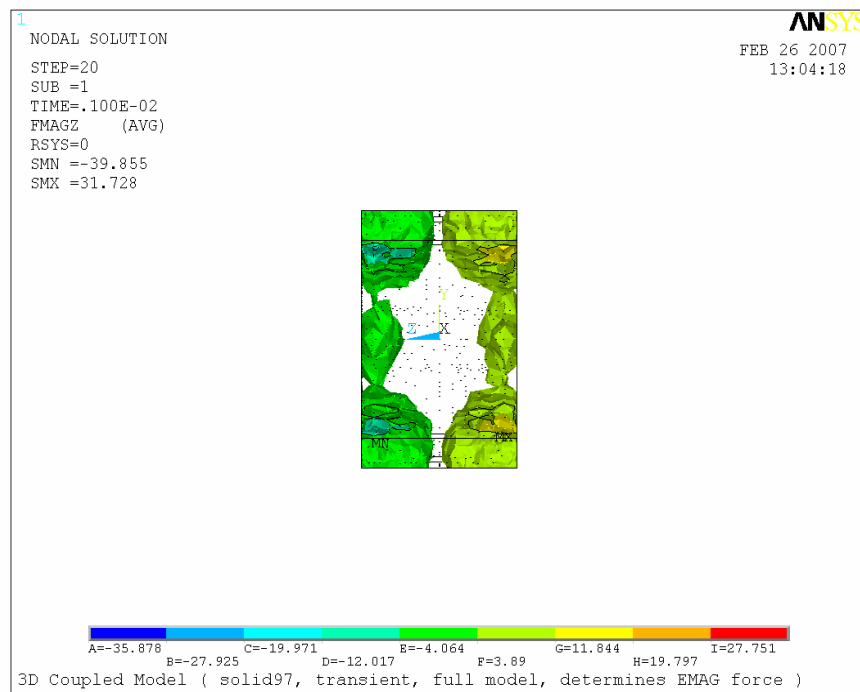
Figure 38: Iso-surface contour plots of the resulting Y direction EMAG force of the armature

Similar to the X direction EMAG force, Figure 38 shows that each armature leg experiences both a positive and negative EMAG force in the Y direction. For the upper leg, the positive EMAG force (upward) is greater than the negative EMAG force, and this will cause the upper armature leg to bend upward. For the lower leg, the negative EMAG force (downward) is greater than the positive EMAG force, and this will cause the lower armature leg to bend downward. This trend matches experimental observations. The asymmetry in the results is believed to be caused by numerical round-off (compared to the large magnitude of the force in the X-axis direction)

As shown in Figure 39, the Z direction EMAG force is distributed such that the sides of the armature is pulled outward, therefore a tensile stress is created in the armature. The majority of the force is distributed along the sides and the inner core of the armature does not experience any EMAG force.



a) Overall view



b) Side view

Figure 39: Iso-surface contour plots of the resulting Z direction EMAG force of the armature

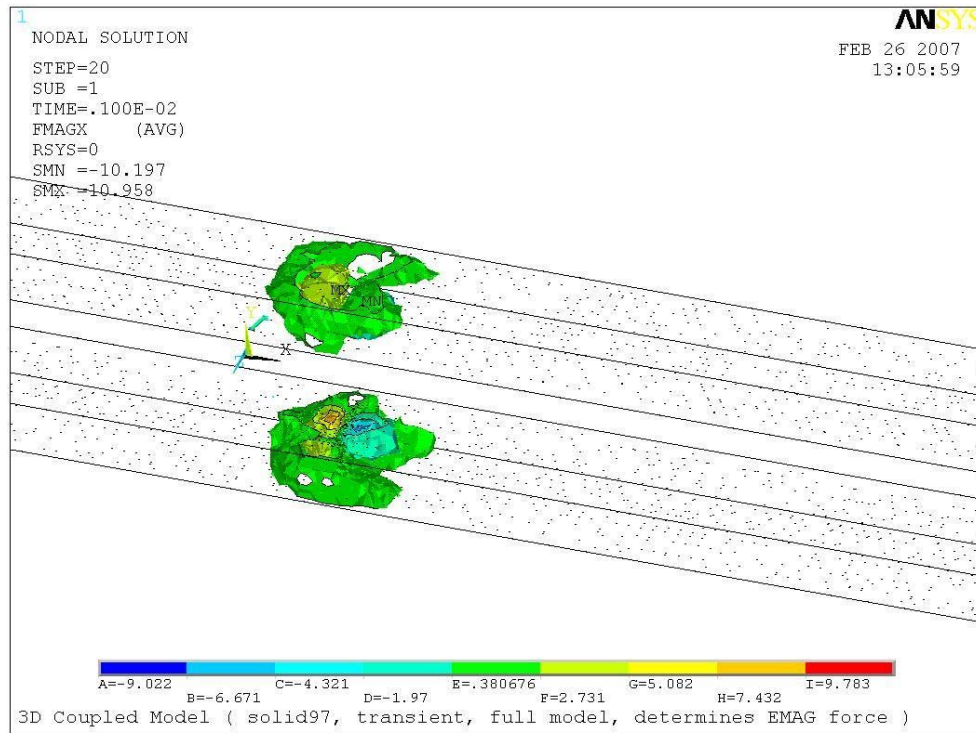
Table 11 provides the summation of the resulting EMAG forces for the top and the bottom rails. As the theoretical calculation predicts, the top rail experiences positive Y direction forces and the bottom rail experiences negative Y direction forces. The magnitudes of these forces in two rails are about the same. In the X direction, both the top and the bottom rails experience essentially the same magnitude of force in the positive X direction. The resulting X direction EMAG force is concentrated near the contact interface. This means that as the armature slides along the rails, the rails experience an X direction EMAG force opposite in direction to the armature sliding direction. In the Z direction, although the magnitude is relatively small compared to both the X and the Y directions, the top and the bottom rails experience a different magnitude of force in the opposite direction. Since the magnitude is small, it is possibly the results of numerical noise. Since the forces that the rails experience can deflect and deform the rails and cause loss of armature contact, these forces must be considered in designing an EML.

Table 11: Summation of the resulting EMAG force of the top and the bottom rails

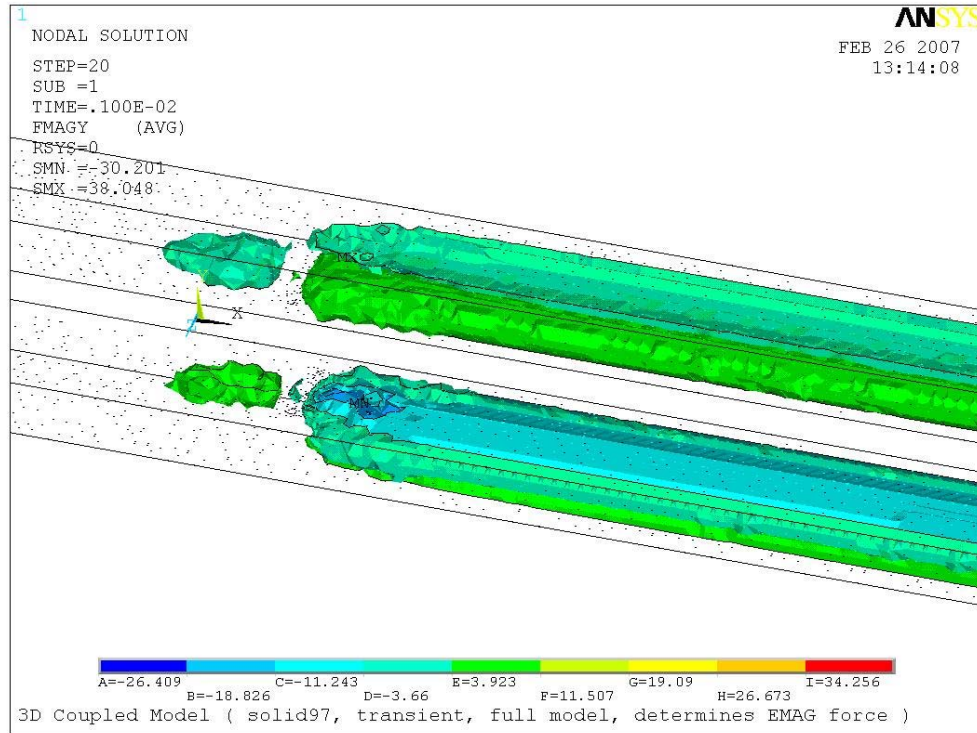
Time (ms)	Current (ampere)	TOP RAIL			BOTTOM RAIL		
		FMAG_X (N)	FMAG_Y (N)	FMAG_Z (N)	FMAG_X (N)	FMAG_Y (N)	FMAG_Z (N)
0.025	165988	38.7836	16105.4	-56.5587	39.0832	-16289.3	20.7522
0.050	298098	459.077	116698	-287.849	453.747	-117526	-101.088
0.075	364017	1109.38	227801	-451.999	1122.2	-228694	-179.592
0.100	404855	1670.17	302533	-535.127	1699.76	-303319	-79.2745
0.150	423360	2363.95	367540	-530.672	2400.98	-368138	3.40728
0.200	444809	2862.63	388968	-469.12	2899.41	-389471	85.6183
0.250	406464	2988.71	363836	-367.497	3018.09	-364218	96.1931
0.300	371716	2710.43	296430	-242.807	2733.06	-296718	109.324
0.350	347224	2487.78	249857	-177.729	2503.62	-250093	74.6235
0.400	316526	2249.21	210540	-131.843	2260.76	-210743	67.72
0.450	296319	2015.29	177818	-97.3366	2025.53	-178001	59.5995
0.500	271350	1800.89	151450	-73.8583	1808.49	-151618	56.6931
0.550	252812	1590.38	128237	-54.2874	1597.27	-128393	54.1544
0.600	232381	1404.72	109298	-40.9552	1410.25	-109442	50.5763
0.650	214269	1222.99	92118.7	-29.4285	1227.68	-92252.4	48.1841
0.700	200041	1078.25	79000.5	-22.5101	1082.54	-79123.8	42.8615
0.750	186802	959.247	68744.1	-17.9392	962.968	-68858.5	39.6791
0.800	171794	839.124	58899.3	-13.3384	842.408	-59004	37.2835
0.900	149369	666.861	45606.5	-8.41872	669.523	-45692.6	31.1351
1.000	125828	501.888	33280.8	-4.57223	503.857	-33349.6	24.9495

The detailed distribution of the EMAG force in the rails can be seen in Figure 40 for an applied electric current of 125828 ampere. As with the case of the armature, each rail experiences both positive and negative EMAG forces. For the top rail, the magnitude of the positive Y direction EMAG force is greater than the negative Y direction EMAG force. For the bottom rail, the magnitude of the negative Y direction EMAG force is greater than the positive Y direction force. Therefore, there is a repelling force in the Y direction between the top and the bottom rails. Both rails experience an X direction EMAG force near the contact interface between the armature and the rails. For the Z direction, the EMAG force is distributed similar to the case of

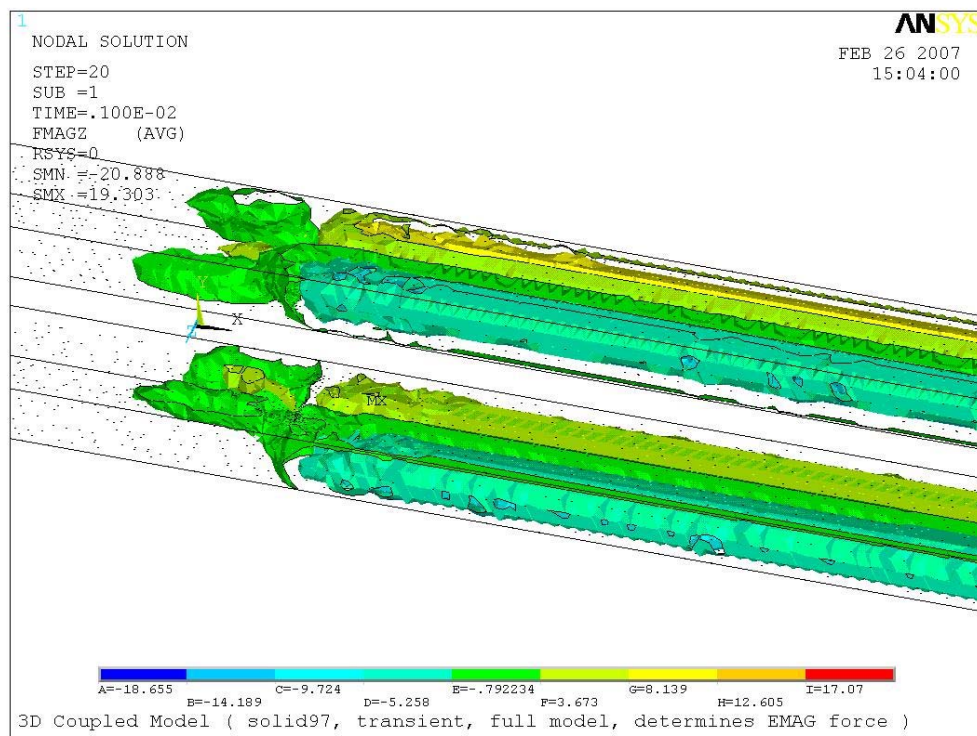
the armature. The Z direction EMAG force pulls the sides of the rails and creates a tensile stress in the rails. The inner section of the rail does not experience the Z direction EMAG force.



a) In the X direction (Rest of Figure 40 are shown in the next page)



b) In the Y direction



c) In the Z direction

Figure 40: Iso-surface contour plots of the resulting EMAG force of the rails in the X, Y, and Z directions



Newton's second law of motion states that the time rate of change of a body's momentum is proportional to the resultant force acting on the body and is in the same direction. The time rate of change of momentum can be interpreted as the product of the mass of the body and its acceleration. Therefore, the X direction EMAG force results provided in Table 10 are divided by the mass of the armature, and the acceleration of the armature is determined as a function of time. It should be noted that a maximum acceleration,  $\sim 5.5 \cdot 10^6 \text{ m/s}^2$ , of the armature occurs at  $\sim 0.2 \text{ ms}$ . Acceleration is then integrated in time, resulting in the velocity of the armature. Once the calculated velocity is integrated again in time, the displacement of the armature as a function of time is determined. Figure 41 and Figure 42 show the calculated velocity and the calculated displacement of the armature, respectively.

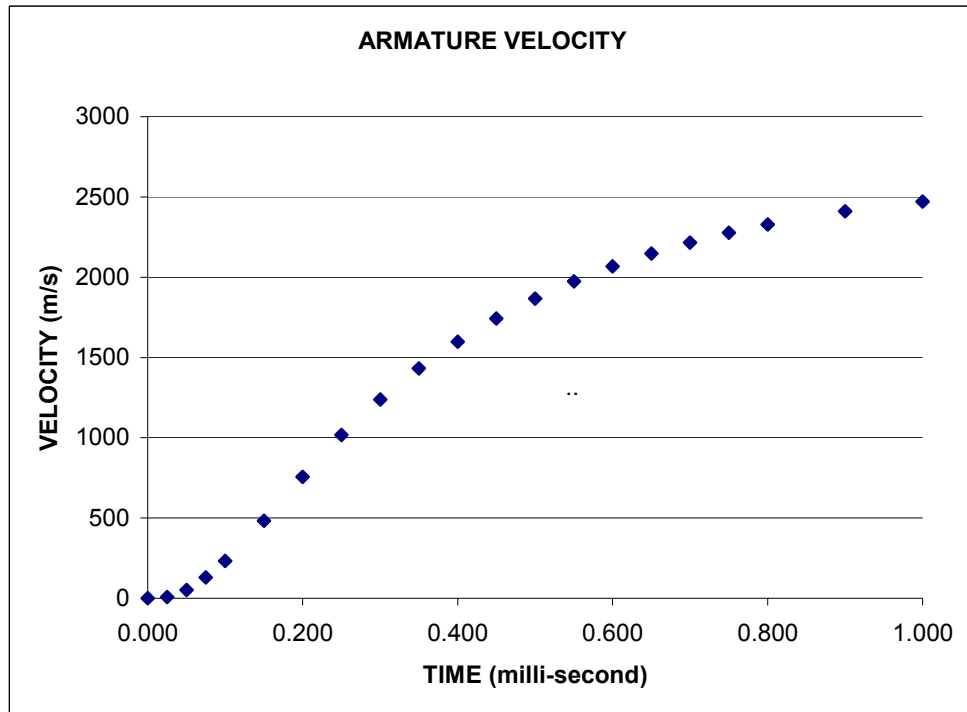


Figure 41: Calculated armature velocity as a function of time

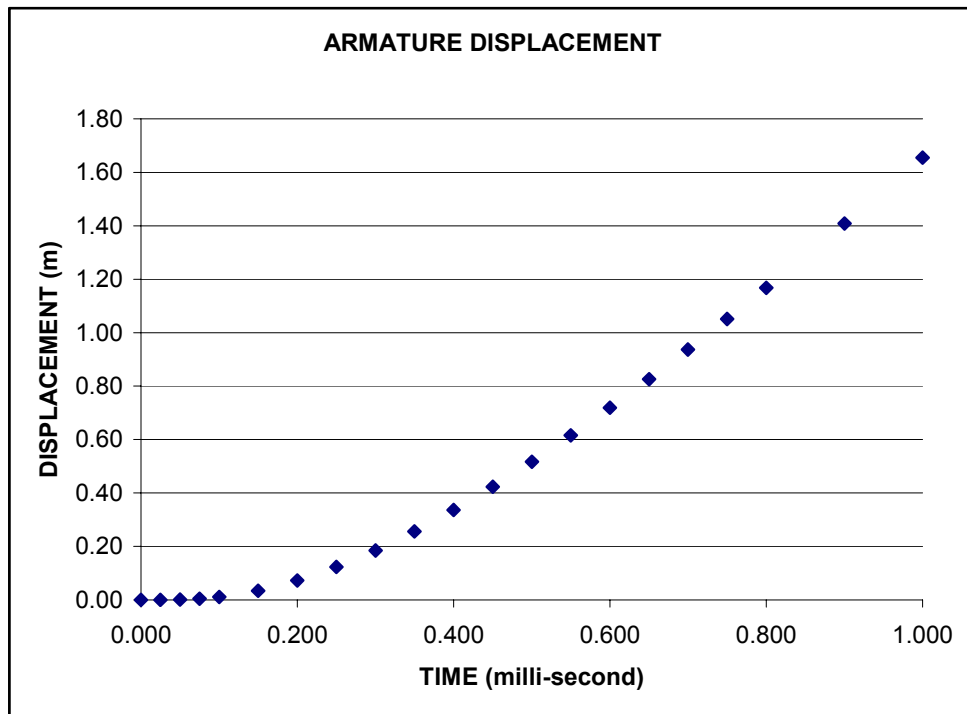


Figure 42: Calculated armature displacement as a function of time

The velocity result shown in Figure 41 is consistent with the experimental velocity. The electric current shown in Figure 34 was applied in the experiment. The maximum velocity measured in that experiment was approximately 2500 m/s. This is an unexpected result. Due to following reasons, the maximum velocity that is calculated using the FEA results is expected to be higher than the experimental velocity. First, the analysis assumes that the armature legs and the rails are in continuous contact throughout. In the actual EML, the contact between the armature legs and the rails is not expected to be continuous. Therefore, the FEA should results a higher velocity compared to the experimental measurement. Second, the complete eddy current effect is not considered in the analysis, since the model used in this analysis is a stationary model. An eddy current is an electric phenomenon which is caused when a moving magnetic field intersects a conductor, or vice-versa. The relative motion causes a circulating flow of electrons, or current, within the conductor. These circulating eddies of current create electromagnets with magnetic fields that oppose the effect of the applied magnetic field. Since the steel containment is not modeled in the analysis, the FEA result should be higher than the experimental measurement. Lastly, the armature is placed in the middle of the rails throughout the analysis. Therefore, this analysis does not consider any possible end effects. Thus, it is recommended that future work be

directed toward obtaining a better understanding of these effects.

Equation 5.1 indicates that regardless of the direction of current flow, the EMAG force must push the armature in the negative X direction (towards the exit of the EML). The physics behind Equation 5.1 is shown in Figure 43. The left diagram represents the case in which the electric current flows from the top rail to the bottom rail. The right diagram represents the reverse case. As the direction of current changes, the direction of the magnetic field also changes. Therefore, regardless of the direction of the electric current flow, the EMAG force pushes the armature in one direction.

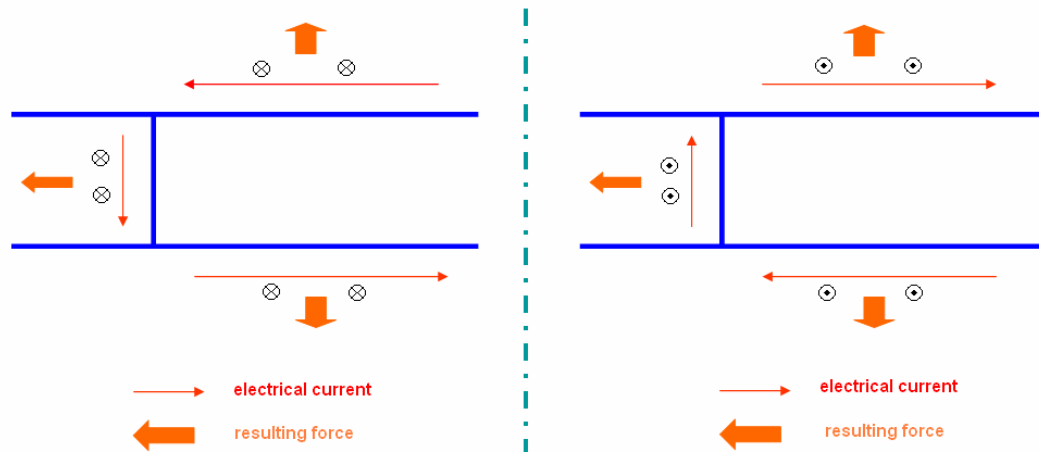
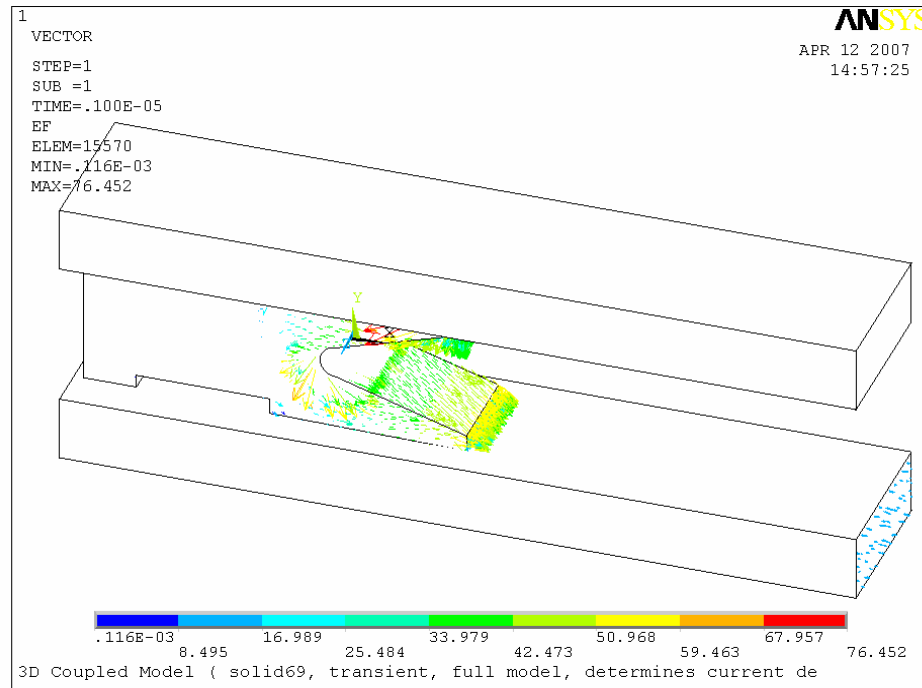


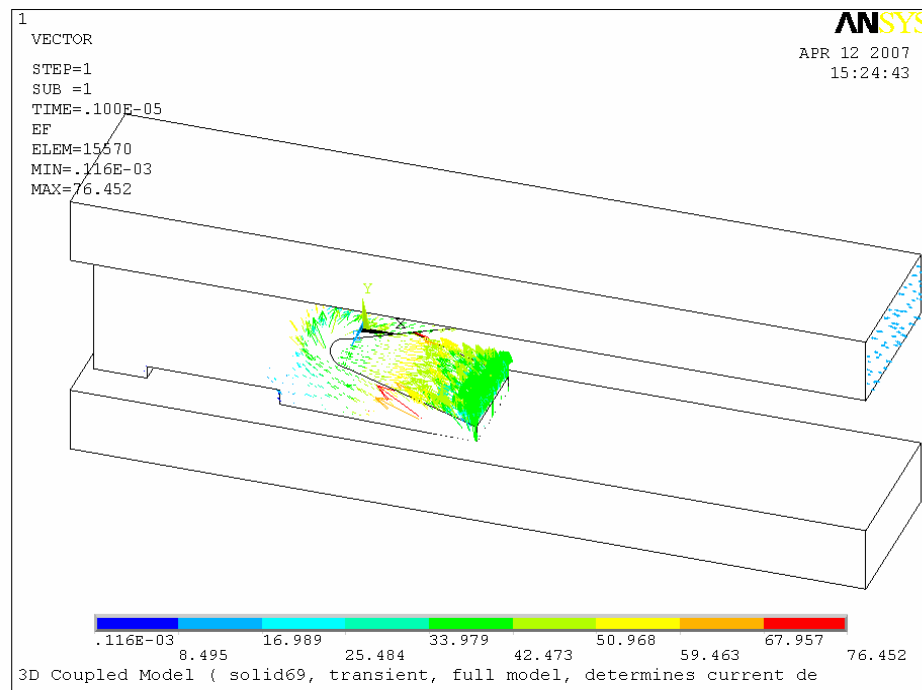
Figure 43: Schematic diagram of resulting EMAG force for different direction current flow

This fact is checked in the FEA. A clockwise and counter clockwise directional electric current is applied. Since this is a verification analysis, a simpler model is used to save on the computational time. Figure 44 shows the resulting electric field. The vectors shown in Figure 44 illustrate different directional electric current flow. In Figure 44-a, the vectors show that the electric field starts from the top rail and ends at the bottom rail. In Figure 44-b, the opposite electric current flow is shown. The magnitude of the resulting electric field is the same for both cases.

Figure 45 shows the resulting X direction EMAG force of the armature for these two cases. The identical X directional force distributions is created in both cases. Although it is not shown, the Y and the Z direction EMAG force results are also identical for both cases. The summation of the EMAG force of the armature for two cases is shown in Table 12.

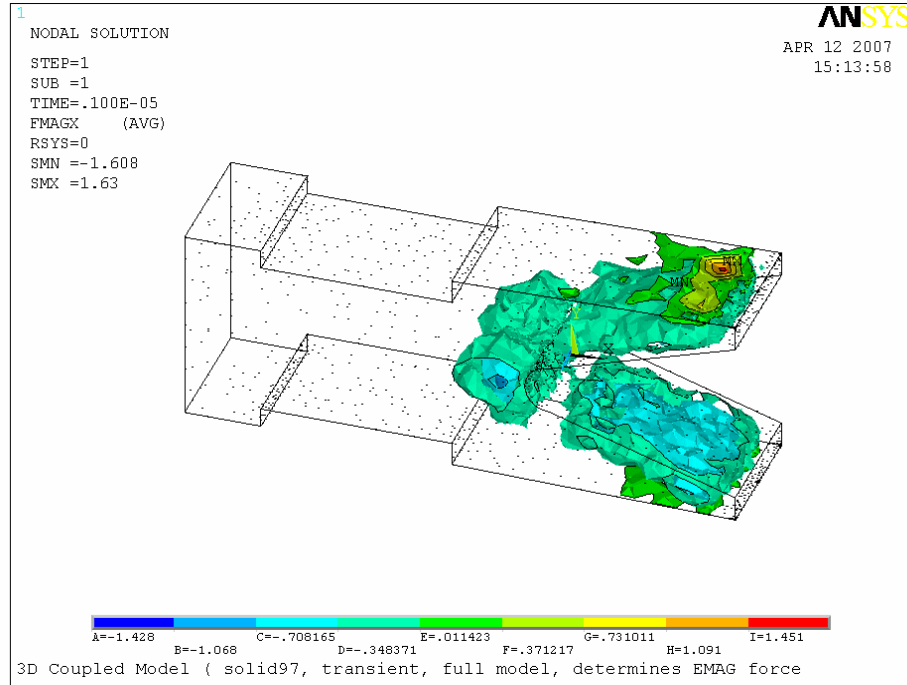


a) Current flows from the rail top to the bottom rail

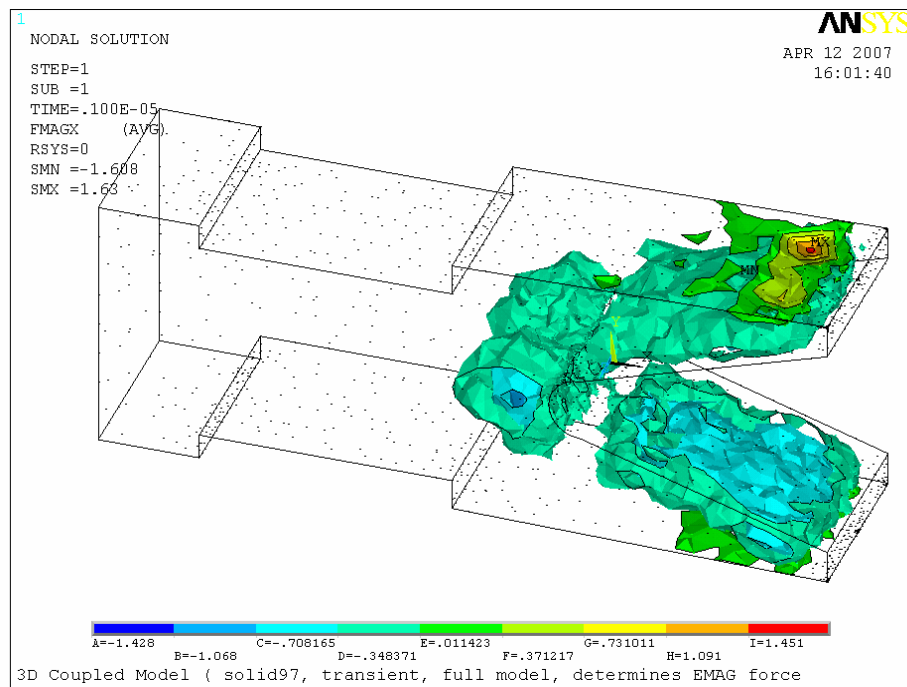


b) Current flows from the bottom rail to the top rail

Figure 44: Vector plots of the electric field for top-to-bottom and bottom-to-top directional electric current



a) Current flows from the rail top to the bottom rail



b) Current flows from the bottom rail to the top rail

Figure 45: Comparison of the resulting EMAG force of the armature in the X direction for top-to-bottom and bottom-to-top direction electric current flow

Table 12: Summation of the EMAG force for top-to-bottom and bottom-to-top directional electric current flow

Current Direction	FMAG_X (N)	FMAG_Y (N)	FMAG_Z (N)
Top to Bottom	-1193.02	0.4463	9.45017
Bottom to Top	-1193.02	0.4463	9.45017

This FEA result proves that the resulting EMAG force is always in one direction regardless of the direction of the electric current flow.

The following conclusions summarize the major findings of the electromagnetic analysis.

1. An electromagnetic force results from an applied electric current as determined from the electromagnetic FEA.
2. Using Newton's second law, the acceleration of the armature is determined by dividing the force by its mass. The maximum acceleration,  $5465300 \text{ m/s}^2$ , occurs at 0.2 ms. Velocity of the armature is calculated by integrating the acceleration with respect to time. Displacement of the armature is calculated by integrating the velocity with respect to time.
3. A significant repulsive force between two rails is observed. The magnitude of the force is significant, the deflection and deformation of the rails is possible.



4. Regardless of the direction of the applied current, the resulting EMAG force accelerates the armature in one direction.

In the next chapter, the thermal analysis of the lab-scale EML is performed. The effect of friction heating and Joule heating will be separately studied. The armature displacement calculated in this chapter and the same applied electric current used in this chapter is going to be used as input in the investigation of friction heating and Joule heating, respectively.

## **CHAPTER 6: THERMAL ANALYSIS**

The EMAG force is maximized if the metal-to-metal contact at the interfaces is preserved while the armature slides along the rail. However, it is known that keeping the metal-to-metal contact throughout the operation is difficult because of the high armature velocity and the high electric current density.

In this chapter, the effects of frictional and Joule heating are examined in two separate thermal analyses. The effects of friction heating are investigated in the first section of this chapter, and the second section of the chapter discusses the effects of Joule heating.

### **6.1. Friction Heating**

As shown in previous chapter, the armature slides along the rails with the extreme velocity. This high sliding velocity generates a significant heat at the contact interface. The generated heat cannot conduct into the body because there is not a sufficient time. In typical setting, the armature exits the lab-scale EML within 1 to 1.5 ms once it is fired. In this analysis, the interface temperature rise due to the frictional heating is determined. Therefore, this analysis can predict when and where the melting

occurs. Three different values of the coefficient of friction and the heat partition<sup>4</sup> are used in this analysis to investigate how these parameters affect the rise in the interface temperature.

#### **6.1.1. Geometry, Meshing, Boundary Condition, and Element**

Figure 46 shows the geometry of the FEA model used in this analysis. This model is exactly same as the model used in the structural FEA of initial contact. The length of the rail and other layers is approximately 0.35 meters. Since melting of the material occurs at the early stage of sliding, modeling full 1.5 m long rail and other layers is not necessary.

In order to create the initial contact, the exact same boundary conditions applied at the structural FEA of initial contact is used in this analysis. Once the initial contact is established, all the X directional constraints of the armature are removed. Then, the armature is set to move at an assigned velocity which is determined in the previous chapter. The temperature of the FEA model is set to the room temperature initially.

---

<sup>4</sup> The weight factor for the distribution of heat conducted between two bodies which are in contact

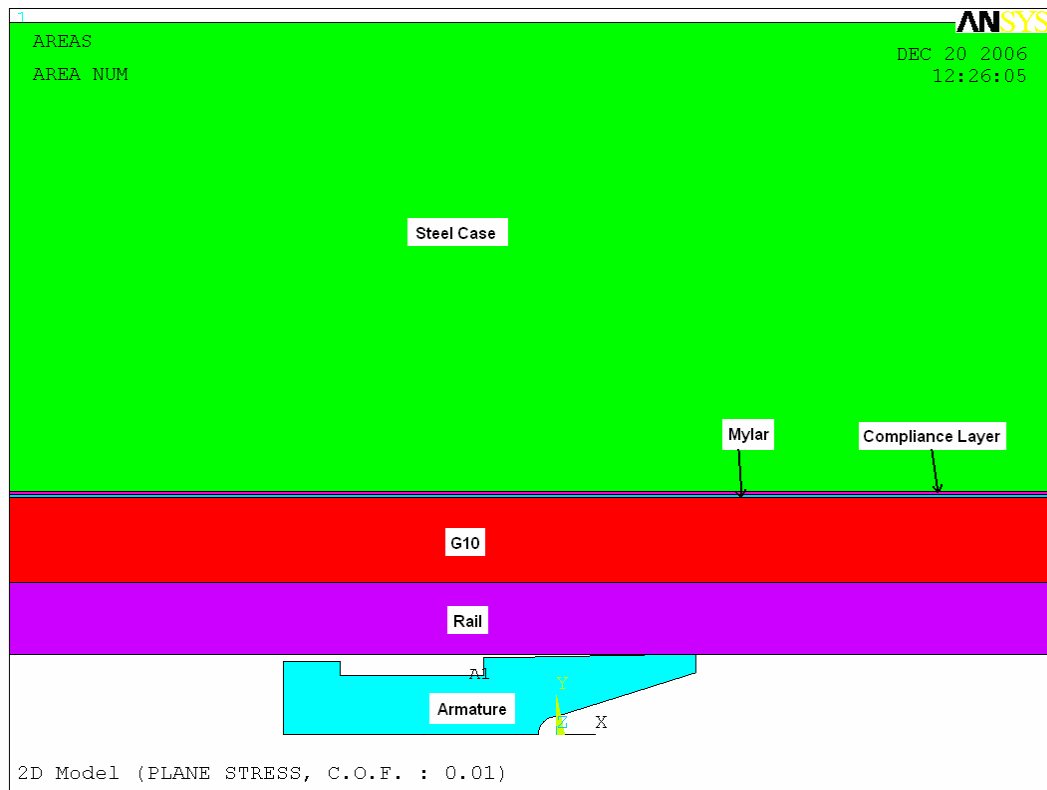
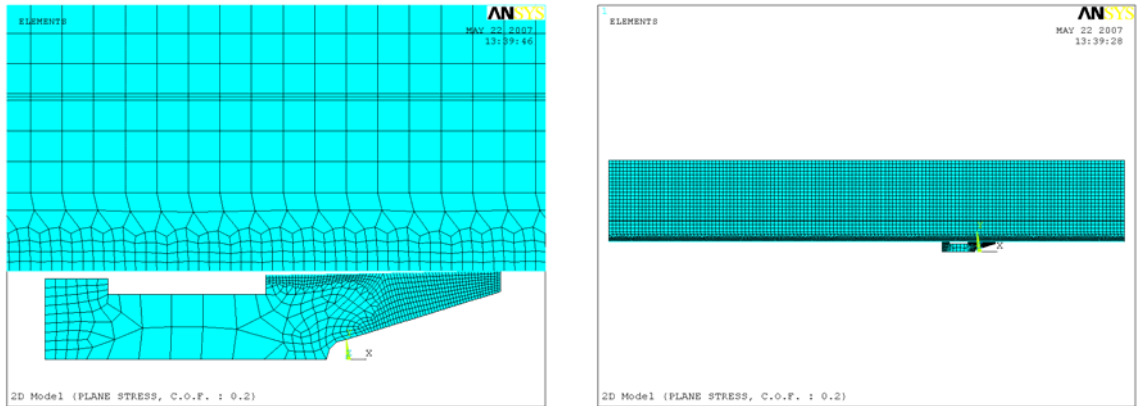


Figure 46: Close up geometry of the friction heating FEA model

Figure 47 shows the meshed FEA model. In order to accurately capture the effect of an extreme sliding velocity, a fine mesh density is applied near the contact interface. The contact elements are applied at the interface between the armature leg and the rail.



a) Close up view

b) Overall view

Figure 47: Mesh plot of the friction heating FEA model

Figure 48 shows the schematic diagram of Plane 13, an element that has a 2-D magnetic, thermal, electrical, piezo-electric, and structural field capability with limited coupling between the fields. The element is defined by four nodes with up to four degrees of freedom per node. The total number of elements used in the friction heating analysis is 6873.

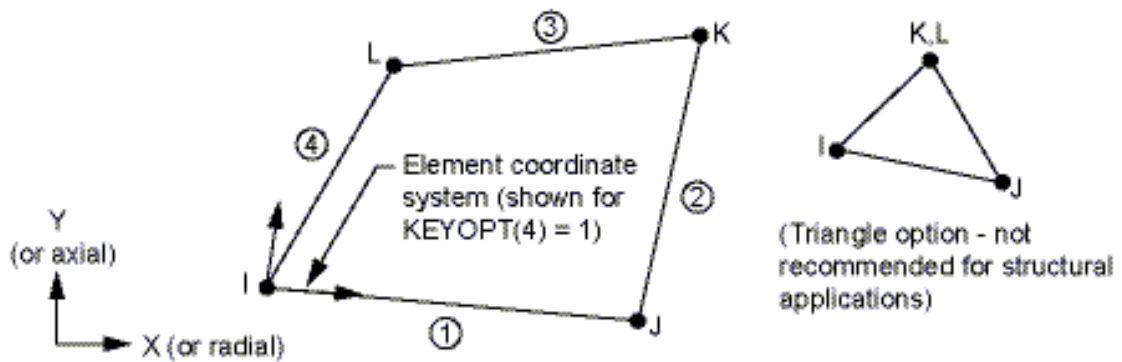


Figure 48: Schematic diagram of the Plane 13 element [22]

Three different values of the coefficient of friction (COF), 0.1, 0.2, and 0.3 are used in the analysis. Also, three different values of heat partition (HP), 10%-90%, 50%-50%, and 90%-10% are used in the analysis. The first value of the HP represents the percentage of the generated heat that goes into the rail, and the second value represents the percentage of the generated heat that goes into the armature. The three values of the COF selected here are expected in a typical setting. However, since the armature slides with an extreme velocity, the study by Jaeger [26] is used in estimating the values of HP. Jaeger's analytical solution uses the assumption that the average temperature of two surfaces is equal. The HP values calculated by using Jaeger's model show that about 97% of the generated heat goes into the rails and only about 3 % goes into the armature for the case of the average velocity of 1000 m/s. When the velocity of the armature is relatively low (below 100 m/s), about 55% of the generated heat goes into the rail and 45% goes into the armature. Therefore, the HP of 90%-10% seems to represent the best combined low and high speed effects.

### **6.1.2. Result and Discussion**

Figures 49 and 50 show results of the interface temperature at 57.5  $\mu$ s and 62.5  $\mu$ s, respectively. The corresponding maximum temperatures at these times are about

580°C and 740°C, respectively, while the melting temperature for the aluminum armature is approximately 600 °C. This occurs at the very early stage of the sliding. Since the velocity of the armature is low, the HP of 55%-45% is used in the analysis for these particular cases. The COF of 0.2 and the thermal contact conductance (TCC) of  $10^6$  J/s-K-m<sup>2</sup> is used in the FEA analysis. As expected, only the confined section of the armature leg near the contact interface is heated up. Unlike the armature, the rail does not experience any significant friction heating effects. For the rail, the temperature rise is insignificant. Although different parameters such as the COF and the HP result in different magnitudes of temperature rise at the contact interface, the trend shown in Figure 49 is observed in every case.

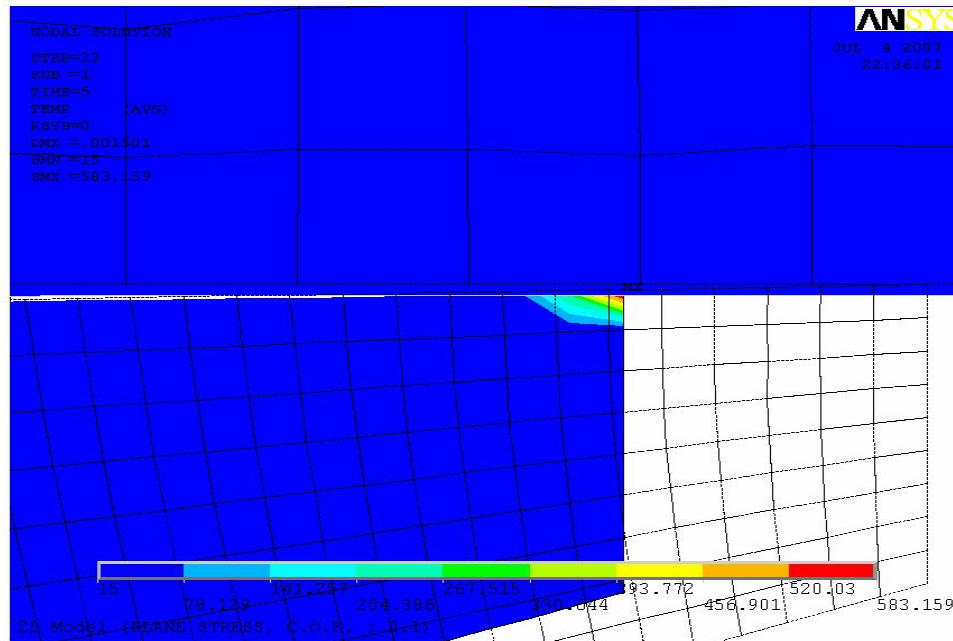


Figure 49: Temperature results at 57.5 microseconds due to friction heating for a coefficient of friction of 0.2, the thermal contact conductance of  $10^6$  J/s-K-m<sup>2</sup>, and 50%-50% heat partition between the armature leg and the rail

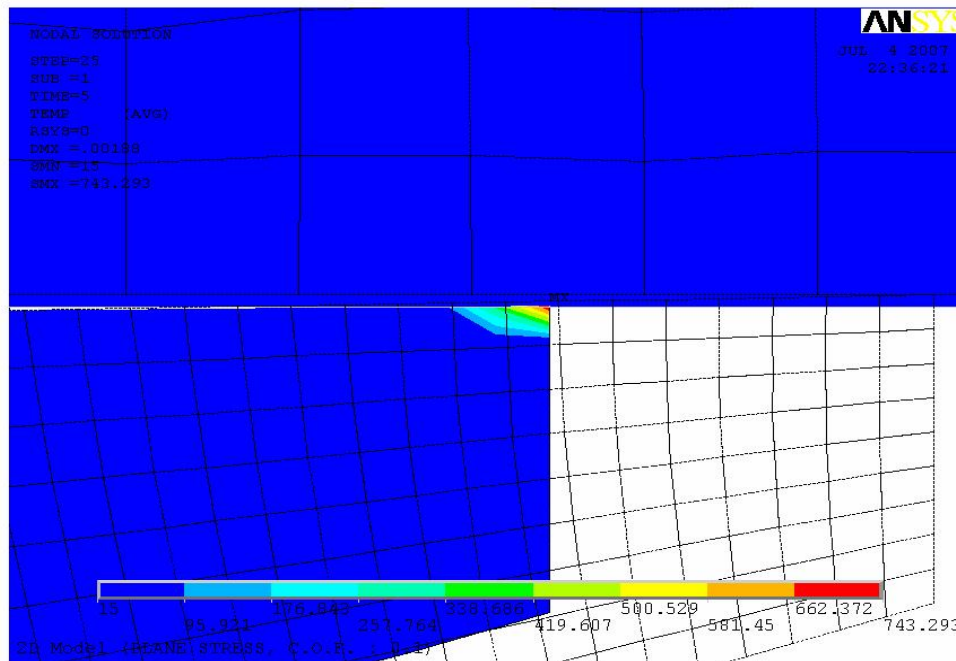


Figure 50: Temperature results at 62.5 microseconds due to friction heating for a coefficient of friction of 0.2, the thermal contact conductance of  $10^6$  J/s-K-m<sup>2</sup>, and 50%-50% heat partition between the armature leg and the rail



The results shown in Figures 49 and 50 need further investigation. Intuitively, it seems unlikely that the solid aluminum armature legs would start to melt at 62.5  $\mu$ s after the lab-scale EML is fired. In order to verify the FEA results, the energy balance between the generated heat and the stored heat is performed as given by Equation 6.1.

$$m(c_p \Delta T + h_{fusion}) = \zeta \cdot \mu \cdot N \cdot \bar{v} \cdot t \quad (6.1)$$

Here  $m$  is the mass,  $c_p$  is the specific heat,  $h_{fusion}$  is the heat of fusion,  $\Delta T$  is the temperature change,  $\zeta$  is the heat partition,  $\mu$  is the coefficient of friction,  $N$  is the normal force,  $\bar{v}$  is the instantaneous velocity, and  $t$  is the time. Left hand side of Equation 6.1 represents the stored heat, and the right hand side of Equation 6.1 represents the generated heat. If the problem involves melting of a material, a heat of fusion (the amount of energy which must be absorbed for 1 mole of a substance to change states from a solid to liquid or vice versa) must be included in the equation. In Figure 49, melting of the armature material has not occurred. Therefore, in this case, a heat of fusion term is not included in Equation 6.1. In Figure 50, melting of a material has occurred. Therefore, in this case, a heat of fusion term is included in Equation 6.1. Close examination of Figure 49 shows that approximately 180  $\mu$ m by 180  $\mu$ m is heated up to an average temperature of 250°C. Close examination of Figure 50 shows that approximately 180  $\mu$ m by 180  $\mu$ m is heated up to an average temperature of 350°C and

approximately  $15\text{ }\mu\text{m}$  by  $15\text{ }\mu\text{m}$  is melted. These heated areas are multiplied by the thickness of the armature,  $9.22\text{ mm}$ , to calculate the volume that stores the generated heat. This information and the material properties of the aluminum are substituted into Equation 6.1 to solve for melting time. It is determined that it takes approximately  $55\text{ }\mu\text{s}$  and  $67\text{ }\mu\text{s}$  for these cases shown in Figures 49 and 50, respectively. This result is comparable with the FEA results,  $57.5\text{ }\mu\text{s}$  and  $62.5\text{ }\mu\text{s}$ . This proves that, in  $62.5\text{ }\mu\text{s}$ , the small volume of the solid aluminum armature can melt due to friction heating as shown in Figure 50.

Figure 51 shows the results of the maximum interface temperature of friction heating for three different values of the COF where HP is 50%-50%. As shown in Figures 49 and 50, the maximum temperature occurs at the tip of the armature where it is in contact with the rail. The aluminum, a material of the armature, starts to melt around  $600\text{ }^{\circ}\text{C}$ . For the COFs of 0.1, 0.2, and 0.3, the tip of the armature leg starts to melt around  $0.075\text{ ms}$ ,  $0.055\text{ ms}$ , and  $0.045\text{ ms}$  after the lab-scale EML is fired, respectively.

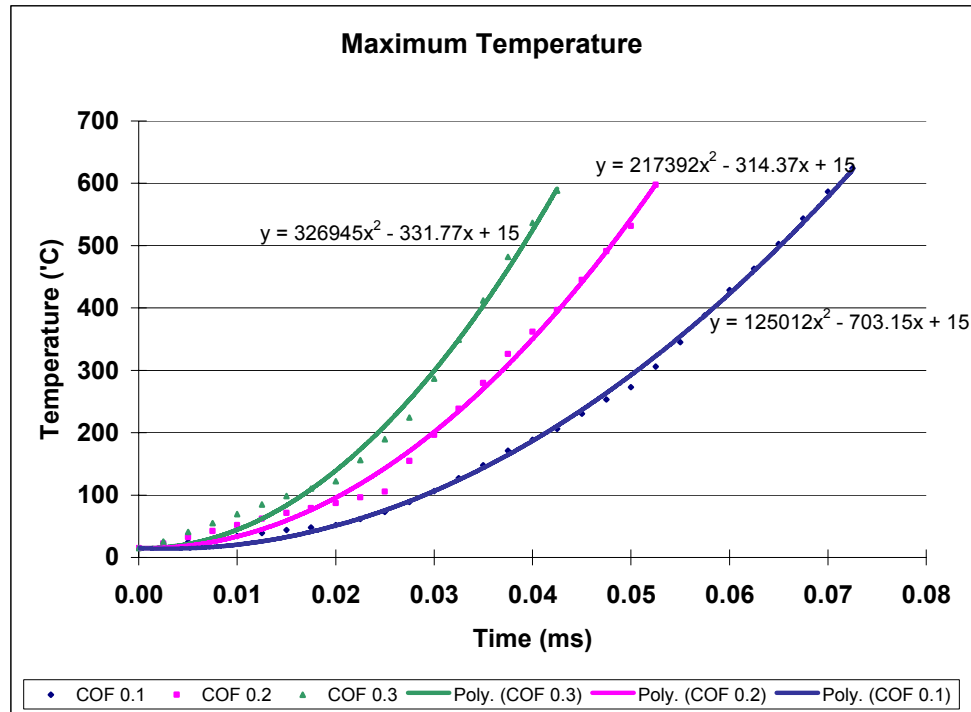


Figure 51: The maximum temperature results of friction heating for three different values of the coefficient of friction (HP 50%-50%)

Figure 52 shows the maximum temperature results of the friction heating for three different values of the HP. The COF is kept at the constant value of 0.2. As discussed earlier, the heat partition case that 90% of the heat goes into the rail and the other 10% goes into the armature appears to be most realistic. For this HP case, it takes about 0.11 ms for the armature leg to start melting for the lab-scale EML. Based on Figure 42, the armature has traveled about 2% of the total rail length when melting occurs.

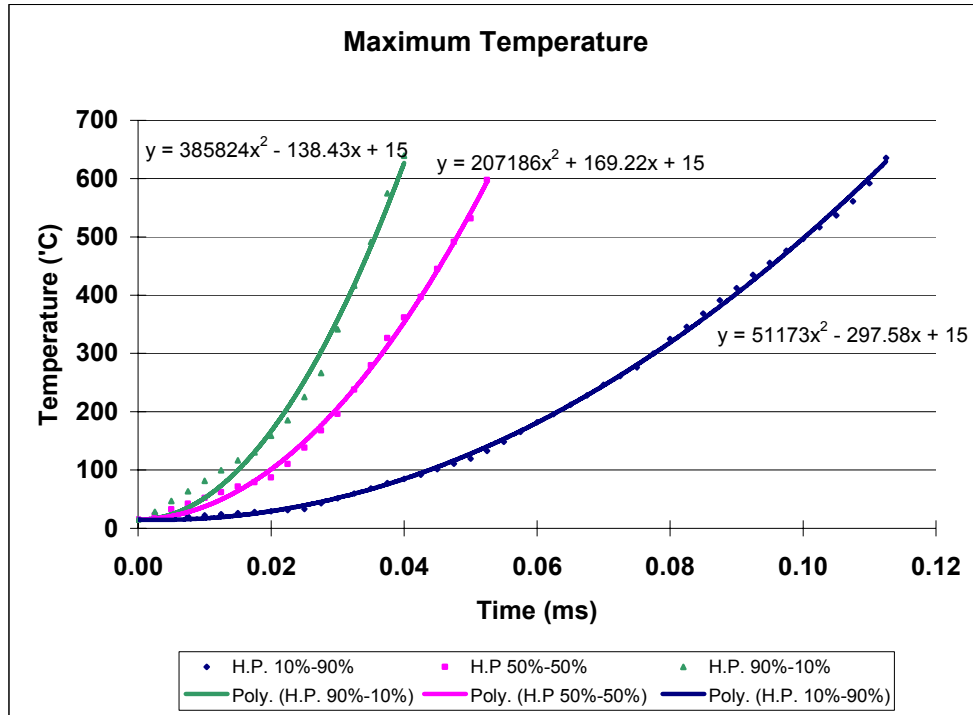


Figure 52: The maximum temperature results of friction heating for three different values of heat partition

Results of the friction heating show that immediate melting at the tip of the armature is inevitable for the current lab-scale EML. Although the melting of the tip of the armature can be delayed by varying the values of the COF and the HP, the delay is small; no meaningful advantage can be achieved.

It should be noted that, in this analysis, the resulting EMAG force is not included, since it is a decoupled analysis. However, if the resulting EMAG force is added to this analysis, the melting will be even expedited because the contact interface will experience a higher contact pressure.

In the next section, the effect of the Joule heating due to applied current is investigated.

## **6.2. Joule Heating**

The large magnitude of the applied electric current shown in Figure 34 flows through the small contact area in the lab-scale EML. This creates an extremely high current density near the contact interface and increases the contact interface temperature significantly. This analysis determines the time and location where the melting starts due to Joule heating.

### **6.2.1. Geometry, Meshing, Boundary Condition, and Element**

Two different FEA models are used in this analysis. The first model represents the worst case scenario, the minimum contact area configuration. This is the configuration before any melting occurs. The second model represents the best case scenario, the maximum contact area configuration. In this chapter, it is assumed that there is not plastic deformation. Therefore, while the tip of the armature melts, the stress that the armature experienced due to the initial contact continually pushes the armature legs into its original geometry until no stress is left in the armature. This

causes an increase in the contact area. This is the configuration where the armature experiences no stress.

Both FEA models are 2-D quasi-static models. Similar to the electromagnetic analysis, the armature stays still while different magnitudes of electric current are applied.

Figures 53 and 54 show the meshed geometry of the worst and the best case scenarios, respectively. Since the high temperature is expected near the interface, a very fine mesh density is applied around the contact interface

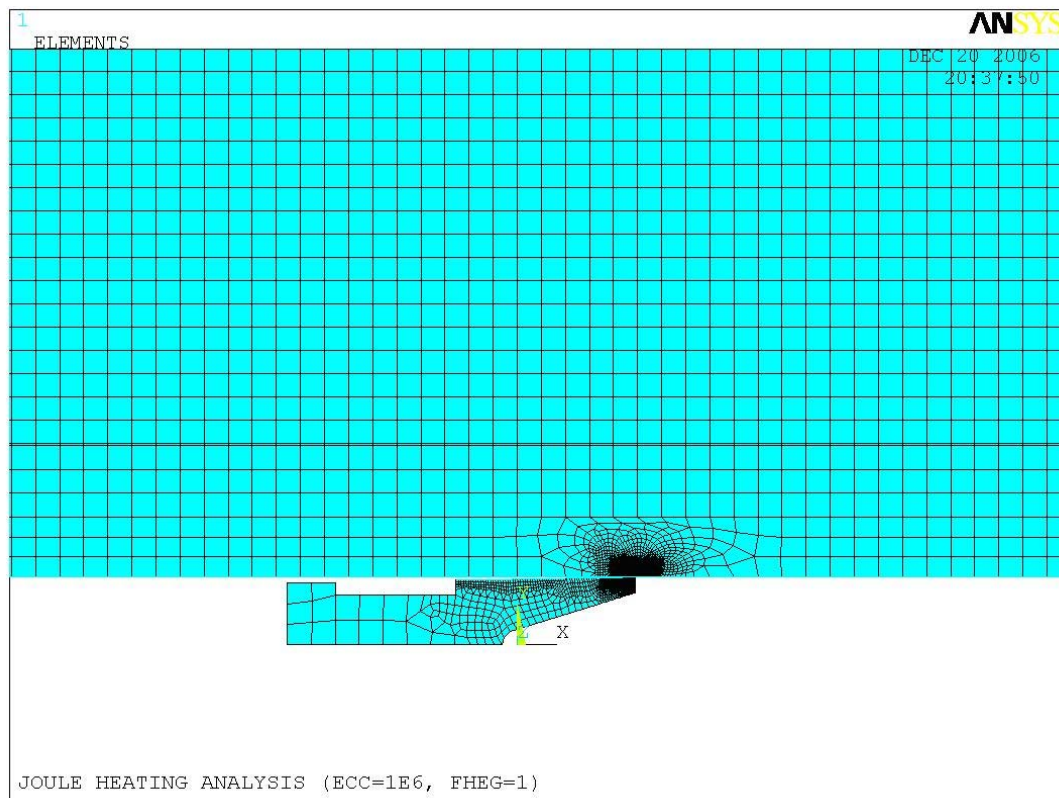


Figure 53: Mesh plot of the worst case scenario of the Joule heating FEA model

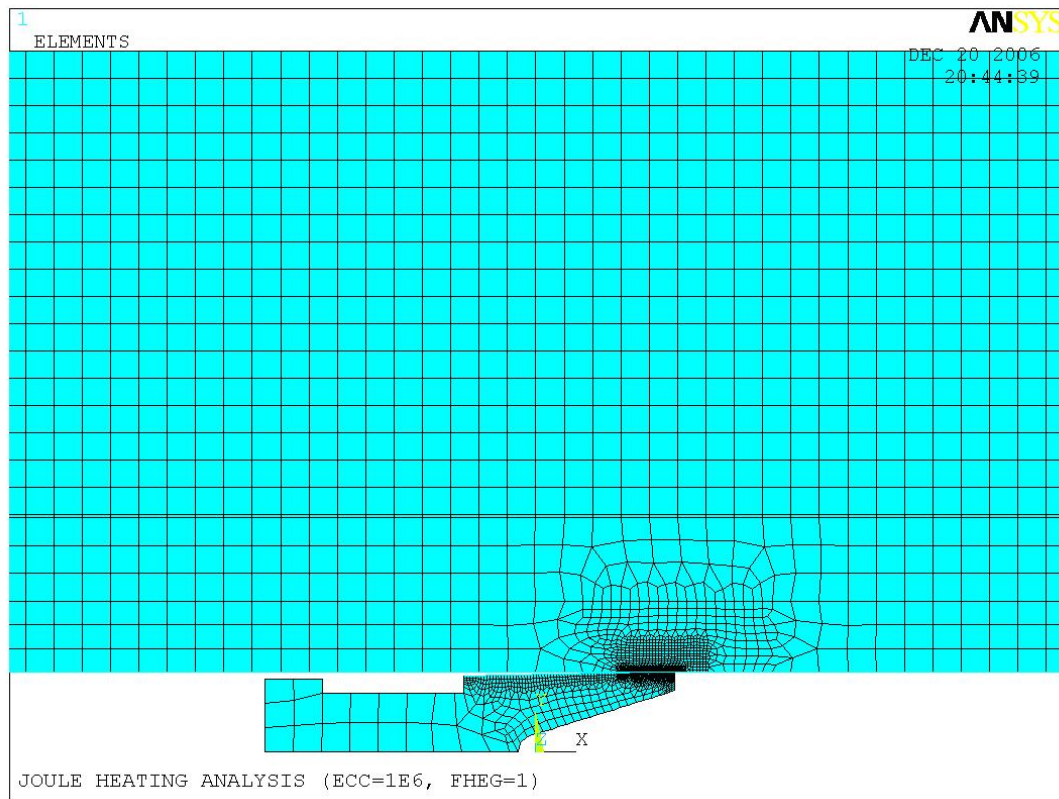


Figure 54: Mesh plot of the best case scenario of the Joule heating FEA model

Contact element pairs are applied at the contact interface for both cases. Initially, the room temperature, 15 °C, is applied to the both FEA models. At the bottom surface of the armature, zero volts is applied as the boundary condition. At the nodes located at the right end of the rail, various electric current are applied. The total number of elements used in the worst and the best case scenario are 15500 and 12724, respectively.

Figure 55 shows a schematic diagram of Plane 67, an element that has thermal

and electrical conduction capability. Joule heating generated by the current flow is also included in the heat balance. The element has four nodes with two degrees of freedom, temperature and voltage, at each node.

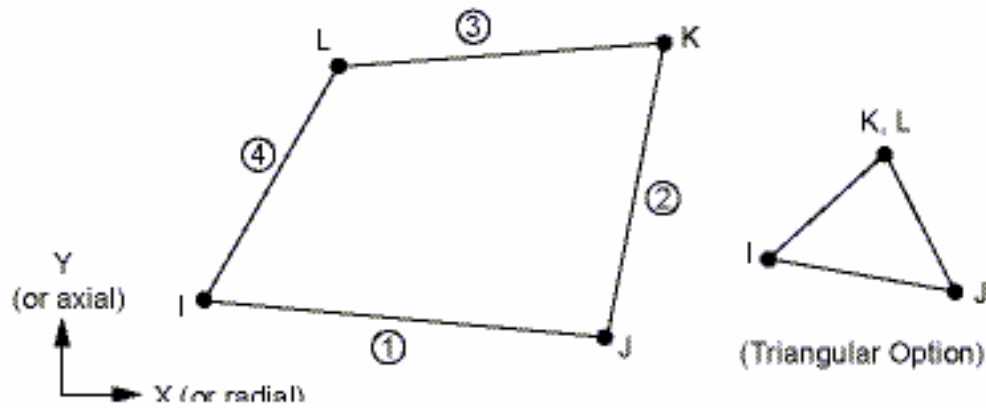


Figure 55: Schematic diagram of the Plane 67 element [22]

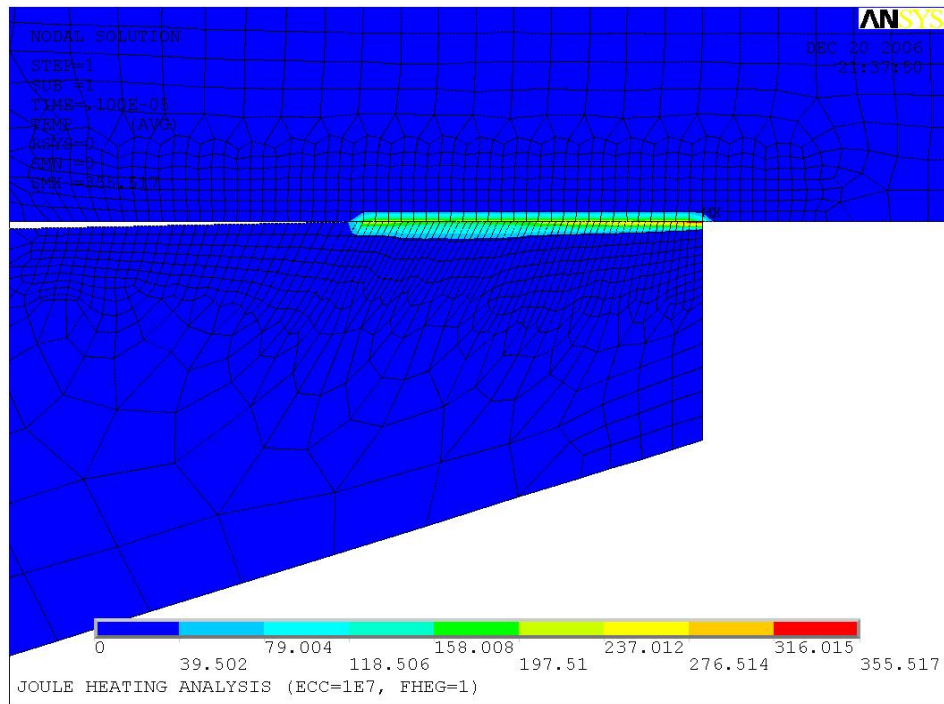
### 6.2.2. Result and Discussion

As expected, a small contact area with the large magnitude of the applied electric current creates a significant heat generation at the contact interface. At 0.4 microseconds, an electric current of  $\sim 25$  k-ampere is supplied to the lab-scale EML. This is an order of magnitude smaller compared to actual maximum current of 450 k-ampere as shown in Figure 34.

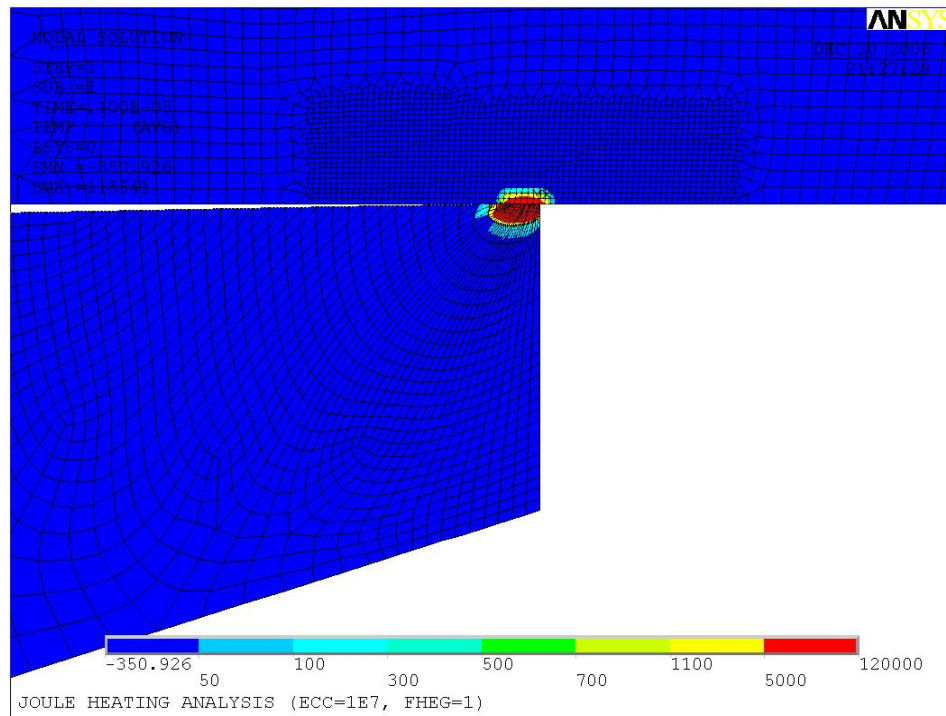
Figure 56 shows the temperature results of an applied electric current of  $\sim 25$  k-amperes. The electric contact conductance (ECC),  $10^7$  Siemens per meter ( $\text{S}\cdot\text{m}^{-1}$ ), is



used in the analysis. For the best case scenario, the temperature at the contact interface is not reached the melting temperature yet. It is due to the larger contact area. For the worst case scenario, the contact interface temperature rose beyond the melting temperature of the both aluminum and copper. This result suggests that instantly the aluminum armature and the copper rail melt due to Joule heating. As shown in Figure 56, although the temperature of the contact interface is reached the melting point, the heat could not be conducted away from the interface. The melting of the contact interface for the best case scenario occurs at  $\sim 0.6 \mu\text{s}$ .



a) Best case scenario



b) Worst case scenario

Figure 56: Results of the temperature plot for an electric contact conductance of  $10^7$  Siemens per meter ( $\text{S}\cdot\text{m}^{-1}$ )

This quasi-static FEA results of Joule heating suggest that immediate melting of the material at the contact interface will occur in this particular lab-scale EML. Even at 0.4  $\mu\text{s}$ , the melting of both the aluminum armature and the copper rail is possible due to Joule heating. Melting of the copper rail may not have taken place had a transient analysis been performed. It should be noted that, in this analysis, the resulting EMAG force is not included, since it is a decoupled analysis. However, if the resulting EMAG force is added, it is expected to cause increase in the contact area. This can reduce the heat generation due to Joule heating significantly.

The results of frictional and Joule heating show that immediate melting of the material at the contact interface is inevitable. Initially, Joule heating dominates frictional heating in the current lab-scale EML. Some studies suggest that there must be melting at the contact interface for the armature to promote sliding. Therefore, initial melting at the contact interface may not be an adverse effect. However, once the armature slides, the continuing melting of the material at the contact interface must be controlled. In order to control the melting of the material at the contact interface, 1) the present armature design should be modified, 2) different armature/rail materials that have higher melting temperature should be selected, and/or 3) the EML structure should be modified to enable thermal management (for example, cooling passages) [13].

## **CHAPTER 7: CONCLUSIONS AND RECOMMENDATIONS**

In this chapter, the conclusions of the work performed in this thesis and the recommendations that identify potential future work are presented.

### **7.1. Conclusions**

The purpose of this work is to improve the understanding of the armature-to-rail contact so that the best performance of the lab-scale EML can be achieved. This has been facilitated by developing a computer design tool. The computer design tool, FEA of physical phenomena of the lab-scale EML, consists of four (structural, modal, electromagnetic, and thermal) components. Conclusions drawn from use of these computer codes follow.

#### **7.1.1. Structural Analysis**

The structural analysis is developed to determine contact area, contact pressure, von Mises stress, and deformation of an EML due to initial armature-to-rail contact. In order to assure accuracy, a compliance layer, an artificial layer that takes account any stiffness present in the EML, is incorporated in the FEA model. The program accepts

interference as a load (input) and provides the aforementioned quantities as output.

The structural analysis indicates that the maximum contact pressure and von Mises stress of the current lab-scale EML is close to but lower than the yield strength of the softer material (aluminum armature) at initial contact. This result suggests that the effect of plasticity does not need to be considered. In addition, it determined the contact area of the current lab-scale EML to be  $3.32 \text{ mm}^2$ .

#### **7.1.2. Modal Analysis**

The purpose of modal analysis is to study the vibration characteristics (i.e., vibration frequencies/periods and vibration mode shapes) of the armature. This program can handle both the un-deformed and deformed armatures. For modal analysis of the deformed armature, the force is applied to the armature through a separate structural analysis to create a deformed geometry. This program does not require any input to provide the vibration characteristics.

Modal analysis determined that vibration of the armature legs is expected during sliding since the vibration period of both un-deformed and deformed armatures of the present lab-scale EML is much shorter than the duration of the sliding. It also indicated that the vibration frequency is proportional to  $\sqrt{E/\rho}$  and inversely proportional to the

size of the armature.

### **7.1.3. Electromagnetic Analysis**

The electromagnetic analysis determines the electromagnetic force created in the EML due to applied current. It is important that the air (i.e., surrounding space) be included in the FEA model, since the electric and the magnetic fields reside in the air. It takes an electric current as a load (input) and provides electromagnetic force as output.

The electromagnetic analysis shows that there is a repelling force between two rails in the lab-scale EML. It also shows that a significant X direction force is present on the rails near the contact interface. These results should not be overlooked since rails can be deflected and/or deformed. The acceleration, velocity, and the displacement of the armature can be calculated as a function of time. For the lab-scale EML with a given current density, the maximum velocity of the armature is determined to be approximately 2400 m/s. This value matches closely with experimental measurement. In addition, the fact that an EML accelerates an armature in one direction regardless of the direction of the applied current is shown with this program.

### **7.1.4. Thermal Analysis**

The purpose of the thermal analysis is to determine the temperature at the contact interface. Friction heating and Joule heating are separately considered in two programs. For a FEA of friction heating, the displacement of the armature is used as a load (input) and the temperature at the contact interface is provided as output. For a FEA of Joule heating, the applied current is entered as a load (input) and the temperature at the contact interface is provided as output.

For the lab-scale EML, the thermal FEA determined that friction heating will cause melting of the armature legs about 0.15 ms (i.e., 2% away from initial position) after being fired. For this analysis, the coefficient of friction was set at 0.2 and the heat partition was set at 90 % into rails and 10 % into armature. Thermal FEA of Joule heating determined that at 0.4 microseconds, melting of the armature legs is expected.

#### **7.1.5. Discussion**

This computer program has many powerful capabilities that can assist the advance of the lab-scale EML research. It can analyze, optimize, and aids the experimental work.

First, the technique employed in this computer program can be used in analyzing the four decoupled physical phenomena of any electromagnetic launcher. By updating

the geometry, the loading and boundary conditions, and the material properties, the structural, the vibrational, the electromagnetic, and the thermal characteristics of any electromagnetic launcher can be determined.

Second, this computer program can be used in optimizing the design of the EML and the material selection. For example, many problems such as the plastic deformation, the immediate melting, and the vibration of the armature legs of the lab-scale EML have been discovered in this work. These problems can be improved or even eliminated by optimizing armature geometry. Figure 57 shows the possible optimization criteria of the armature geometry. By varying the parameters shown in Figure 57, an optimum design that provides a maximum contact area, a sufficient contact pressure, and optimum vibration characteristics can be determined. Likewise, changing the materials for the armature and the rail, the aforementioned problems can be improved.



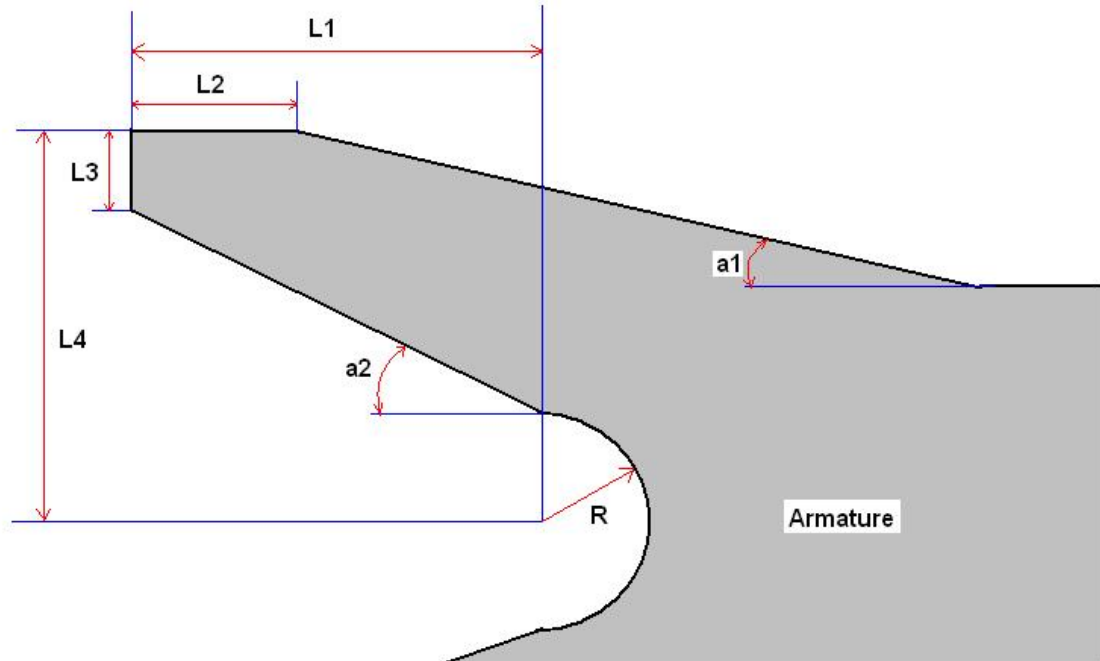


Figure 57: Optimization of the armature geometry

Lastly, this computer program can aid the experimental work. It can provide information so that the instrument and/or equipment with the adequate capacity can be used in the experimental work. For example, the maximum acceleration of the lab-scale EML calculated using the FEA results is approximately  $5.5 \cdot 10^6 \text{ m/s}^2$ . Therefore, if a sensor needs to be installed in the armature, the sensor that can withstand this acceleration must be used. Therefore, this computer program prevents the wasting of unnecessary and expensive equipments and time spent in experimental work.

## **7.2. Recommendations**

Although the decoupled analyses presented in this work provide meaningful results and improve our understanding at the armature-to-rail interface of the lab-scale EML, obtaining coupled FEA results are necessary to have comprehensive understanding at the contact interface. Obtaining the coupled solution with one simulation is optimal; but if proven to be too difficult, a means to sequentially couple the individual components should be considered.

Two important parameters (coefficient of friction and heat partition) greatly influence the thermal condition at the contact interface. A means to measure these two parameters should be developed. Without accurate input of these parameters, any FEA and/or analytical solution will be only a best estimate.

The impact of the EMAG force and the eddy current effects on the steel containment and other layers (G10 and Mylar) must be studied. Deformation of the steel containment was evident after many shots were fired. If the reusability of the EML is an important consideration, the investigation of the impact of the EMAG force and the eddy current effect on the steel containment and other layers should be further investigated.

In this study, molten material had not been removed from the model. This,

however, needs to be addressed in future studies while using the “birth and death” capability built within the ANSYS program.

## APPENDIX A

### MATERIAL PROPERTIES

#### A.1 ALUMINUM ARMATURE

YOUNG'S MODULUS	680 MPa
POISSON'S RATIO	0.33
COEFFICIENT OF FRICTION	0.2
DENSITY	2700 kg/m <sup>3</sup>
SPECIFIC HEAT	896 J/kg-K
THERMAL CONDUCTIVITY	180 W/m-K
RESISTIVITY	0.04 $\mu\Omega$ -m
MELTING TEMPERATURE	~ 600°C

#### A.2 COPPER RAILS

YOUNG'S MODULUS	125 GPa
POISSON'S RATIO	0.33
COEFFICIENT OF FRICTION	0.2
DENSITY	8900 kg/m <sup>3</sup>
SPECIFIC HEAT	385 J/kg-K
THERMAL CONDUCTIVITY	365 W/m-K
RESISTIVITY	0.05 $\mu\Omega$ -m
MELTING TEMPERATURE	~ 1000°C

#### A.3 G10 INSULATOR

YOUNG'S MODULUS	17 GPa
POISSON'S RATIO	0.1
COEFFICIENT OF FRICTION	0.2
DENSITY	1500 kg/m <sup>3</sup>
SPECIFIC HEAT	N/A
THERMAL CONDUCTIVITY	N/A
RESISTIVITY	0.1 $\Omega$ -m

#### A.4 MYLAR

YOUNG'S MODULUS	4 GPa
POISSON'S RATIO	0.1
COEFFICIENT OF FRICTION	0.2
DENSITY	1500 kg/m <sup>3</sup>
SPECIFIC HEAT	N/A
THERMAL CONDUCTIVITY	N/A
RESISTIVITY	0.1 $\Omega$ -m

#### A.5 COMPLIANCE LAYER

YOUNG'S MODULUS	20 MPa
POISSON'S RATIO	0.3
COEFFICIENT OF FRICTION	N/A
DENSITY	N/A
SPECIFIC HEAT	N/A
THERMAL CONDUCTIVITY	N/A
RESISTIVITY	N/A

#### A.6 STEEL CONTAINMENT

YOUNG'S MODULUS	185 GPa
POISSON'S RATIO	0.25
COEFFICIENT OF FRICTION	0.2
DENSITY	8030 kg/m <sup>3</sup>
SPECIFIC HEAT	500 J/kg-K
THERMAL CONDUCTIVITY	16.2 W/m-K
RESISTIVITY	0.72 $\mu\Omega$ -m

## REFERENCES

1. Petry, C., *Schematic diagram of an electromagnetic launcher*, NAVSEA Dahlgren.
2. Merrill, R. and F. Stefani, *Electrodynamics of the Current Melt-Wave Erosion Boundary in a Conducting Half-Space*. IEEE TRANSACTIONS ON MAGNETICS, 2003. **39**(1): p. 66-71.
3. Angeli, M. and E. Cardelli, *Electro-Thermal Behavior of Solid Armatures*. IEEE TRANSACTIONS ON MAGNETICS, 1999. **35**(1): p. 47-52.
4. Drobyshevski, E.M., E.N. Kolesnikova, and V.S. Yuferev, *Thermoelectrodynamic loss of material by a solid armature in a railgun as a cause of velocity limitation*. TECHNICAL PHYSICS LETTERS, 1999. **25**(4): p. 260-262.
5. Powell, J.D. and A.E. Zielinski, *Current and Heat Transport in the Solid-Armature Railgun*. IEEE TRANSACTIONS ON MAGNETICS, 1995. **31**(1): p. 645-650.
6. Powell, J.D. and A.E. Zielinski, *Observation and Simulation of Solid-Armature Railgun Performance*. IEEE TRANSACTIONS ON MAGNETICS, 1999. **35**(1): p. 84-89.
7. Kim, B.K., K.T. Hsieh, and F.X. Bostick, *A Three-Dimensional Finite Element Model for Thermal Effect of Imperfect Electric Contact*. IEEE TRANSACTIONS ON MAGNETICS, 1999. **35**(1): p. 170-174.
8. Drobyshevski, E.M., et al., *Role of the pinch effect in a high-velocity metallic contact with a high current*. TECHNICAL PHYSICS LETTERS, 1999. **25**(3): p. 245-247.
9. Drobyshevski, E.M., et al., *Physics of Solid Armature Launch Transition into Arc Mode*. IEEE TRANSACTIONS ON MAGNETICS, 2001. **37**(1): p. 62-66.

10. James, T.E. and D.C. James, *Contact Pressure Distribution and Transition in Solid Armatures*. IEEE TRANSACTIONS ON MAGNETICS, 2001. **37**(1): p. 81-85.
11. Tzeng, J.T., *Dynamic Response of Electromagnetic Railgun Due to projectile Movement*. IEEE TRANSACTIONS ON MAGNETICS, 2003. **39**(1): p. 472-475.
12. Kothmann, R.E. and F. Stefani, *A Thermal Hydraulic Model of Melt-Lubrication in Railgun Armatures*. IEEE TRANSACTIONS ON MAGNETICS, 2001. **37**(1): p. 86-91.
13. Satapathy, S. and C. Persad, *Thermal Stresses in an Actively Cooled Two-Piece Rail Structure*. IEEE TRANSACTIONS ON MAGNETICS, 2003. **39**(1): p. 468-471.
14. Hopkins, D.A., et al., *Analysis of Startup Behavior in a "C-Shaped" Armature Using Linked EMAP3D/DYNA3D Finite Element Codes*. IEEE TRANSACTIONS ON MAGNETICS, 1999. **35**(1): p. 59-64.
15. Newill, J.F., J.D. Powell, and A.E. Zielinski, *Coupled Finite-Element Codes for Armature Design*. IEEE TRANSACTIONS ON MAGNETICS, 2003. **39**(1): p. 148-152.
16. Barber, J.P. and A. Challita, *Velocity Effects On Metal Armature Contact Transition*. IEEE TRANSACTIONS ON MAGNETICS, 1993. **29**(1): p. 733-738.
17. Barber, J.P., et al., *Contact transition in metal armatures*. IEEE TRANSACTIONS ON MAGNETICS, 1991. **27**(1): p. 228-232.
18. Barber, J.P. and Y.A. Dreizin, *Model of contact transitioning with "realistic" armature-rail interface*. IEEE TRANSACTIONS ON MAGNETICS, 1995. **31**(1): p. 96-100.
19. James, T.E., *Current Wave and Magnetic Saw-Effect Phenomena in Solid Armatures*. IEEE TRANSACTIONS ON MAGNETICS, 1995. **31**(1): p. 622-627.

20. Woods, L.C., *The Current Melt-Wave Model*. IEEE TRANSACTIONS ON MAGNETICS, 1997. **33**(1): p. 152-156.
21. Stefani, F., et al., *Electrodynamic Transition in Solid Armature Railguns*. IEEE TRANSACTIONS ON MAGNETICS, 2001. **37**(1): p. 101-105.
22. ANSYS, Inc., *ANSYS Release 9.0 Documentation*. 2004.
23. Bair, S., *Personal Communication*, in *Georgia Institute of Technology*. 2007: Atlanta, GA.
24. Johnson, A.J. and F.C. Moon, *Elastic Waves in Electromagnetic Launchers*. IEEE TRANSACTIONS ON MAGNETICS, 2007. **43**(1): p. 141-144.
25. Watt, T. and S. Fish, *Examination of High Frequency Contact Chatter in Trailing Arm Armatures*. IEEE TRANSACTIONS ON MAGNETICS, 2001. **37**(1): p. 106-110.
26. Jaeger, J.C., *Moving sources of heat and the temperature at sliding contacts*. J of the Royal Society of New South Wales, 1942. **76**: p. 203-224.